Technische Universität München
TUM School of Natural Sciences

Thermodynamic Properties of Oxide Compounds under Transverse Magnetic Fields

Alexander Engelhardt, M. Sc.

Vollständiger Abdruck der von der TUM School of Natural Sciences der Technischen Universität München zur Erlangung des akademischen Grades eines

Doktors der Naturwissenschaften (Dr. rer. nat.)

genehmigten Dissertation.

Vorsitz:		Prof. Dr. Johannes Knolle
Prüfende der Dissertation:	1.	Prof. Dr. Christian Pfleiderer
	2.	Prof. Dr. Christian Back

Die Dissertation wurde am 17.10.2024 an der Technischen Universität München eingereicht und durch die TUM School of Natural Sciences am 19.12.2024 angenommen.

Contents

1 Introduction

1.1 Quantum Magnetism and Effective Models

The investigation of magnetic materials has been attracting great interest for a long time covering a broad range of topics from fundamental physics, such as symmetry breaking, magnetic order and topology [1–3], to technical applications. Typical applications include highly permeable magnets for sustainable applications such as electric motors [4–6], but also spintronic applications for relays and switches [7].

A significant part of research in the field of magnetism covers the study of quantum magnetism and quantum phase transitions. In this area, the discovery of novel ground states and novel excitations is of central interest. Notable examples include the discovery of magnetic monopoles in spin-ice materials [8, 9], skyrmions in chiral magnets [10] and the search for Majorana-fermions in spin-liquids [11, 12].

This work is dedicated to the experimental investigation of quantum magnetism and quantum criticality in strongly anisotropic magnetic compounds. A central question concerns the extent to which quantum criticality results in the breakdown of the concept of low-lying excitations and the emergence of a quantum critical continuum. In this context, experimental investigations of complex magnetic compounds exhibiting quantum magnetism serve as a testing ground for new theoretical concepts and methods.

A common approach to describing complex systems is the use of effective theories to model experimental observations. In such a model, complex mechanisms are simplified so that observations in experiments can be correctly described without full account of the microscopic details. The textbook example of this concept is the effective mass of an electron in a solid rather than explicitly considering the detailed interactions between the electron and the periodic Coulomb potential of the crystal lattice [13]. Other applications of this concept include the Thomas-Fermi screening of the potential of an electron representing the effective pairwise interaction in a system of many electrons [13] or the mean field approach of the exchange interactions of an atom with its surroundings in a solid [14].

A key aspect of effective models is the dimensionality of the system. Depending on the chosen dimensions, the physical properties may change dramatically. For the free electron gas, the dimensionality of a system is responsible for the variation of the density of states [13]. For the effective model of magnetic systems, an additional aspect is the anisotropy of the magnetic moments. The associated degree of freedom of the magnetic

spins may be classified as three-dimensional Heisenberg-spins, two-dimensional XY-spins, or one-dimensional Ising-spins [14].

1.2 Quantum Magnets in Transverse Magnetic Fields

In this thesis, two oxide compounds were investigated, which are considered to contain magnetic spins with an Ising anisotropy. $TbFeO_3$ was reported to be the host of two magnetic sublattices interacting with each other resulting in the formation of a magnetic soliton lattice in a transverse magnetic field. $CoNb_2O_6$ is a prototype material for the investigation of the quantum critical point of a one-dimensional system in a transverse magnetic field[15]. In $CoNb_2O_6$, the magnetic cobalt atoms are ferromagnetically coupled on quasi one-dimensional zig-zag chains along the c-axis [16]. Every chain of cobalt atoms is surrounded by chains of non-magnetic niobium atoms. The combination of the crystal electric field of the oxygen atoms surrounding the cobalt atoms in an octahedron and spin-orbit coupling induce the Ising anisotropy of the cobalt spins [17].

The central work on the Ising-chain compound $CoNb_2O_6$ utilizes various effective models to explain the excitation spectra observed in inelastic neutron scattering experiments and THz-spectroscopy [1, 16, 18–20]. Initially, a simple one-dimensional Ising model was used in combination with a mean field approach to account for the weak interchain interactions [16]. Following models have become more elaborate including glide-symmetry breaking and Kitaev-like physics and more complex terms in the Hamiltonian to account for different signatures observed in spectroscopic measurements [1, 18–26].

The Ising model in a transverse magnetic field is an archetypal example of a quantum phase transition [27]. Unlike a classical phase transition, a quantum phase transition is driven by quantum fluctuations instead of thermal fluctuations and takes place at $T = 0\,\mathrm{K}$ [28]. A special case of a quantum phase transition is the one-dimensional Ising chain in a transverse magnetic field. The transverse magnetic field induces a quantum phase transition from an ordered magnetic phase to a quantum paramagnetic phase. $CoNb_2O_6$ is considered to be one of the best realizations of an one-dimensional ferromagnetic Ising chain [16]. It was shown theoretically and experimentally that the weak interchain couplings between different chains of cobalt atoms lead to bound states in the excitation spectrum in the ordered magnetic phase and to the emergence of an E8 symmetry validated by the observed excitation spectrum in the vicinity of the quantum critical point [16, 29].

Transverse field tuning of an Ising system can not only result in quantum criticality but also in the emergence of novel magnetic effects, as seen in the perovskite $TbFeO_3$ [15]. This

compound consists of two magnetic sublattices of iron spins and terbium spins interacting with each other. The terbium sublattice exhibits a hard-axis Ising anisotropy while the iron sublattice exhibits a less pronounced anisotropy. In the absence of a magnetic field, the magnetic interactions within the sublattices and the interplay between them lead to several phase transitions [30]. A magnetic field transverse to the terbium spins induces the emergence of a so-called soliton lattice. This magnetic texture is characterized by a periodic alignment of antiferromagnetic domains with a periodicity of approximately 340 Å[15].

In some effective models, quasi-particle excitations play a key role [13]. For example, in BCS-theory for conventional superconductivity, the attractive interaction is modeled using a virtual exchange phonon that mediates the attractive force between two electrons. The explanation of the fractional quantum hall effect requires the introduction of so-called composite fermions. These are quasi-particles are essential for the theoretical description and consist of an electron or hole and a magnetic flux quantum. In the effective model proposed for the soliton lattice in $TbFeO_3$, a virtual magnon within the iron-sublattice is being accounted for to mediate a repulsive interaction between the solitonic domain-walls, thereby stabilizing the magnetic texture [15]. In analogy to the Yukawa-force in particle physics, the magnons can be integrated out, resulting in a Coulomb-like interaction between the domain-walls.

1.3 Methods for the Investigation of Transverse-Field Magnetism

Our investigations of $TbFeO_3$ and $CoNb_2O_6$ in a transverse magnetic field employ transverse susceptibility measurements and heat capacity measurements as well as measurements of the magnetocaloric effect and elastic neutron scattering. The measurement of the transverse susceptibility has proven to be a powerful tool for the measurement of Ising systems in a transverse magnetic field, such as the three-dimensional Ising ferromagnet $LiHoF_4$ [31]. Transverse susceptibility enables to probe the magnetic response of a system parallel to the easy axis of a magnetic compound while a static magnetic field is applied transverse to the easy axis and the probing direction of the susceptibility. For investigations of strongly anisotropic materials in transverse magnetic fields, this method can provide a more effective extraction of information out of the measurements in comparison to conventional longitudinal susceptibility measurements, as demonstrated in this thesis.

The measurement of the heat capacity provides valuable information on the thermodynamic properties of a system. Low-temperature heat capacity measurements can extract information on the nature of phase transitions and the entropy contained in a system.

However, conventional heat capacity setups are typically too delicate to withstand a magnetic torque acting on an anisotropic sample in a transverse magnetic field. Therefore, we have used custom-made setups developed within our group for the specific purpose of measuring anisotropic magnetic samples down to milli-Kelvin temperatures [32, 33]. Additionally, the hard-axis heat capacity setup was also employed to measure the magnetocaloric effect, which provides supplementary information on phase transitions and the change of entropy in a magnetic field.

1.4 Outline of this Thesis

Our results obtained from the measurements of thermodynamic properties of $TbFeO_3$ and $CoNb_2O_6$ have updated the hard-axis magnetic phase diagrams and serve as input to validate or disprove effective models proposed in literature, which were mostly based on neutron diffraction experiments and spectroscopic measurements.

The following work begins with a description of the experimental details including the crystal synthesis, the cryogenic environment, the ac susceptibility and heat capacity measurement setups, the software used for the measurement of the heat capacity, and the sample alignment procedure for the measurements of $CoNb_2O_6$ in transverse magnetic fields.

The second part of the thesis introduces the state of research on $TbFeO_3$ and presents the experimental results of the measurement of the ac susceptibility, the heat capacity, and neutron diffraction experiments. The central result of this section is the presentation of a transverse-field phase diagram for magnetic fields up to 12 Tesla.

The third part of this thesis begins with the description of a quantum phase transition and the current state of research on the Ising system $CoNb_2O_6$. This is followed by a description of the single-crystal synthesis and the characterization of the sample in zero magnetic field and for magnetic fields applied along the major crystallographic directions. The experimental results of the transverse field magnetism in $CoNb_2O_6$ are presented, starting with the measurements of the ac susceptibility and the heat capacity under perfect transverse orientation and under slightly misaligned transverse field orientation. A detailed magnetic phase diagram for perfect transverse field orientation is inferred and the effect of tilting the magnetic field away from this orientation are discussed. Finally, the scaling of the critical fields and critical temperatures is evaluated.

2 Experimental Methods

For the scientific studies reported in this thesis large high-quality single crystals were grown of the multiferroic perovskite $TbFeO_3$ and the quasi 1D-Ising chain material $CoNb_2O_6$. After successful synthesis, the low-temperature magnetic properties of the materials were investigated by measuring the magnetization, ac susceptibility, and the specific heat and the magnetocaloric effect as well as by means of neutron diffraction experiments. In this chapter, the single-crystal growth technique, namely the optical floating-zone technique, the measurement techniques, which were used for the determination of the magnetic and thermodynamic properties of the samples, and the sample alignment procedure for the measurement of $CoNb_2O_6$ in transverse magnetic fields are described.

2.1 Single Crystal Growth of Oxide Compounds

Single-crystal material was synthesized using a combination of solid-state reaction and optical floating-zone techniques. The optical floating-zone technique used for the synthesis of single-crystal material requires mechanically stable, polycrystalline feed rods with well-controlled stoichiometry. The preparation of polycrystalline rods from powder material is a common technique as a first step of the synthesis of single crystal material [34, 35]. The oxide starting materials were mixed and heated for several hours to initiate the solid-state reaction. The material is ground into a powder and pressed into a rod shape using rubber tubes and a hydrostatic press.

The preparation chain for oxide starting rods of $CoNb_2O_6$ is shown in Fig. 2.1. Different approaches for the preparation of $CoNb_2O_6$ are described in Refs. [34–38]. As described in Refs. [39] and shown in Fig. 2.1 (a), the first step is the stoichiometric inweight of the starting materials Co_3O_4 (black, 99.995 % purity) and Nb_2O_5 (white, 99.9985 % purity) for the prereaction. The two powders were mixed in a ball mill and heated in a box furnace at 1100°C for 48 hours. The blue color of the material in Fig. 2.1 (b) after heat treatment is an indication of the successful reaction in large parts. The powdered material was then ball-milled and inserted into a rubber tube, as shown in Fig. 2.1 (c). Figure 2.1 (d) displays the compacted powder rod subsequent to the application of hydrostatic pressure. After undergoing a final sintering process for 15 hours at 1400°C under oxygen flow, the rod became more stable and acquired a dark gray color, as shown in Fig. 2.1 (e). In later approaches, the sintering process was reduced to 12 hours at 1100°C in air atmosphere. In these approaches, the rods remained their blue color.

The polycrystalline rods were mounted inside of the quartz chamber of a Crystal Systems

Corporation four-mirror optical floating zone furnace as shown in Fig. 2.2 (a) and (b). The combination of the four ellipsoidal mirrors and four halogen lamps allows for the melting of the polycrystalline rods in a localized area. This is illustrated in Fig. 2.2 (c). By slowly moving the molten zone upwards, the atoms may crystallize in the desired stoichiometry and structure. The quartz chamber allows to have different gaseous atmospheres around the molten zone. For the single-crystal growth of $CoNb_2O_6$, a 50:50 Argon-Oxygen mixture was used. The typical growth rate (moving rate of the molten zone) was 5 mm/h.

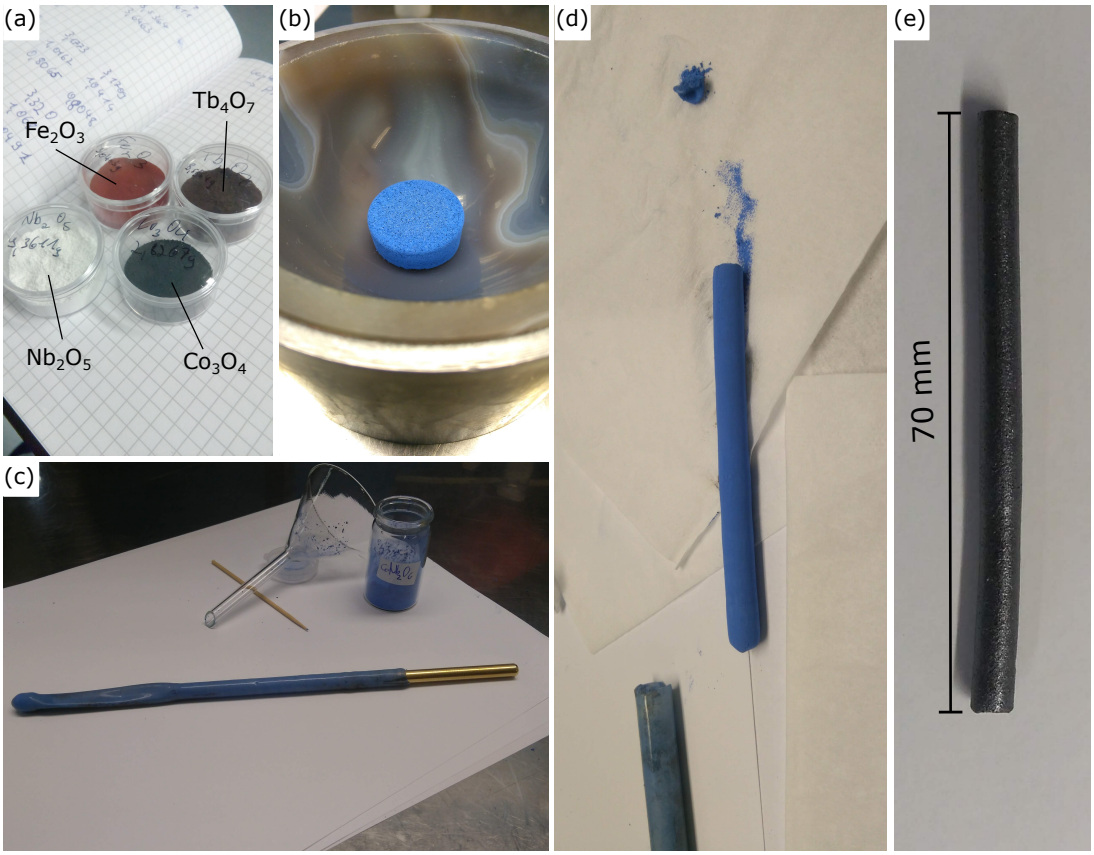

Figure 2.1: Preparation chain for the synthesis of oxide compounds. (a) The starting materials were weighed with the correct stoichiometry. (b) After mixing and heating, the Co_3O_4 and Nb_2O_5 reacted to form $CoNb_2O_6$, as indicated by the change in color from gray to blue. (c) The pre-reacted powder is filled into a rubber tube in preparation for hydrostatic pressing. (d) After the application of hydrostatic pressure and the removal of the rubber tube, the pressed powder forms a rod. (e) The polycrystalline rod gains enhanced rigidity after the sintering process. Figure taken from Ref. [39].

For the investigation of $CoNb_2O_6$, four samples were prepared from the synthesized single crystalline material. The longitudinal susceptibility and the magnetization was measured using a sample with a size of $1.8\times2.4\times2.6\,\mathrm{mm}^3$ along the a-axis, c-axis, and b-axis weighing

62.6 mg. The heat capacity measurement in a PPMS system in zero magnetic field was carried out using a sample without defined orientation weighing 17.6 mg. For the extensive studies of the transverse susceptibility and the heat capacity in transverse magnetic field and down to mK-temperatures, a spherical sample with a diameter of 2.7 mm and a mass of 67.8 mg was prepared. The spherical shape of the sample is essential for two reasons: (i) the spherical shape prevents distortions of the local magnetic field present in edges and corners of other sample geometries and (ii) the demagnetization factor of a spherical sample is constant for any direction of an external magnetic field. This is in particular important for investigations of the effects of a misaligned magnetic field.

The synthesis of $TbFeO_3$ is described in Refs. [15, 39–41]. The synthesis of single crystal $TbFeO_3$ started with stoichiometric amounts of Tb_4O_7 (99.998 % purity) and Fe_2O_3 (99.998 % purity). The two materials can be seen in Fig. 2.1 (a) with the brown and the red color, respectively. After mixing the two compounds, the mixture was heated at 1100°C for ten hours. The resulting prereacted powder was then ball milled, filled into rubber tubes and pressed to a polycrystalline rod using hydrostatic pressure. The rods were then sintered for 12 hours at 1100°C and mounted in the optical floating-zone furnace as shown in Fig. 2.2 (b). For the single-crystal growth of $TbFeO_3$, a pure oxygen atmosphere at ambient pressure and a growth rate of 5 mm/h was used.

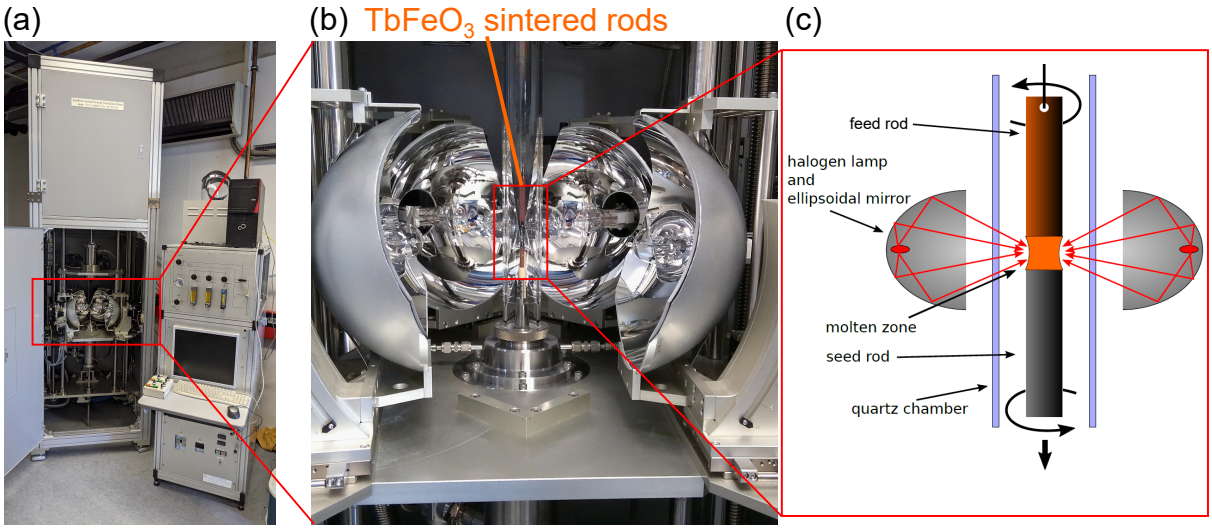

Figure 2.2: Crystal Systems Corporation optical floating zone furnace. (a) Outside view of the optical floating zone furnace. (b) Mirror stage of the optical floating zone furnace with $TbFeO_3$ starting rods inside of the quartz chamber. (c) Schematic of the optical floating-zone technique. Adapted from Ref. [39].

The presented data on $TbFeO_3$ in this work was obtained using different cuboidal samples prepared from the synthesized single crystals. A small sample used for the transverse

susceptibility measurements has a size of $1 \times 1.1 \times 1.5\,\mathrm{mm}^3$ along the a-axis, b-axis, and c-axis weighing 13 mg. For the heat capacity measurements, a sample with the same size weighing 13.1 mg was used. For the longitudinal susceptibility and the neutron diffraction experiments a sample was prepared with a size of $2 \times 2.5 \times 3\,\mathrm{mm}^3$ along the a-axis, b-axis, and c-axis weighing 94 mg.

2.2 Cryogenic Techniques

In this thesis, different types of cryostats were used for the investigations of quantum effects in magnetic compounds. Measurements above 1.4 K were carried out using two different types of helium-4 cryostats, a Quantum Design Physical Property Measurement System (PPMS) and the Oxford Instruments S16 magnet system.

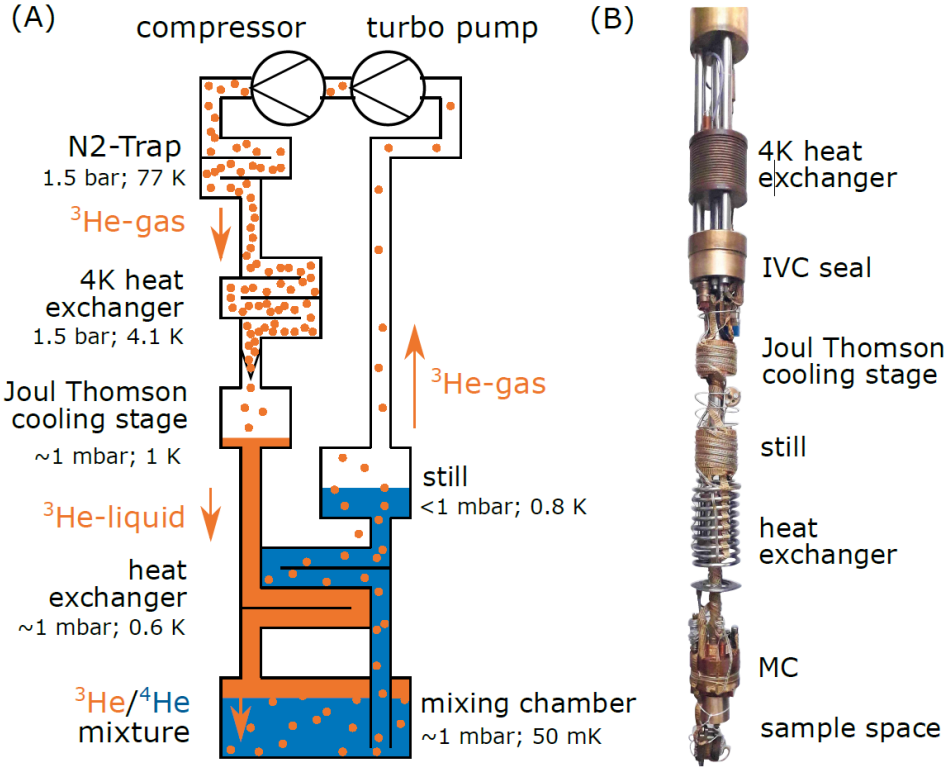

Figure 2.3: Dilution refrigerator with Joule-Thomson stage used in this work. (A) Illustration of the working principle of a dilution refrigerator. (B) The Dilution refrigerator used in the course of this work. Figure taken from Ref. [33].

The PPMS is equipped with a 14 Tesla magnet and allows us to measure the heat capacity, the ac susceptibility, and the magnetization using commercial and custom-made setups at temperatures between 1.8 K and 400 K. The S16 is equipped with a 16 Tesla magnet and with a variable temperature insert (VTI) providing temperatures between 1.4 K and 300 K. This versatile system permits the use of custom made setups. In this work, a custom

made susceptometer attached to a rotational stage at the end of a sample stick was used. In the case of these two helium-4 cryostats, low temperatures are achieved by vacuum pumping on liquid helium through thin capillaries (PPMS) or a needle valve (S16).

For studies at milli-Kelvin temperatures, a JT dilution refrigerator (DR) insert was used, which was equipped with a Joule-Thomson stage. This insert was combined with either a susceptometer developed by F. Rucker or with a hard axis heat capacity setup conceived by C. Duvinage/A. Wendl. The working principle of the DR insert is illustrated in Fig. 2.3 (A). An input pressure of approximately 1.6 bar is provided by a compressor at the input side. After passing through a nitrogen trap, the compressed helium is cooled down in a 4 Kelvin heat exchanger. The compressed helium then expands in the Joule Thomson stage resulting in a liquefaction of the helium. After passing through a second heat exchanger, the liquid helium enters the mixing chamber. In the mixing chamber, the liquid helium separates into two regions: one with concentrated helium-3 and the other with a mixture of helium-3 and helium-4 below. The helium-3 diffuses to the still with a lower helium-3 concentration. The helium-3 is then extracted from the still and transferred to the compressor via vacuum pumping. The DR insert used in this work is shown in Fig. 2.3 (B). The essential parts are labeled. The DR insert was used in combination with a 9 T-4.5 T 2D vector magnet. When the insert is rotated inside of the vector magnet, this combination allows to apply the magnetic fields in any direction with respect to the crystalline orientation of the sample.

2.3 Measurement Setups

The main results of this work concern the measurement of thermodynamic quantities, namely the magnetic ac susceptibility and the heat capacity. In the following, the corresponding measurement setups and the underlying working principles are presented.

2.3.1 Susceptibility Setups

The measurement of the transverse magnetic susceptibility has been established as a method of choice for the investigations of the physics of Ising systems and for the determination of their magnetic phase diagrams [31, 42, 43]. In the case of the measurement of the longitudinal susceptibility, a small oscillating excitation field is applied parallel to a static magnetic field. In contrast, for the measurement of the transverse susceptibility, the excitation field is applied perpendicular to the static magnetic field. The measurement of transverse susceptibility is a time-efficient process that allows for the extraction of detailed information about different magnetic phases and their extent. The transverse

susceptibility is a particularly useful technique for anisotropic samples. Additionally, a transverse susceptibility setup can be combined with a variety of different magnet setups. In particular for this study, a vector magnet in combination with a insert that can be rotated inside of the helium dewar was required for the precise alignment of the sample with respect to the magnetic field. This experimental setup also allows for the systematic study of the influence of tilting the magnetic field away from a transverse-field orientation [31].

Two setups for the measurements of the transverse susceptibility were used. Both designs were conceived by F. Rucker [44, 45]. Fig. 2.4 (a) shows susceptometer setup 1. This setup is made of a combination of oxygen-free copper and sapphire glass. It was designed to achieve good thermal coupling of the sample to the thermal bath. It consists of one primary coil wound on a sapphire tube and two secondary coils inside of the sapphire tube. The susceptometer body is made of oxygen-free copper to ensure good thermal coupling down to milli-Kelvin temperatures. The sample was affixed to a sapphire rod using GE varnish to achieve optimal thermal coupling with minimal background signal.

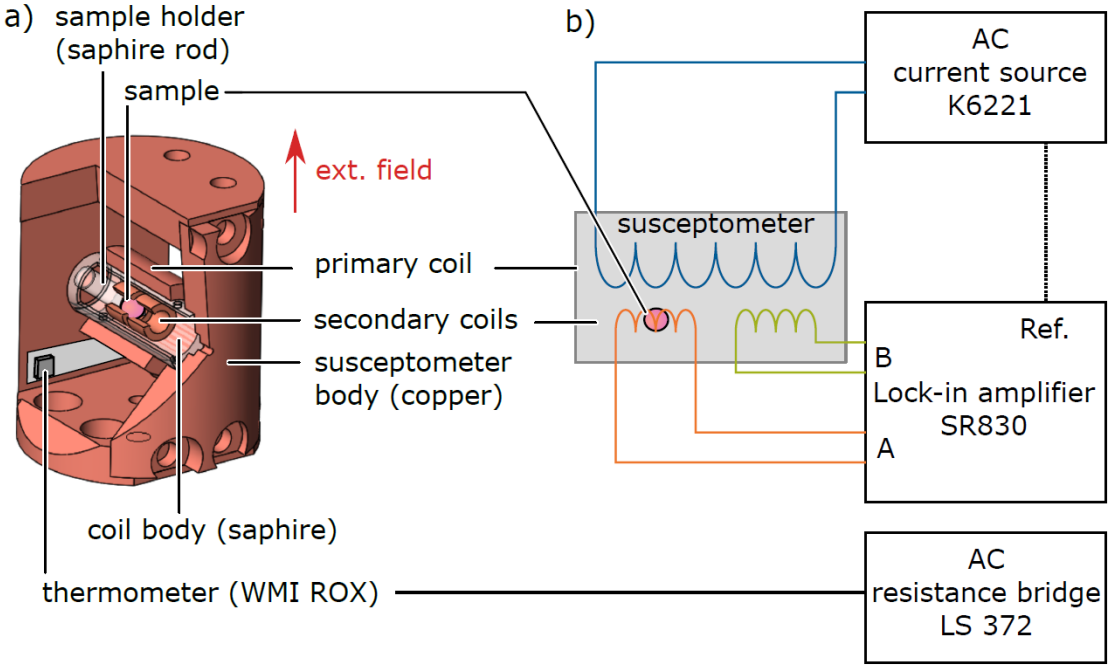

Figure 2.4: Setup for transverse susceptometry. a) CAD drawing of the susceptometer used for the measurement at milli-Kelvin temperatures. b) Overview of the electrical connections between the measurement electronics and the different coils of the susceptometer. Figure taken from Ref. [33].

Susceptometer setup 2 was made of plastic and is shown in Fig. 2.5. It was designed to minimize the background signal induced by the susceptometer itself. Its compact size

also allows for use with a rotational stage, enabling the study of angle dependence of the ac susceptibility when the sample orientation is changed relative to the magnetic field direction. The working principle of this susceptometer is equivalent to the susceptometer setup 1 described above. This low-noise design of the susceptometer required exchange gas inside the cryogenic environment to ensure sufficient thermal coupling of the sample.

A LakeShore ruthenium oxide thermometer labeled with WMI ROX was attached to the susceptometer body to ensure accurate temperature readings of the samples temperature. This thermometer was calibrated in different magnetic fields in an earlier work [44]. The resistance of the WMI ROX thermometer was recorded using a LakeShore LS372 AC resistance bridge. This device converts the measured resistance into a temperature. In analogy to Refs. [33, 44], the magnetic-field correction of the measured temperature was carried out during the data processing.

In Fig. 2.4 (b), the electrical wiring of the measurement devices is illustrated. The primary coil of the susceptometer is driven by a Keithley K6221 AC current source. The driving frequency used for the measurement of the transverse susceptibility was 911 Hz while the amplitude was chosen to be 1 Oe. The magnetic field of the primary coil induces an AC voltage in the secondary coils, that is recorded using a Stanford Research SR830 lock-in amplifier. The lock-in amplifier uses a reference signal for the phase-locked loop provided by the K6221.

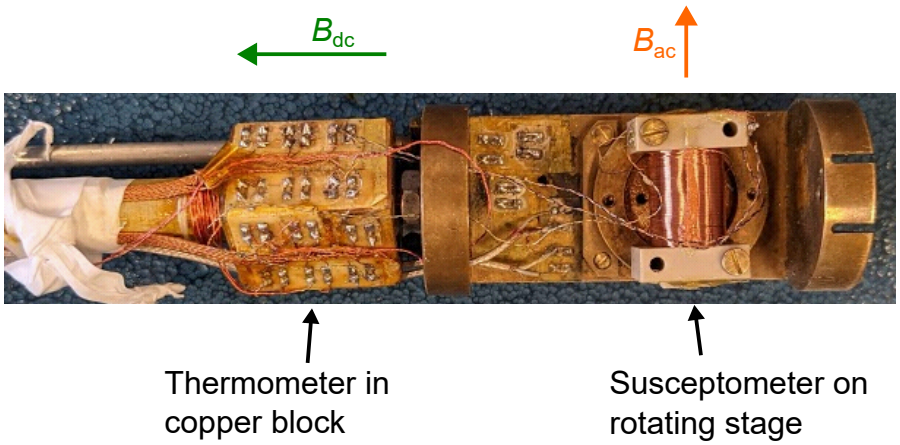

Figure 2.5: Setup used for the measurement of the transverse susceptibility of $TbFeO_3$. The rotating stage allowed to switch between a longitudinal and a transverse susceptibility measurement configuration and to study the angular dependence of the susceptibility.

The susceptometer is designed such that the voltages induced in the two secondary coils cancel each other when no sample is placed inside. The sample placed inside one of the

secondary coils adds an additional voltage contribution proportional to the ac susceptibility $\chi_{\mathrm{ac}}^{\mathrm{sample}}$ of the sample. The voltage induced in the susceptometer can be written as

$$U_{\mathrm{ind}}^{\mathrm{sample}} = U_{\mathrm{coil\ 1}}^{\mathrm{vacuum}} + U_{\mathrm{coil\ 1}}^{\mathrm{sample}} - U_{\mathrm{coil\ 2}}^{\mathrm{vacuum}} = \mu_0 H_{\mathrm{exc}} \omega A N_s \sin(\omega t) \chi_{ac}^{\mathrm{sample}} f_{\mathrm{sample}} \tag{1}$$

with H_{exc} the magnitude of the ac excitation field, ω the driving frequency of the excitation field, N_s the number of windings of one of the secondary coils and f_{sample} the filling factor of the samples volume with respect to the volume of the inside of the secondary coil [33, 44–46].

2.3.2 Heat capacity Setup

The heat capacity of a sample is defined as the amount of heat which is required to change the temperature of the sample. The heat capacity was measured using a setup optimized for the thermal relaxation method [33]. Fig. 2.6 (A) illustrates the working principle of a heat capacity setup. The experimental setup consists of a platform weakly coupled to a thermal bath with a coupling constant k_l. The sample of interest is placed on the platform with a large coupling constant $k_s \gg k_l$. A heater mounted to the platform supplied the heating power $P(t)$. This experimental setup can be described using two coupled differential equations [33, 47]. The incoming and outgoing heat flux at the platform is described by

$$P(t) = C_p \frac{dT_p}{dt} + k_s(T_p - T_s) + k_l(T_p - T_0) \tag{2}$$

where P(t) is the heating power applied to the platform and C_p and T_p describe the platform heat capacity and platform temperature, T_s and T_0 the sample temperature and the bath temperature. k_s describes the thermal coupling between sample and platform and k_l the thermal coupling between platform and bath.

The second equation describes the incoming heat flux from the platform to the sample

$$C_s \frac{dT_s}{dt} = k_s(T_p - T_s) \tag{3}$$

with C_s being the samples heat capacity.

Under ideal conditions, the bath temperature remains constant during the measurement whereas the temperature of the sample and the platform temperature can be assumed to be equal.

Fig. 2.6 (B) displays a typical time dependence of the temperature of the platform (T_p) during a measurement. Phase I represents the period when the heater is off and the temperature is equal to the bath temperature T_0. In phase II, the heater is switched on causing an exponential increase of T_p over time. In phase III, when the heater is switched off, T_p relaxes exponentially back to the bath temperature. This characteristic temperature profile may be used to infer the heat capacity of the sample using a fitting algorithm reported by Hwang et al. [47]. Typical temperature rises used for the thermal relaxation experiments aimed on 2% of the current temperature.

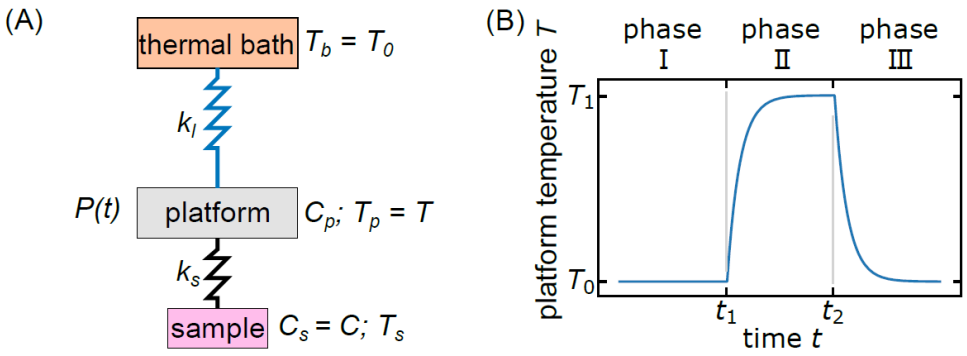

Figure 2.6: Working principle of the thermal relaxation method for the measurement of the heat capacity. (A) Basic sketch of the different components and their thermal couplings in a heat capacity setup. (B) Characteristic temperature variation recorded during the three phases of a heat pulse. Figure taken from Ref. [33].

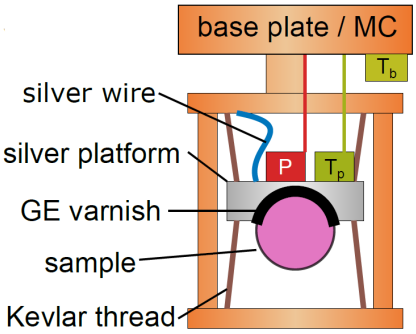

Figure 2.7: Schematic illustration of the experimental realization of the thermal relaxation method for the measurement of the heat capacity. The platform and bath thermometer are shown in green. The heater is shown in red. Figure taken from Ref. [33].

Fig. 2.7 displays a schematic illustration of the experimental setup for measuring the heat capacity. The experimental setups were designed by C. Duvinage and A. Wendl [32, 33]. The frame surrounding the setup is made of oxygen-free copper. It is mounted rigidly to the base plate that provides the temperature bath. A silver platform is connected

to the copper frame using Kevlar threads. A heater (P) and a thermometer (T_p) are attached to the backside of the silver platform. The sample is attached to the other side of the silver platform using GE varnish. The thermal link between the platform and the bath is provided by the electric leads of the heater and the thermometer attached to the platform as well as by the Kevlar threads. Depending on the heat capacity of the sample, an additional silver wire may be used to adjust the thermal link between base plate and silver platform. For the measurement of the specific heat of $CoNb_2O_6$, no silver wire was used.

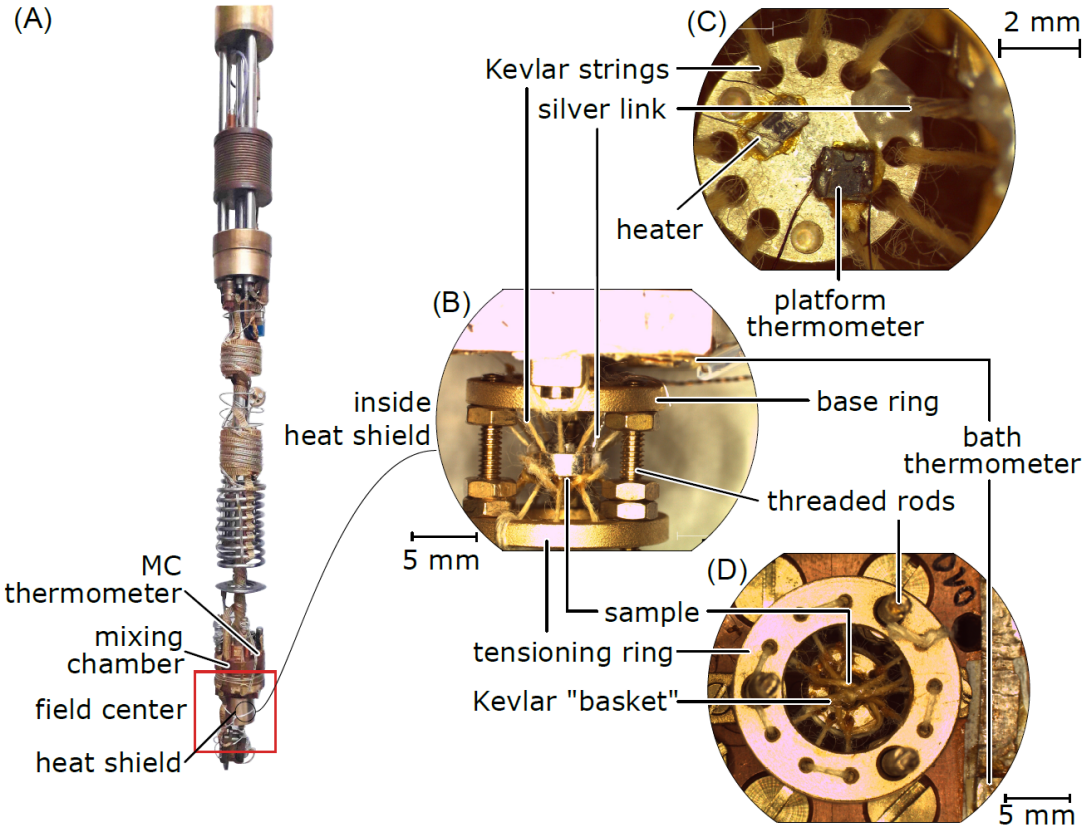

Figure 2.8: Experimental setup for the measurement of the heat capacity of $CoNb_2O_6$. (A) Dilution refrigerator with Joule-Thomson stage used in this work. The heat capacity setup I was mounted to the bottom of the mixing chamber. (B) Side view of the heat capacity setup I with the frame consisting of a base ring and a tensioning ring and the silver platform in the middle. (C) Backside of the silver platform with the heater and the platform thermometer. (D) Top view of the heat capacity setup with the sample fastened to the silver platform using additional kevlar strings. Figure taken from Ref. [33].

The experimental realization of the heat capacity measurement setup I is shown in Fig. 2.8. Fig. 2.8 (A) displays an overview of heat capacity setup I as mounted at the bottom of the mixing chamber of the dilution refrigerator. Fig. 2.8 (B) presents a detailed view of

the heat capacity setup. The silver platform and the copper frame were both gold plated. The 1-kΩ SMD-chip heating resistor and the platform thermometer (Lakeshore Rox-BR 102A) can be seen in Fig. 2.8 (C). As shown in Fig. 2.8 (D), an additional Kevlar thread forming a basket was used to attach the samples to the platform. For the temperature measurement of the platform and the bath thermometer, LS372 and LS370 Lake Shore resistance bridges were used, respectively. The heater was connected to a Keithley K6221 current source.

For measurements of the heat capacity of $TbFeO_3$ under magnetic fields applied along the hard magnetic axis, a modification of the commercial heat capacity setup of the Quantum Design PPMS was used. This heat capacity setup II was conceived by C. Duvinage as reported by N. Bonacic [32] and is shown in Fig. 2.9 (a). This design consists of a thin aluminum bridge with a small platform in the middle on which the sample is placed. On the backside of the platform, a 1-kΩ heating resistor and a thermometer (Cernox CX-1010-BG) are located. Due to the limited rigidity of this setup for samples with very large magnetic torque, as observed in $TbFeO_3$, an additional setup was built for the PPMS for future measurements. This new setup for the PPMS inspired by setup I is shown in Fig. 2.9 (b).

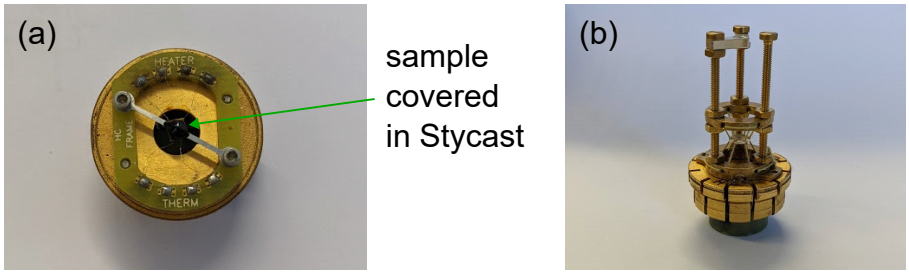

Figure 2.9: Heat capacity setup used for the measurement of the heat capacity of $TbFeO_3$ in a Quantum Design PPMS system under magnetic fields applied along the hard magnetic axis. The designs were conceived by C. Duvinage and part of the work by Bonacic and Wendl [32, 33]. (a) Setup II with a aluminum bridge. (b) New design for the PPMS inspired by setup I.

2.3.3 Software Implementation of the heat pulse method

The initial version of the algorithm used for data recording was implemented in LabVIEW by A. Wendl [33]. This algorithm enabled the temperature variation during a heat pulse to be recorded with a waiting time before the heater is switched on, a heating time and a relaxation time, which all had to be chosen for every single heat pulse in advance. The processing of the data was entirely done later using Python.

Inspired by the heat capacity measurement algorithm of the commercially available Quantum Design PPMS [48], several modifications were implemented in the course of this thesis to increase the efficiency of the measurements.

A central modification concerned the timing parameter, namely τ, which is now used as the input parameter for each heat pulse. Instead of manually selecting the waiting time, heating time, and relaxation time for each heat pulse, the new approach involves a single timing parameter, with the waiting time, heating time and relaxation time described in units of τ multiplied with fixed factors for all heat pulses. This also allows the value of τ to be automatically selected using the result of the exponential fit of the previous heat pulse.

A flowchart visualizing the different steps of the measurement algorithm is shown in Fig. 2.11. Step 1 (stabilizing temperature), and step 3 (exponential fitting) were added during the course of this thesis. The algorithm in step 1 was implemented to ensure a stable temperature before each heat pulse. The algorithm checks whether the temperature is within a chosen stability window, expressed as a percentage of the current temperature, during the characteristic time τ.

Step 3 involves an exponential fitting algorithm for both the heating and relaxation parts of the recorded data. Two criteria were used to determine the satisfactory extraction of the time constants τ: (i) the difference between the time constants extracted from the heating and relaxation parts of the temperature profile, and (ii) the difference between the initial time constant τ and the averaged time constants extracted from the exponential fits. The heating pulse is repeated at the current temperature and magnetic field if either of these criteria is not met. In case of a bad thermal coupling between the sample and the platform of the heat capacity setup, the first data points of the heating phase and the relaxation phase may be disturbed due to the so called τ_2-effect [33]. Because this effect is not addressed by the simple exponential fit employed during the measurement, the first data points of the heating phase and the relaxation phase can be excluded for the fit.

The option was implemented, to choose between using the previous time constant and an automatically adjusted current applied to the heater or using manually selected values for the time constant and heater current. In general, the automatic adjustment of time constant and heater current was preferred. For a more systematic analysis of the glassy regimes in $CoNb_2O_6$, manually selected values for time constant and heater current were found to be advantageous.

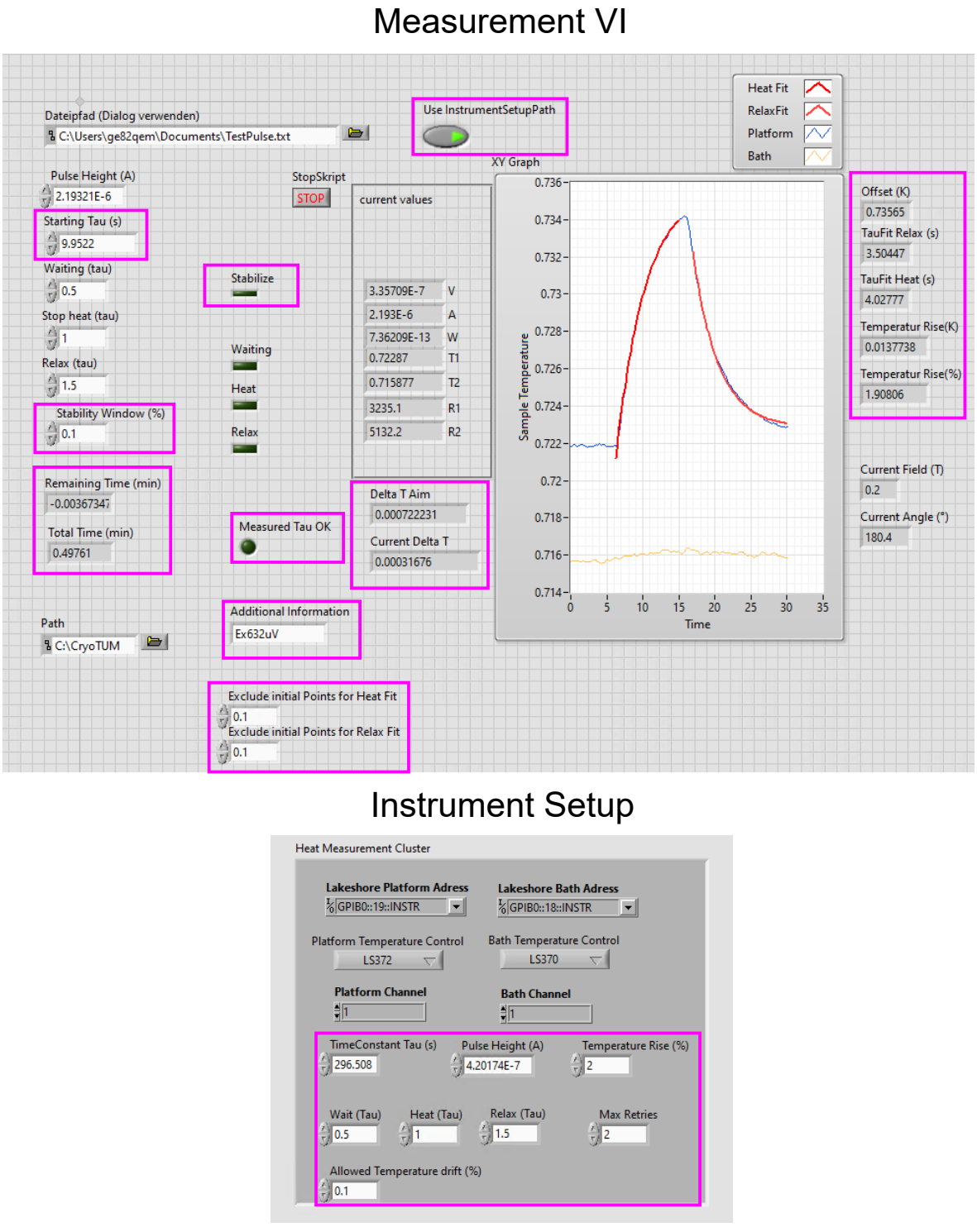

Figure 2.10: Front panel of the LabView VI for the measurement of the heat capacity implemented by A. Wendl and heat measurement cluster in the Instrument setup of the S16 EPMS Software. Modifications are marked with pink. On the left side of the measurement VI, input parameters of the measurement are shown, in the middle, the progress of the measurement is shown and on the right side, the results of the exponential fit are displayed.

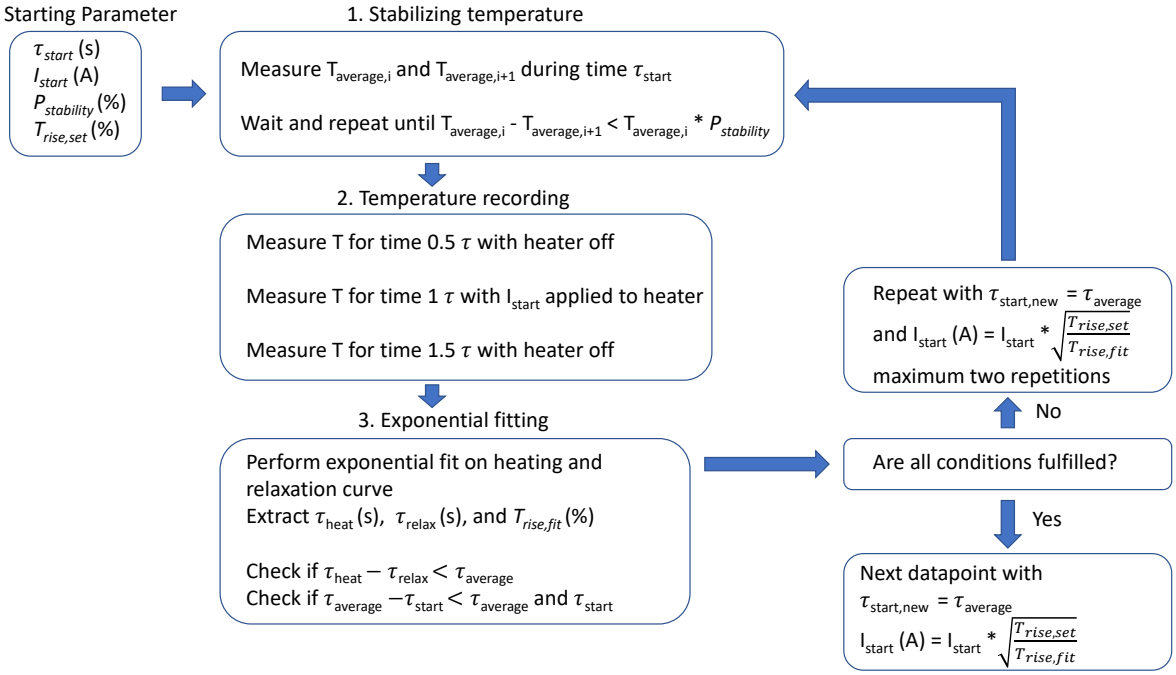

Figure 2.11: Flowchart describing the measurement algorithm. Step 1 and step 3 were added in the course of this thesis whereas step 2 was only slightly modified.

2.3.4 Data processing for the heat pulse method

A first version of the evaluation of the heat capacity was implemented in Python by A. Wendl based on the work from Hwang et al. [47]. The model presented by Hwang et al. consists of two coupled differential equations as described in section 2.3.2. These differential equations are transformed to obtain an expression for the temperature variation during a heat pulse sequence:

$$T(t) - T(0) = h \cdot H(t) + q \cdot Q(t) + s \cdot S(t) \tag{4}$$

with the following characteristic functions

$$H(t) = P(t) - C_p V(t) \tag{5}$$

$$V(t) = \left.\frac{dT}{dt'}\right|_0^t \tag{6}$$

$$Q(t) = \int_0^t P(t')dt' \tag{7}$$

$$S(t) = \int_0^t T(t')dt' \tag{8}$$

where $T = T_p(t) - T_1(t)$ describes the change of the platform temperature with T_1 the extrapolated baseline temperature of the platform in thermal equilibrium. The characteristic functions can mostly be extracted from the measured data with only knowledge of the platforms heat capacity C_p being required in advance. Equation 4 can then be used for a least-squares fit to extract h, q and s. As described in Ref. [47], these three quantities can then be used to calculate the thermal couplings k_l and k_s as well as the corresponding time constants τ_1 and τ_2 describing the time required for the thermal equilibration between platfrom and bath and between sample and platform, respectively, and finally the samples heat capacity C_s.

2.3.5 Magnetocaloric Measurements

The heat capacity setup provides the means to measure temperature variations during magnetic field sweeps, also known as magnetocaloric field sweeps. This method can provide insight into the nature of phase transitions and their position in the magnetic phase diagram. In addition, the change in entropy can be derived from the measured temperature variation. This section describes the data processing to extract the change in entropy from the change of the temperature of the platform during a magnetocaloric field sweep.

Following relationship between the change in entropy and the change in temperature can be derived, as shown in Ref. [49].

$$\left.\frac{dS}{dH}\right|_T = -\frac{k_l}{T_s}(T_s - T_B)\frac{1}{\dot{H}} - \frac{C_s}{T_s}\frac{dT_s}{dH} \tag{9}$$

The thermal coupling between the bath and platform, k_l, and the heat capacity of the sample, C_s, must be determined in advance using the thermal relaxation technique.

Figure 2.12 presents the steps for obtaining entropy from a magnetocaloric field sweep. Figure 2.12 (a) displays the platform temperature and the bath temperature as obtained from a magnetocaloric field sweep. The magnetic-field calibration of the thermometers described in Refs. [33, 44] was already applied to the data shown in Fig. 2.12 (a). A constant offset was subtracted to correct the deviation between the temperatures of the bath and the platform at the beginning of the field sweep.

In Figure 2.12 (b), the temperature difference is shown between the bath and platform temperatures. Using equation 9 and the results of the preceding heat capacity measurements, $\mathrm{d}S/\mathrm{d}B$ can be calculated to receive the magnetic field dependence shown in Fig.

2.12 (c). After integrating $\mathrm{d}S/\mathrm{d}B$, the change of entropy as a function of magnetic field is obtained. The corresponding plot is shown in Fig. 2.12 (d).

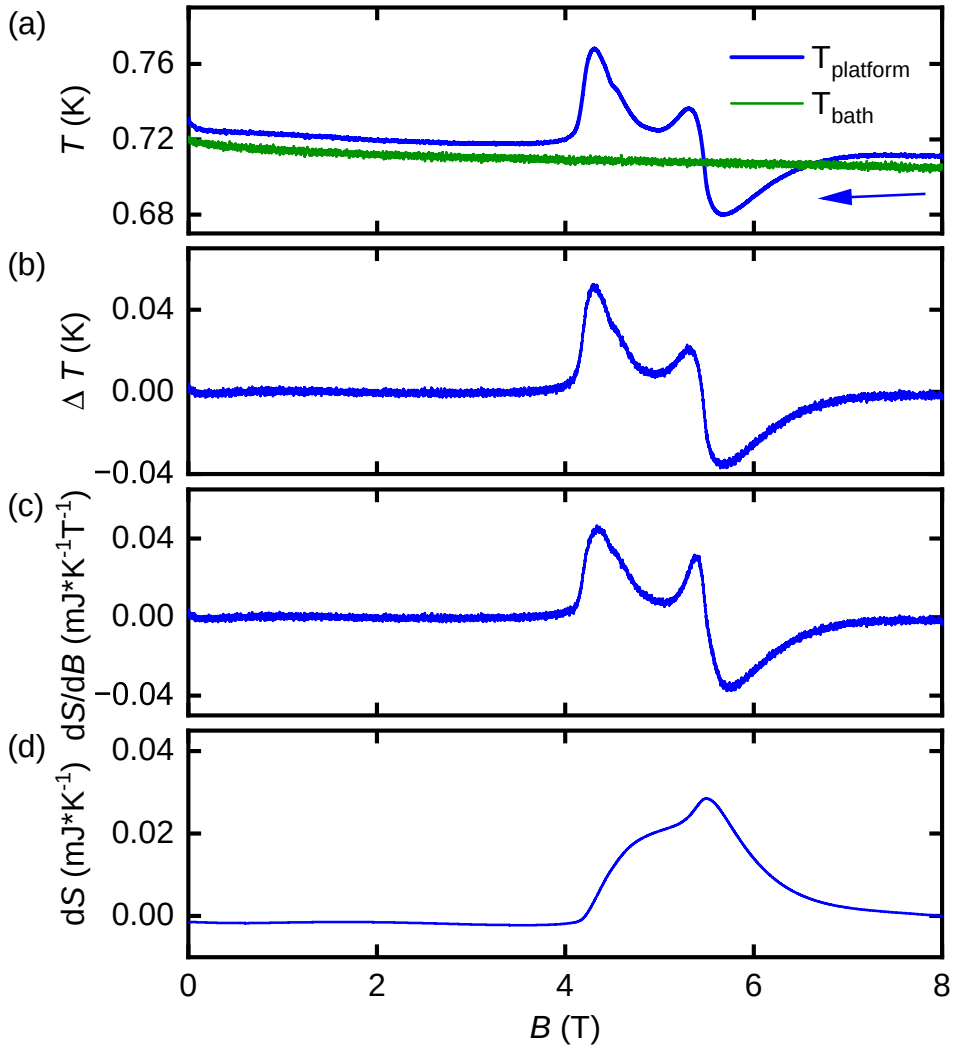

Figure 2.12: Data processing of a magnetocaloric field sweep of $CoNb_2O_6$ in a transverse magnetic field. (a) Recorded temperature of the sample platform and the thermal bath. (b) Temperature difference between the platform and the thermal bath. The temperature difference visible in panel (a) between the two curves in particular visible below 3 T and above 7 T was manually compensated for using a constant offset. (c) Derivative of the change of entropy calculated using equation 9. (d) Change of entropy obtained after the integration of the derivative of the change of entropy in (c).

2.4 Orientation of the Sample with Respect to the Magnetic Field

The precise alignment of the magnetic field with respect to the orientation of the sample is crucial in anisotropic systems. The challenging part is, to align the magnetic field

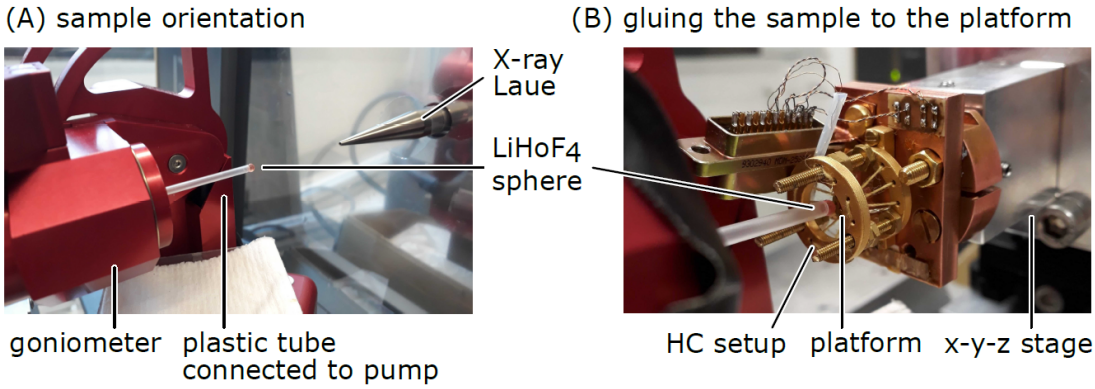

Figure 2.13: Sample mounting process using a Laue diffractometer and a goniometer presented on the example of a $LiHoF_4$ sphere mounted to the heat capacity setup. (A) The sample at the tip of a plastic tube during the Laue alignment procedure. (B) Transfer of the aligned sample from the plastic tube to the heat capacity setup. Figure taken from Ref. [33].

parallel to the hard axis within the tenth of a degree. In preparation for the measurement of the transverse susceptibility and the heat capacity of $CoNb_2O_6$, a spherical sample was prepared and aligned using a special setup for the alignment using a Laue diffractometer. After the sample is glued to the sample holder in the right orientation, the magnetic field of a vector magnet is aligned with respect to the crystalline orientation of the sample. In the following, this orientation process is described in detail.

The sample mounting process is shown in Fig. 2.13. The spherical sample is placed at the tip of a plastic tube, which is connected to a vacuum pump, as shown in Fig. 2.13 (A). The plastic tube is attached to the goniometer of a X-ray Laue diffractometer. This allows the sample to be correctly aligned with respect to the crystallographic directions. Once the sample is aligned, it can be transferred to the experimental setup of choice. This second step of the mounting process shown in Fig. 2.13 (B) with the heat capacity setup as an example is described in Ref. [33]. The experimental setup itself is mounted on an x-y-z translation stage. This allows the sample to be transferred very carefully. The sample is glued to the platform of the heat capacity setup using GE varnish. After the GE varnish has dried, the orientation of the sample has typically changed by a few degrees. The sample mounting process for the susceptibility setup is the same.

Various systematic susceptibility scans as a function of angle and magnetic field strength were used to evaluate the actual sample orientation, which could be misaligned due to the sample mounting process or imperfections of the experimental setup or the dilution insert. Rough knowledge of the orientation of the sample (within a few degrees) is obtained from the sample mounting process.

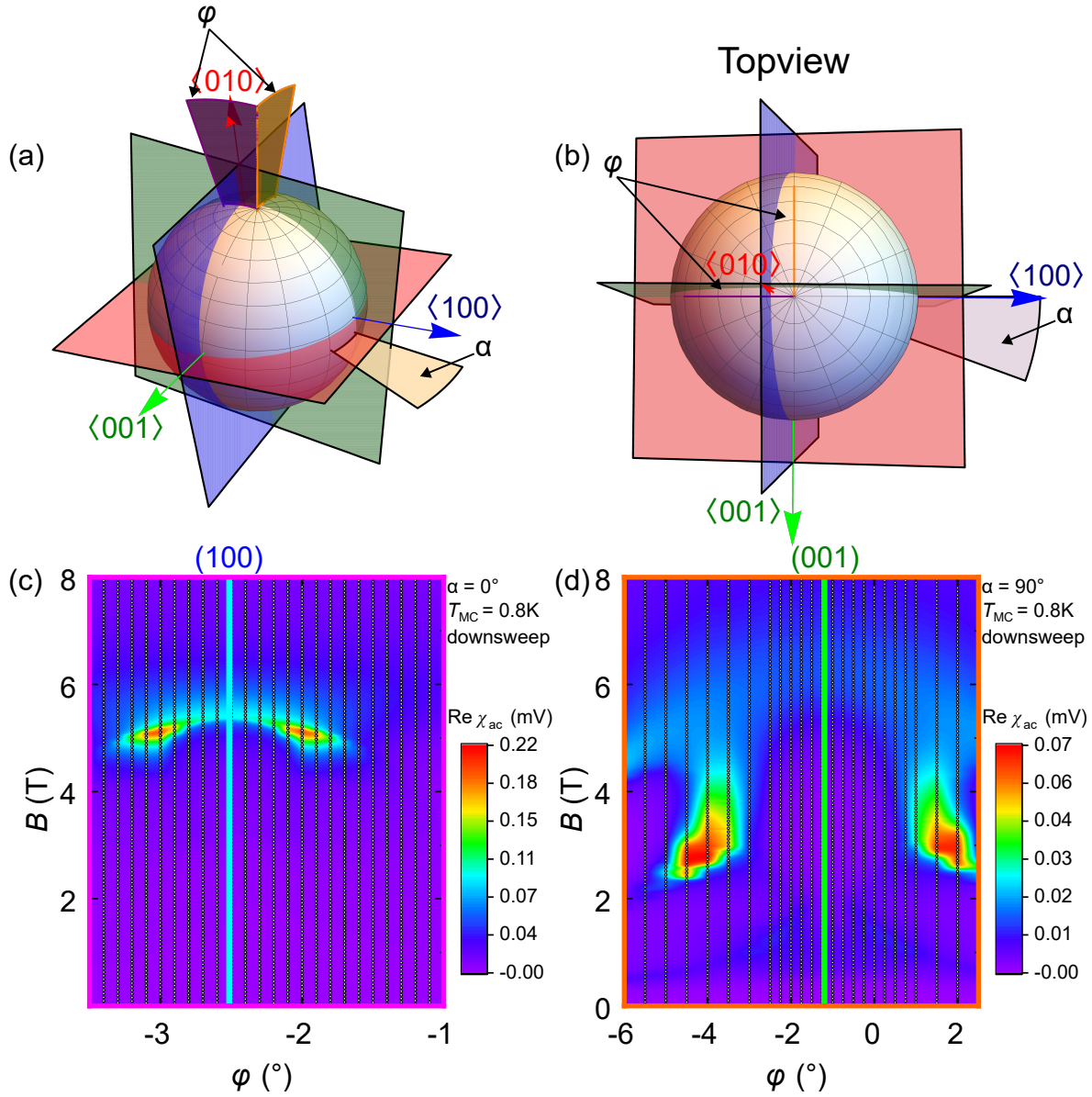

Figure 2.14: First part of the process for the orientation of the magnetic field towards the ⟨010⟩ direction of $CoNb_2O_6$. (a) Visualization of the major crystallographic planes and directions of the orthorhombic system with respect to the two angles α and φ defining the direction of the magnetic field. The directions of the two scans shown in (c) and (d) are displayed as purple and orange slices, respectively. (b) Top view of (a). (c) and (d) Color maps of the measured susceptibility as function of magnetic field and angle φ for fixed angles $\alpha = 0°$ and $\alpha = 90°$, respectively

Any magnetic field direction can be described in spherical coordinates by the polar angle φ and the azimuthal angle α, as shown in Fig. 2.14 (a). The direction of the b-axis of the sample, which is slightly misaligned from the z-axis of the vector magnet, can also be described by these two angles, as illustrated in Fig. 2.14 (a) and (b). To better visualize the process of determining the orientation of the sample, the misalignment angles in Fig.

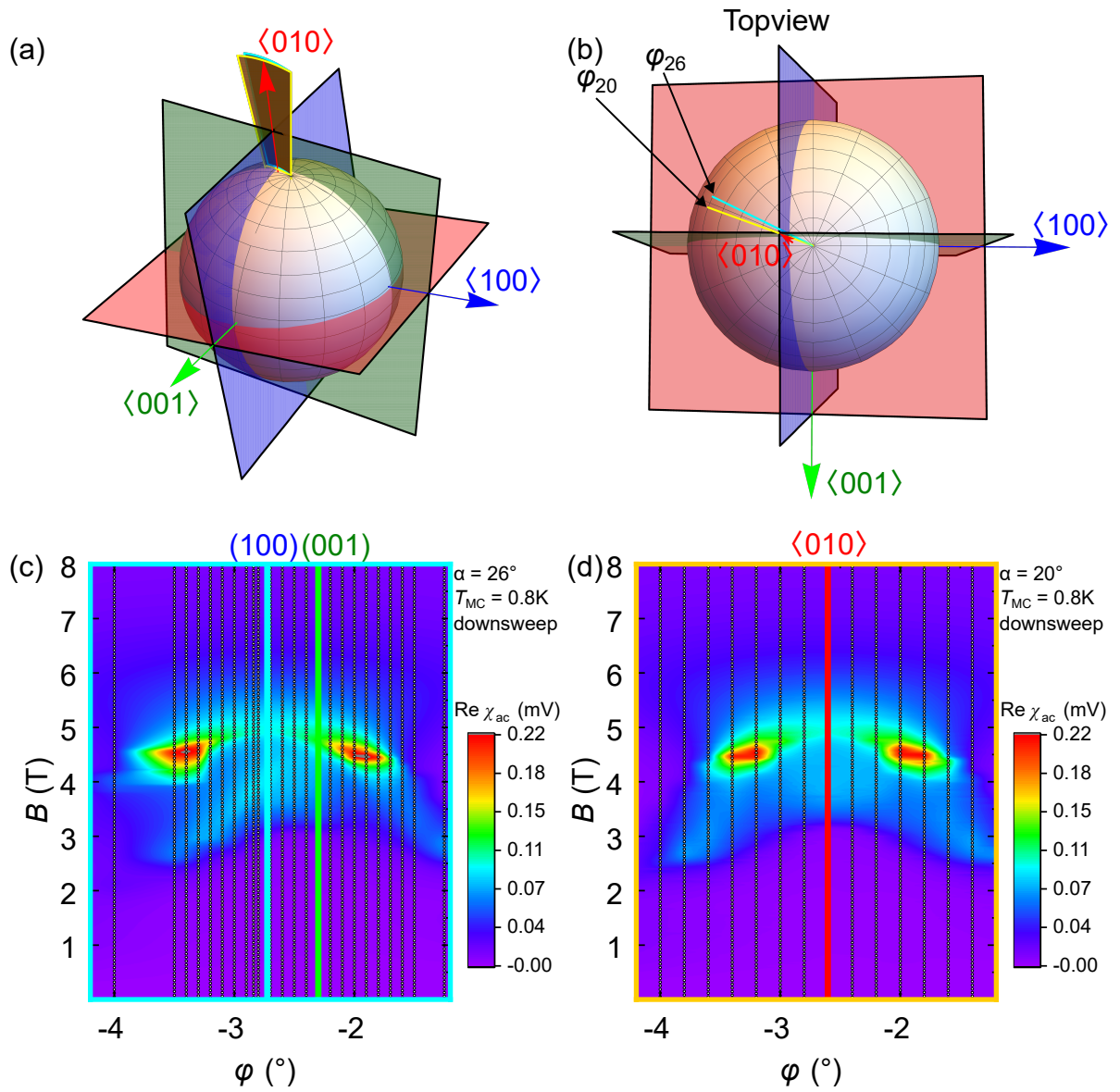

Figure 2.15: Second part of the process for the orientation of the magnetic field towards the ⟨010⟩ direction of $CoNb_2O_6$. (a) Visualization of the major crystallographic planes and directions of the orthorhombic system with respect to the two angles defining the direction of the magnetic field. The directions of the two scans shown in (c) and (d) are displayed as cyan and yellow slices, respectively. (b) Top view of (a). (c) and (d) Color maps of the measured susceptibility as function of magnetic field and angle φ for fixed angles $\alpha = 26°$ and $\alpha = 20°$, respectively.

2.14 (a) and (b) have been chosen to be larger than they actually are in Fig. 2.14 (c) and (d).

The vector magnet allows for magnetic field scans for any angle φ in a 2D space. The additional rotation of the dilution refrigerator insert allows access to any field direction in 3D space. This rotation angle of the insert is marked as α in Fig. 2.14 (a) and (b).

After the experimental setup containing the sample was inserted into the vector magnet setup, angle φ scans were performed at angles of the dilution insert $\alpha = 0°$ and $\alpha = 90°$. For these two angles α, the rotation planes of the vector magnet were approximately perpendicular to each of the two easy axes of the orthorhombic system, $\langle 001 \rangle$ and $\langle 100 \rangle$. In these scans, symmetry axes can be used to identify the angles φ, for which the magnetic field is exactly perpendicular to one of the easy axis. These scans are presented in Fig. 2.14 (c) and (d).

The angles φ of high symmetry found in the two scans in Fig. 2.14 (c) and (d) can then be used to estimate the angle α for the rotation of the DR insert. In particular, the angle α must be determined such that the hard axis of the system is parallel to the 2D rotation plane of the vector magnet. The φ-scan at an estimated angle of $\alpha = 26°$ is shown in Fig. 2.15 (c). In this scan, a superposition of two symmetry elements can be seen. Two maxima at magnetic fields of 5 T are observed at angles of -3.4° and -1.9° symmetrically around an angle of $\varphi_{(100)} \approx$-2.7° (cyan line) are observed. Additionally, signals are observed between magnetic fields of 3 T and 4 T symmetric around an angle of $\varphi_{(001)} \approx$-2.3°. This can be interpreted as there is no angle φ for $\alpha = 26°$, for which the magnetic field is perpendicular to both easy directions $\langle 001 \rangle$ and $\langle 100 \rangle$ simultaneously. By slightly changing the angle α, a perfectly symmetric scan can be found, as shown in Fig. 2.15 (d) for an angle $\alpha = 20°$. From this scan, an angle $\varphi = -2.68°$ was obtained, where the magnetic field is perpendicular to the easy directions $\langle 001 \rangle$ and $\langle 100 \rangle$ and thus parallel to the hard magnetic direction $\langle 010 \rangle$.

For the intentionally canted orientation, the high symmetry angle from Fig 2.14 (c) with $\alpha = 0°$ and $\varphi = -2.58°$ was used. In this orientation, the magnetic field is parallel to the blue (100) plane and perpendicular to the $\langle 100 \rangle$ direction. The angle between this orientation and the b-axis is approximately 0.9°.

Additionally it can be deduced from these scans, in particular from the scan at $\alpha = 20°$ in Fig. 2.15 (d), that the measured susceptibility increases (red areas in the 2D plots) as one tilts away from higher symmetry directions, before it decreases as the tilting angle is further increased.

3 Magnetic Soliton Lattice in $TbFeO_3$ under Transverse Magnetic Fields

The investigation of the magnetic and meta-magnetic phase transitions and their underlying mechanisms in $TbFeO_3$ represents a topic of research in the field of quantum magnetism for over six decades [30, 50–55]. Recently, a magnetic soliton lattice, a non-linear magnetic texture, was observed in a neutron diffraction experiment when a magnetic field was applied perpendicular to both of the Ising axes of the terbium spins [15]. The study proposes, that the magnetic soliton lattice is a result of dynamically stabilizing mechanisms. However, the proposed theory of a repulsive interaction between domain walls in the terbium sublattice, mediated by magnons of the iron sublattice, still lacks further experimental evidence. In particular, the measurement of additional thermodynamic quantities and neutron diffraction experiments may provide useful information for a better understanding of the nature of the magnetic soliton lattice. Open questions focus on the extent of the soliton phase pocket and the working principle of its stabilizing dynamics.

Single crystals of the rare-earth orthoferrite $TbFeO_3$ were grown using the optical floating-zone technique. The low-temperature properties, in particular the different magnetic phases and spin re-orientations under magnetic fields applied along the crystallographic c-axis of the orthorhombic system, were investigated. Of particular interest was the incommensurate soliton lattice phase.

The first part of this chapter provides an overview of the state of the art. The second part of this chapter presents a magnetic phase diagram for magnetic fields up to 12 Tesla parallel to the hard magnetic $\langle 001 \rangle$ direction. This phase diagram is drawn based on experimental results of measurements of the transverse susceptibility and of neutron diffraction experiments presented in the third part. The section ends with a concluding discussion.

3.1 Spin Re-orientation Transitions and Complex Spin Texture in $TbFeO_3$

$TbFeO_3$ crystallizes in the orthorombic $Pbnm$ structure and is a member of the orthorombically distorted perovskite materials. The lattice constants of the conventional unit cell are $a = 5.326\,\text{Å}$, $b = 5.602\,\text{Å}$ and $c = 7.623\,\text{Å}$[39, 41, 56–61]. Fig. 3.1 (a) depicts the crystal unit cell of $TbFeO_3$. The unit cell contains four terbium atoms (red), four iron atoms (blue) and 12 oxygen atoms (gray). The magnetism in this compound is driven by two magnetic subsystems, the iron and the terbium subsystem, which interact with each other. A main subject of early theoretical and experimental studies on $TbFeO_3$

was the investigation of the different spin re-orientation transitions that occur at varying temperatures and magnetic fields, which induce different magnetic orderings in the two magnetic subsystems.

One of the first studies to employ neutron diffraction, measurement of the magnetization and Mössbauer experiments focused on the different spin configurations in zero magnetic field [56]. Coming from high temperatures, the first magnetic transition is observed at a temperature $T_{\mathrm{N,Fe}}$ between 650 K and 691 K, with notable variations observed across different samples [15, 41, 53, 57, 62–64]. Above $T_{\mathrm{N,Fe}}$, the terbium and the iron subsystems are in a paramagnetic state. Below the temperature $T_{\mathrm{N,Fe}}$, the iron spins order antiferromagnetically with small ferromagnetic canting towards the $\langle 001 \rangle$ direction, while the terbium moments remain in a paramagnetic state. The anisotropy of the iron spins is induced by the Dzyaloshinkii-Moriya exchange, the magnetic dipole interaction and the single-ion anisotropy [65]. The spin configuration of the iron atoms is illustrated in the left column of Fig. 3.1 (c). The crystal field splitting of the 4f electrons in $TbFeO_3$ consists of two energy levels separated by 1 K, while being well separated from the remaining energy levels ($\delta \approx 120$ K). The energy level scheme is sketched in Fig. 3.1 (b). This energy level configuration gives rise to Van-Vleck paramagnetism and an Ising-like anisotropy of the g-factor of the terbium spins with two Ising axes in the ab-plane at an angle of approximately $\pm 36°$ from the a-axis [66, 67].

At the temperature $T_{\mathrm{Tb\text{-}Fe}}$ the interaction between the two magnetic sublattices induces a spin re-orientation of both magnetic subsystems. In the literature, various values have been reported for the transition temperature $T_{\mathrm{Tb\text{-}Fe}}$: 8.5 K [15, 41], 8.4 K [56], 7 K [68, 69], 6.5 K [30], [52] and 6 K [53]. Bidaux et al. attempted to explain the variations of ordering temperatures observed across different samples, postulating that shape effects may play a role [50, 70]. In the intermediate phase (IT) below $T_{\mathrm{Tb\text{-}Fe}}$ both magnetic sublattices have a ferromagnetic component parallel to the a-axis, resulting from the Heisenberg interaction between terbium and iron spins [60]. Furthermore, the iron spins exhibit antiferromagnetic behavior along the c-axis, whereas the terbium spins show antiferromagnetic ordering parallel to the b-axis. The spin configurations of the two sublattices in the IT-phase are sketched in the middle column in Fig. 3.1 (c). This spin re-orientation is described as a consequence of the competition between anisotropy and degeneracy lifting, which is analogous to the competition between deformation and degeneracy lifting observed in the Jahn-Teller effect [30, 71]. A study employing Mössbauer spectroscopy came to a similar conclusion regarding the transitions resulting from a competition between Zeemann energy and anisotropy in the iron sublattice [53].

The last spin re-orientation is observed at a temperature $T_{\mathrm{N,Tb}}$ between 3 K and 4 K [15,

30, 41, 52, 53, 68, 69, 72–74]. Below $T_{\mathrm{N,Tb}}$, the antiferromagnetic interaction between the terbium spins becomes dominant resulting in a purely antiferromagnetic ordering of the terbium spins. Consequently, the iron spins return to their high-temperature spin configuration due to the absence of Heisenberg exchange between the two sublattices. The right column in Fig. 3.1 (c) shows the spin configuration of the two magnetic sublattices in this low-temperature phase (LT). Nonmagnetic doping with aluminum has been observed to suppress the antiferromagnetic ordering temperature [75, 76].

The investigation of metamagnetic phase transitions for magnetic fields applied along the major crystallographic axes was of central interest in studies of $TbFeO_3$. For a magnetic field parallel to the a-axis, a spin-flip transition resulting in a field polarized state was observed at a magnetic field of 0.2 T [40, 41, 50–52, 68, 77–79]. Based on experimental results, magnetic phase diagrams were presented for a magnetic field parallel to the a-axis [50, 52, 77].

The two-step metamagnetic behavior for a magnetic field parallel to the b-axis was investigated both, experimentally and theoretically [41, 50, 51, 68, 79, 80]. This process, which consists of two subsequent spin flips, is believed to be influenced by magnetic Jahn-Teller-like effects. It was shown, that it is energetically advantageous to flip the terbium spins one after the other [51]. Above $T_{\mathrm{Tb\text{-}Fe}}$, only the Van-Vleck paramagnetism of the terbium spins contributes to the magnetization along the b-axis, due to the fact that the iron spins are locked in the ac-plane as a result of their anisotropy [40, 41, 67, 68]. This allowed for the extraction of crystal field splitting parameters and the g-factor anisotropy from the b-axis magnetization [67, 68]. No phase diagram for a magnetic field parallel to the b-axis was found in the literature. A recent study has focused on the magnetic phase transitions for magnetic fields at different angles in the ab-plane at 1.9 K and presents the measured electric polarization resulting from the magnetoelectric coupling together with a theoretical model [81].

A magnetic field applied parallel to the c-axis was observed to suppress the intermediate state, in which the two sublattices are coupled to each other [15, 52, 68, 79]. However, a more recent study has revealed the emergence of an incommensurate phase in the vicinity of $T_{\mathrm{N,Tb}}$ when a magnetic field is applied parallel to the c-axis [15]. This incommensurate phase is identified as soliton lattice phase characterized by a periodic alignment of antiferromagnetic domains with alternating directions of the ordering vector. The periodicity was determined to be 340 Å along the b-direction. This periodic alignment results in a considerable number of higher harmonic reflections in a neutron diffraction experiment. This formation of periodically aligned antiferromagnetic domains can be explained by the interplay of the Ising-like anisotropy of the terbium spins and a term in the free energy

allowing a modulation of the spins along the *b*-axis. Following the model proposed in Ref. [15], the interaction separating the domain walls is Coulomb-like and mediated by virtual magnons of the iron sublattice.

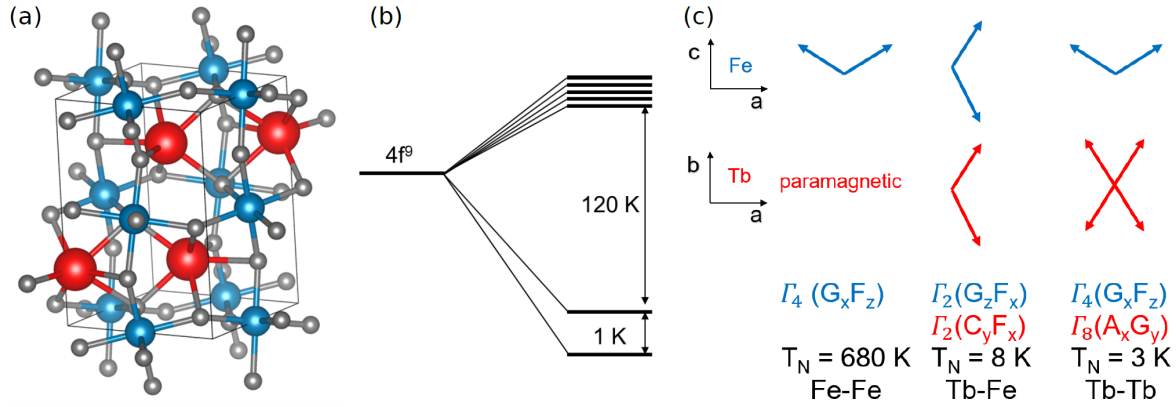

Figure 3.1: (a) Crystal structure of $TbFeO_3$. Terbium atoms are shown in red, iron atoms in blue and oxygen atoms in grey. (b) Schematic crystal electric field splitting of the 4f electrons in $TbFeO_3$ with two energy levels well separated from the remaining levels. (c) Spin configurations of the two sublattices below the different ordering temperatures. Figure taken from Ref. [39].

Futher studies on $TbFeO_3$ focused on a number of additional aspects. Exchange parameters and electric field levels were extracted from magnon dispersions, which were measured by means of inelastic neutron diffraction [57, 58, 60]. The investigation of electromagnons in $TbFeO_3$ was conducted by Stanislavchuk et al. using IR-spectroscopy at temperatures as low as 1.5 K and magnetic fields reaching 9 T applied parallel to all three orthorhombic directions [59]. Tejada et al. investigated the magnetization relaxation in $TbFeO_3$ and observed quantum tunneling of antiferromagnetic domain walls [82]. Krotenko et al. conducted calculations on the relaxation of the magnetization and ruled out self-heating effects to be responsible for the experimental observations [83]. Raman scattering was employed to determine the FeO_6 octahedron tilt angle of various rare-earth ferrites, including $TbFeO_3$ [84]. The influence of magnetic and non-magnetic doping in $TbFeO_3$ has been the subject of numerous studies [75, 76, 85–97].

3.2 Transverse-Field Phase Diagram

The first magnetic phase diagram including the soliton lattice phase for a magnetic field parallel to the hard axis of $TbFeO_3$ was presented in Ref. [15]. Fig. 3.2 shows this phase diagram adapted from Artuykhin et al. This first phase diagram was inferred from neutron diffraction and capacitance and loss measurements for magnetic fields up to 4 T.

In this published phase diagram, the spin reorientation transition between the HT and the IT phase was observed at a temperature of 8.5 T and between the IT and the LT phase at a temperature of 3 K in zero magnetic field. The soliton lattice phase (IC) was observed for magnetic fields above 1 T in the vicinity of 3.3 K. At a temperatures below 3 K, a transition from a LT phase to a LT' phase was observed for magnetic fields of ≈ 0.5 T. This LT' prime was explained by domain-wall pinning weakening the magnon-mediated interaction between the domain walls [15]. The resulting correlation function of the order parameter of the randomly positioned domain walls decays exponentially with distance.

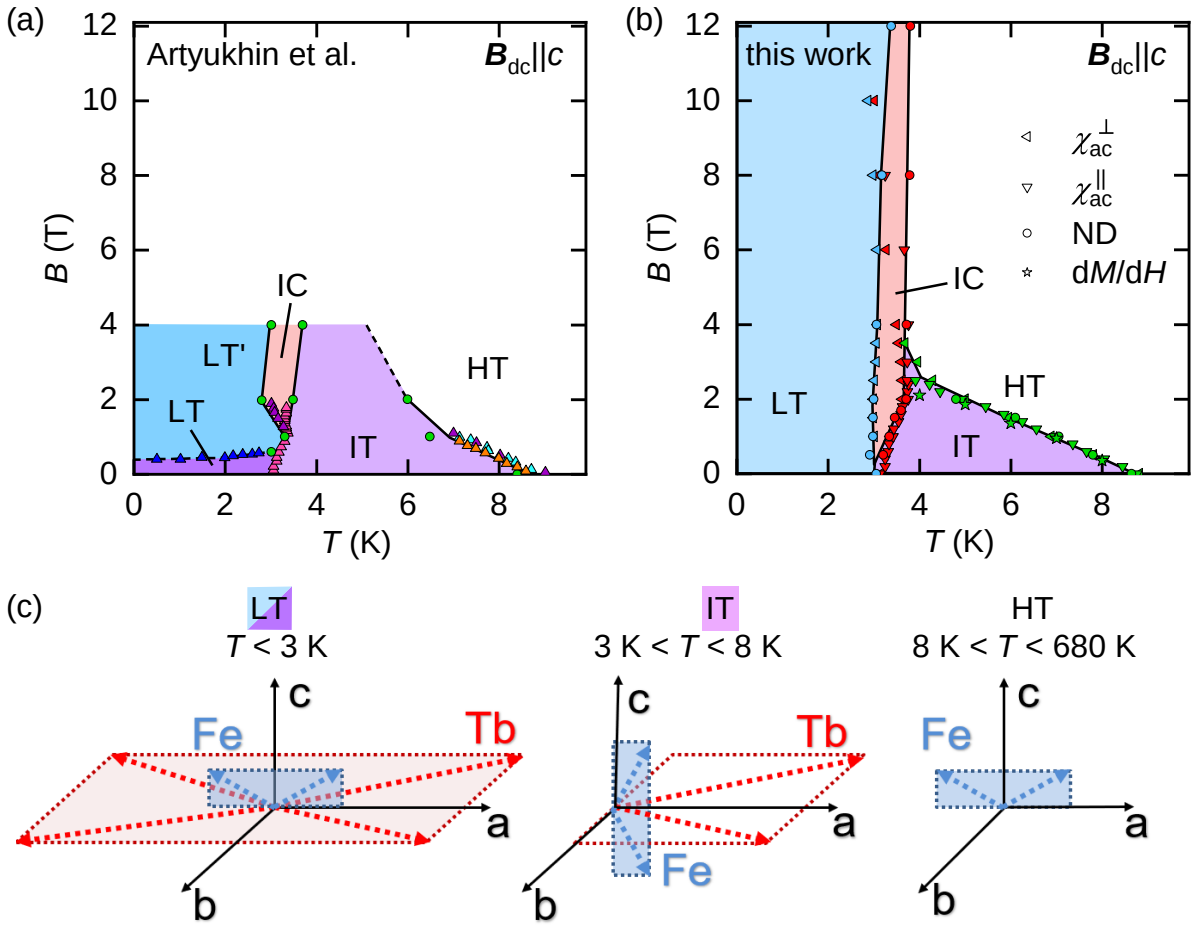

Figure 3.2: (a) Hard-axis magnetic phase diagram adapted from Ref. [15]. (b) Hard-axis magnetic phase diagram of $TbFeO_3$ extracted from magnetometry and neutron diffraction measurements in this work. (c) Visualizations of the spin configurations of the iron and the terbium sublattices in the different magnetic phases in zero magnetic field.

Fig. 3.2 (b) depicts our hard-axis magnetic phase diagram for temperatures between 0 K and 10 K and for magnetic fields up to 12 T. The data points were extracted from our neutron diffraction and magnetometry experiments. At zero magnetic field, three phases

are observed: the high-temperature phase (HT), the intermediate phase (IT) and the low-temperature phase (LT). The HT phase is characterized by ordered iron moments and paramagnetic terbium moments and is observed between $T_{N1} = 8.7\,\mathrm{K}$ and $T_{N0} \approx 680\,\mathrm{K}$. Between $T_{N1} = 8.7\,\mathrm{K}$ and $T_{N2} = 3.1\,\mathrm{K}$, the exchange interaction between the iron and the terbium moments induces a magnetic ordering with re-orientated spin configurations of the two magnetic sublattices with ferromagnetic components parallel to the $\langle 100 \rangle$ direction. Below a temperature of $T_{N2} = 3.1\,\mathrm{K}$, the system undergoes another spin re-orientation transition, resulting in a purely antiferromagnetic ordering of the terbium spins, while the iron spins return to the same spin configuration as in the HT phase. Fig. 3.2 (c) visualizes the spin configurations of the two magnetic sublattices in the three zero-field phases.

As the magnetic field parallel to the $\langle 001 \rangle$ direction increases, T_{N2} increases continuously while T_{N1} decreases, resulting in a narrowing of the temperature regime of the IT phase. Above a magnetic field of 4 T, the IT phase was not observed in our measurements. While the temperature region of the IT phase disappears with increasing magnetic field, an incommensurate phase (IC) emerges between T_{N2} and T_{N3}. This incommensurate phase is characterized by a periodic alignment of antiferromagnetic domains of the terbium spins with a ferromagnetic coupling at the domain walls. However, no indications of an additional low-temperature phase LT' were found in our measurements.

In the field range between 0 T and 2 T, the temperature band of the IC phase broadens with increasing magnetic field. Above 2 T, the transition temperatures T_{N2} and T_{N3} exhibit only weak field dependence. For magnetic fields above 3 T, the transition temperatures T_{N2} and T_{N3} inferred from susceptibility measurements and from neutron diffraction experiments start to deviate. The discrepancy may be attributed to the intentional misalignment angle of 3.5° between the hard axis of the sample and the magnetic field applied during the transverse susceptibility measurement. Further details on the misalignment can be found in section 3.3.

The following sections present the transverse susceptibility data and the results of the elastic neutron diffraction experiment.

3.3 Transverse Susceptibility

A susceptometer is commonly used to probe the susceptibility parallel to a static magnetic field. This configuration is suitable for many scientific questions. However, in the following is shown, that as the magnetic anisotropy increases, the choice of an alternative probing direction becomes increasingly relevant.

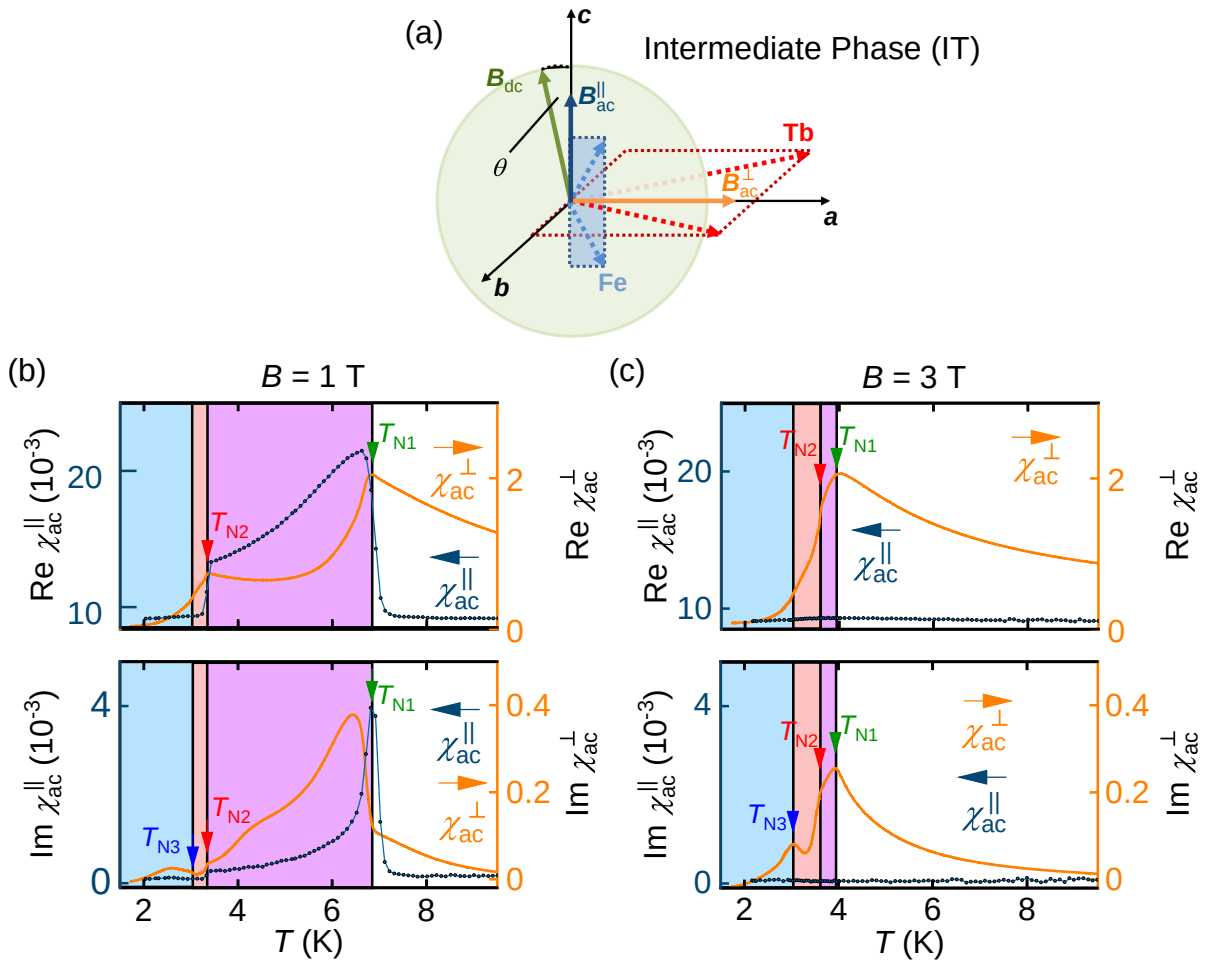

Figure 3.3: Comparison of the longitudinal and the transverse susceptibility of $TbFeO_3$ for different magnetic fields applied parallel to the ⟨001⟩ direction. (a) Visualization of the directions of the static field and the excitation fields with respect to the spin configurations of the terbium and iron sublattice in the intermediate phase. (b) and (c) Comparison of the longitudinal susceptibility (blue) and the transverse susceptibility (orange) at magnetic fields of 1 T and 3 T, respectively. The different color shadings in the background of the plots mark the regions of different magnetic phases.

Fig. 3.3 (a) shows schematically the direction of the applied magnetic fields for the transverse and longitudinal susceptibility configuration in the context of the spin directions in the IT phase. The terbium spins are fixed in the *ab*-plane and the iron spins are fixed in the *ac*-plane. In the longitudinal configuration, the excitation field $B_{\mathrm{ac}}^{\parallel}$ is parallel to the static magnetic field B_{dc} and the *c*-axis of the crystal. For the transverse configuration, the excitation field $B_{\mathrm{ac}}^{\perp}$ is parallel to the *a*-axis while the static magnetic field is applied long the *c*-axis perpendicular to the excitation field. The angle θ between the static magnetic field B_{dc} and the *c*-axis was introduced for the study of an intentional misalignment of the magnetic field. The transverse susceptibility data of $TbFeO_3$ presented in Fig 3.3

and Fig. 3.5 were recorded using a misalignment angle of 3.5°.

Fig. 3.3 presents a comparison of the measured temperature dependence of the susceptibility signal for a longitudinal and a transverse susceptibility measurements. The static magnetic field is applied predominantly parallel to the hard magnetic ⟨001⟩ direction of the sample. For the measurement of the longitudinal susceptibility, the ac magnetic excitation field was applied parallel to the static magnetic field along the ⟨001⟩ direction. In contrast, for the measurement of the transverse susceptibility, the ac magnetic excitation field was applied parallel to the ⟨100⟩ direction, perpendicular to the static magnetic field. Fig. 3.3 (b) presents the real and imaginary parts of the longitudinal and transverse signal for a static magnetic field of 1 T. Prominent signatures characteristic of T_{N1} and T_{N2} are evident in all signal curves. However, a minor shoulder marking the transition temperature T_{N3} is only discernible in the imaginary part of the transverse susceptibility.

Fig. 3.3 (c) depicts the same measurement quantities, but for a magnetic field of 3 T. The real and imaginary parts of the longitudinal susceptibility are at a constant low level and lack any discernible signature. In both, the real and imaginary parts of the transverse susceptibility, a global maximum at a temperature of $T_{N1} = 3.94\,\mathrm{K}$ marks the transition between the HT and the IT phases, while a kink at $T_{N2} = 3.6\,\mathrm{K}$ is characteristic of the transition between the IT phase and the IC phases. A distinct maximum at $T_{N3} = 3.04\,\mathrm{K}$, observed exclusively in the imaginary part of the transverse susceptibility in Fig. 3.3 (c) marks the transition between the IC phase and the LT phase.

This comparison demonstrates that the measurement of the transverse susceptibility is more effective than the longitudinal susceptibility for the mapping of the hard-axis magnetic phase diagram. In this hard-axis configuration, the longitudinal susceptibility is most likely only sensitive to the iron sublattice. This results from the strong anisotropy of the terbium spins, which are fixed in a plane perpendicular to the ⟨001⟩ direction [66, 67].

Fig. 3.4 presents the effect of an intentional misalignment on the measured transverse susceptibility signal. The rotation axis was approximately parallel to the ⟨010⟩ direction. In Fig. 3.4 (a) the temperature dependence of the imaginary part of the transverse susceptibility for a magnetic field of 1.5 T is plotted for a selection of different misalignment angles. The maximum at the temperature T_{N3} becomes particularly pronounced at a misalignment angle of 3.5°. This angle was chosen for investigation of the transverse susceptibility of $TbFeO_3$. Fig. 3.4 (b) illustrates the angle dependence of the maximum signal of the imaginary part of the transverse susceptibility marked in Fig. 3.4 (a). The angle dependence of the maximum signal was used to determine the misalignment angle

for the measurement of the temperature dependence of the transverse susceptibility of $TbFeO_3$. The maximum of a parabola fit marks the minimum misalignment angle.

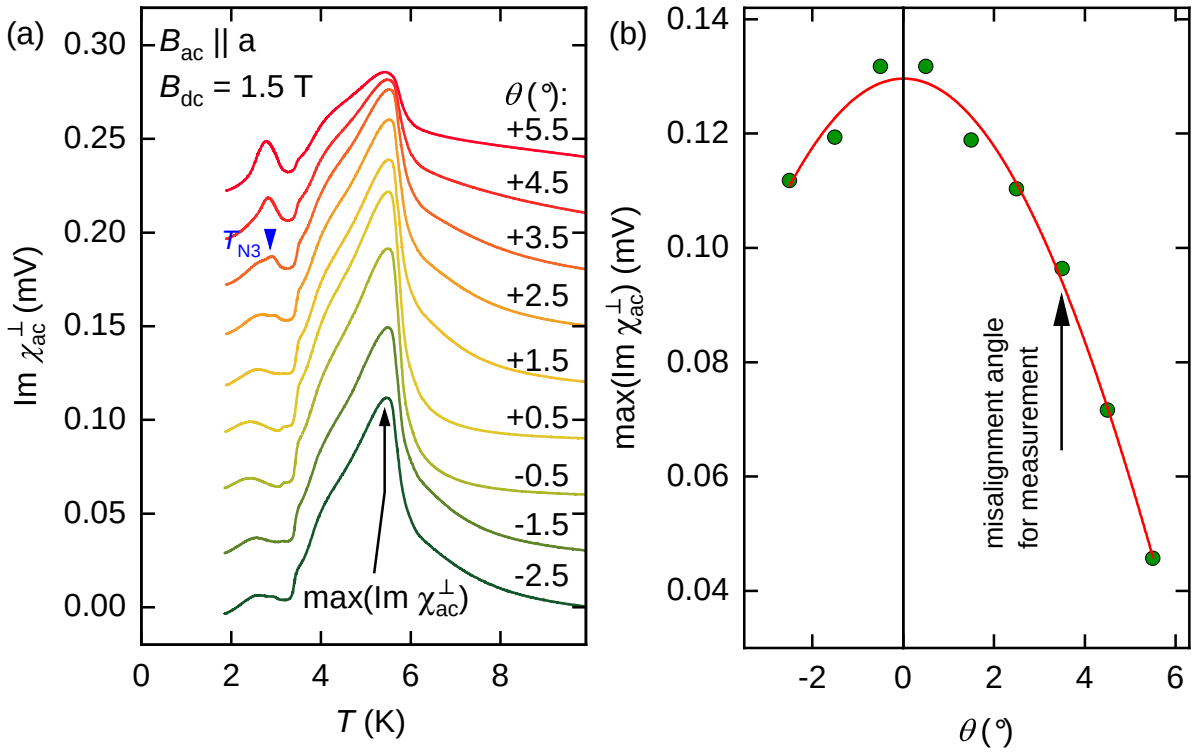

Figure 3.4: Temperature dependence of the transverse susceptibility of $TbFeO_3$ at a constant magnetic field of 1.5 T for a selection of different misalignment angles away from the ⟨001⟩ direction. (a) Imaginary part of the transverse susceptibility plotted with constant offsets. (b) Angle dependence of the maximum signal of the imaginary part of the transverse susceptibility.

Fig. 3.5 shows the temperature dependence of the real and the imaginary parts of the transverse susceptibility for a selection of constant magnetic fields that are predominantly parallel to the ⟨001⟩ direction.

In Fig. 3.5 (a), the temperature dependence of the real part of the transverse susceptibility is presented. At zero magnetic field, a global maximum at $T_{N1} = 8.68\,\mathrm{K}$ marks the transition between the HT and the IT phases. As the magnetic field increases, this maximum shifts to lower temperatures. A small maximum at $T_{N2} = 3.12\,\mathrm{K}$ is characteristic of the transition between the IT and the LT phases. T_{N2} increases slightly when a magnetic field is applied. However, above magnetic fields of 1.5 T, the maximum at T_{N2} in the real part of the transverse susceptibility can no longer be tracked.

Fig. 3.5 (b) illustrates the temperature dependence of the imaginary part of the transverse susceptibility. A kink at T_{N1} marks the transition between the HT and the IT phases. As the magnetic field increases, this kink shifts to lower temperatures, becoming a maximum

for magnetic fields larger than 2 T. For magnetic fields larger than 6 T, this maximum at T_{N1} in the imaginary part of the transverse susceptibility is no longer discernible. In the absence of a magnetic field, a shoulder in the imaginary part at $T_{N2} = 3.12$ K indicates the transition between the IT and the LT phases. With increasing magnetic field, the shoulder at T_{N2} shifts to slightly higher temperatures. At a magnetic field of 3.5 T, the shoulder at T_{N2} becomes a maximum. As the magnetic field is further increased, T_{N2} decreases slightly.

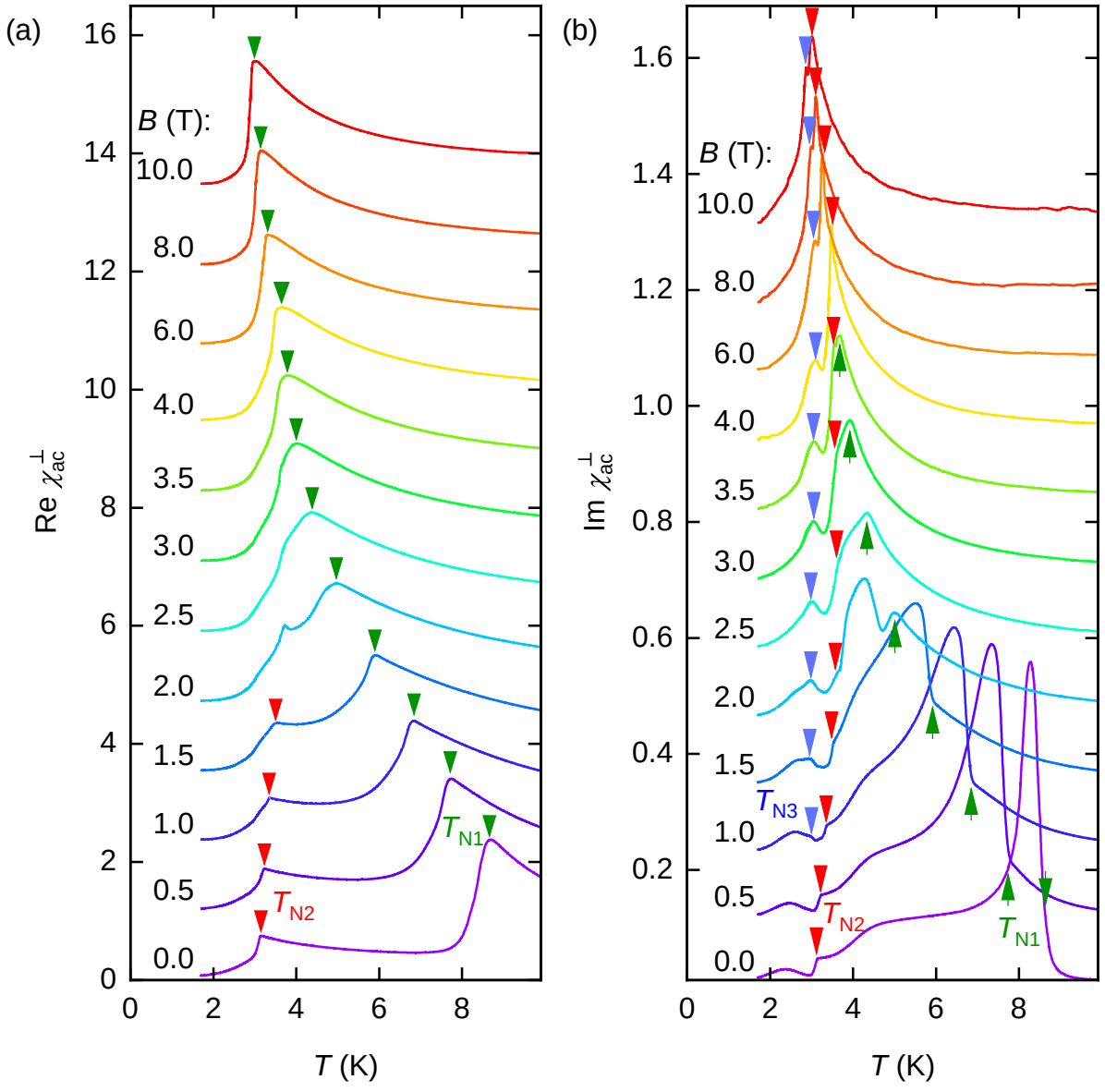

Figure 3.5: Temperature dependence of the transverse susceptibility of $TbFeO_3$ for a selection of constant magnetic fields parallel to the ⟨001⟩ direction. The data is plotted with constant offsets. (a) Real part of the transverse susceptibility. (b) Imaginary part of the transverse susceptibility.

At a magnetic field of 1 T, a small shoulder emerges at $T_{N2} = 2.99$ K in the imaginary part of the transverse susceptibility. As the magnetic field is further increased, this shoulder becomes a maximum and remains at a constant temperature up to a magnetic field of 6 T. For even larger magnetic fields, T_{N2} decreases slightly. The discrepancies between the temperatures T_{N3} obtained from neutron diffraction and transverse susceptibility measurements may be a result of the intentional misalignment angle in the susceptibility measurement. An overview of all signatures observed in the transverse susceptibility in Fig. 3.5 is presented in table 1.

Transition temperature	Signature	Color
T_{N1}	local maximum in $\mathrm{Re}(\chi_{ac}^{\perp})$ and a kink turning in a maximum in $\mathrm{Im}(\chi_{ac}^{\perp})$	green
T_{N2}	kink which turns into a maximum in $\mathrm{Re}(\chi_{ac}^{\perp})$ and a kink in $\mathrm{Im}(\chi_{ac}^{\perp})$	red
T_{N3}	maximum in $\mathrm{Im}(\chi_{ac}^{\perp})$	blue

Table 1: Overview of the signatures attributed to different phase transitions in the temperature dependence of the transverse susceptibility for transverse field orientation in $TbFeO_3$ in Fig. 3.5.

3.4 Elastic Neutron Diffraction

The first evidence for solitonic spin textures in $TbFeO_3$ was provided by the emergence of higher harmonic peaks in elastic neutron diffraction measurements [15]. In this work, neutron diffraction methods were similarly used to study the extent of the incommensurate phase and to prepare for the study of potential dynamics of stabilizing mechanisms behind the solitonic spin texture using inelastic neutron scattering techniques.

Fig. 3.6 (a) shows the $TbFeO_3$ sample in the aluminum housing prepared to prevent the sample from moving due to magnetic torque induced by the transverse magnetic field. As shown in Fig. 3.6 (b) the aluminum housing was mounted to a sample stick of the flow cryostat used at the triple-axis spectroscopy neutron beam line PANDA. The sample was orientated such that the magnetic field is parallel to the *c*-axis and the *ab*-plane is the scattering plane of the experiment. The neutron beam line PANDA at the Heinz Maier-Leibnitz Zentrum (MLZ) in Garching is shown in Fig. 3.6 (c).

Fig. 3.7 (a) and (b) illustrate the measured neutron intensity as a function of the scattering vector at a temperature of 3.1 K and magnetic fields of 12 T and 4 T, respectively. For this subtraction, the measured diffraction patters at 8.5 K for both magnetic fields were used. The higher harmonic peaks up to the seventh order, which are characteristic of the soliton lattice as described in the literature, are clearly visible for both magnetic fields.

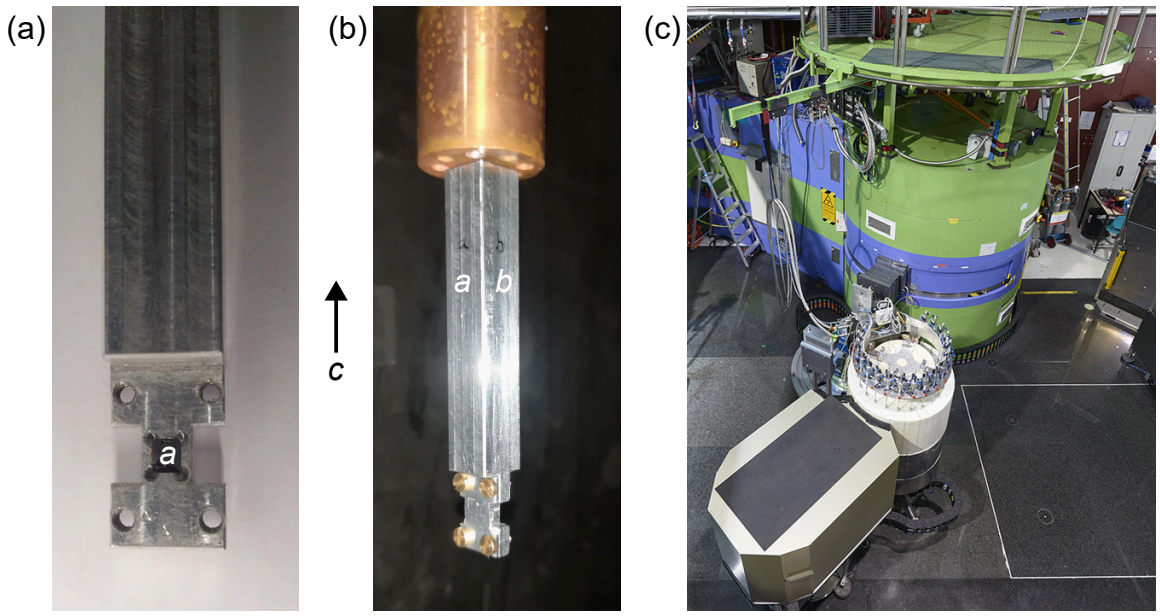

Figure 3.6: Experimental setup for the neutron diffraction experiment at the triple-axis spectrometer PANDA at the Maier-Leibnitz Zentrum in Garching. (a) Sample inside the custom-fit aluminum sample holder. The a-axis of the sample is in out-of-plane direction. The c-direction of the sample points upwards. (b) The sample holder with lid attached to the lower end of the cryogenic sample stick. The a and b direction are as shown in horizontal direction. (c) The cold triple-axis spectrometer PANDA at the Heinz Maier-Leibnitz Zentrum in Garching. Image taken from Ref. [98].

In contrast to the higher harmonic peaks observed by Artyukhin et al. [15], the peaks measured in this study are broader and have a lower intensity. These discrepancies may result from a different sample quality. However, qualitatively, the diffraction patterns resulting from the soliton lattice structure observed in our study are consistent with Ref. [15].

Fig. 3.7 (c) shows the magnetic field dependence of the intensity measured at a temperature of 3.1 T at the position of the third harmonic peak (1,-1.058,0). The emergence of the soliton lattice is marked by a sharp increase in the measured intensity between 1.6 T and 2 T. The intensity remains elevated up to the maximum magnetic field of 12 T.

Fig. 3.8 presents the measured neutron intensity as a function of the k-vector and the temperature for a selection of different magnetic fields between 0 T and 12 T. For all panels the structural background at a temperature of 10.5 K in zero field and at 8.5 K for all finite magnetic fields was subtracted. In Fig. 3.8 (a), the measured intensity in zero magnetic field is shown. The onset of intensity is observed below temperatures of $T_{N1} = 8.65\,\mathrm{K}$ at the (1,-1,0) position. This intensity remains at a constant level down to $T_{N2} = 3.00\,\mathrm{K}$. At zero magnetic field, T_{N2} is characterized by the beginning of a broadening of the observed

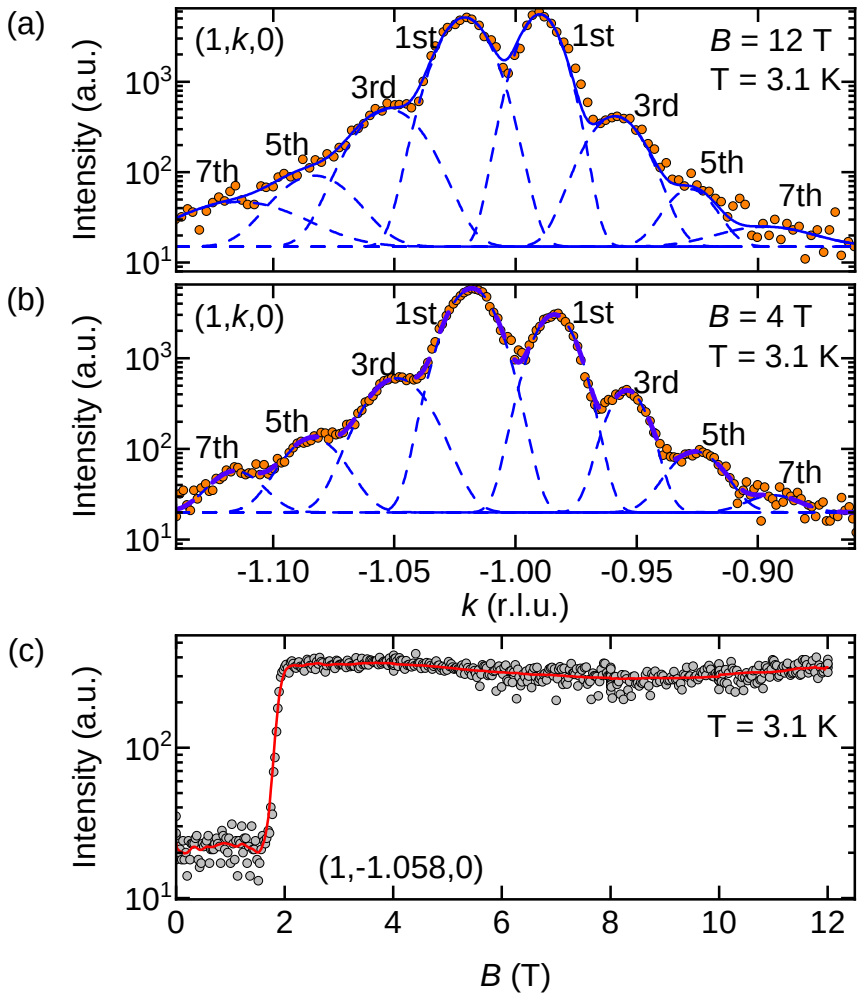

Figure 3.7: (a) and (b) Neutron diffraction pattern of $TbFeO_3$ at 3.1 K for magnetic fields of 12 Tesla and 4 Tesla, respectively, applied parallel to the $\langle 001 \rangle$ direction. The nuclear contribution was subtracted using the diffraction patterns recorded at 8.5 K at the respective magnetic fields. Gaussian fits and their superposition are added in order to pronounce the nature of the satellite peak contributions to the diffraction patterns. (c) Magnetic field dependence of the intensity observed at the position of the third harmonic diffraction peak. The red line results from a smooth of the data and serves as a guide to the eye.

intensity towards lower temperatures.

The application of a magnetic field parallel to the $\langle 001 \rangle$ direction results in a shift of the onset of intensity at T_{N1} to lower temperatures as shown in Fig. 3.8 (b)-(e). As illustrated in Fig. 3.8 (f)-(h), the onset of intensity is no longer discernible. This can be interpreted as a disappearance of the IT phase for magnetic fields of 4 T and higher.

In Fig. 3.8 (b), for a magnetic field of 0.5 T, the emergence of higher harmonic peaks can be observed for temperatures between T_{N2} =3.22 K and T_{N3} =2.92 K. As illustrated in

Fig. 3.8 (b)-(e), it is observed that the broadening of the intensity at T_{N2} shifts to slightly higher temperatures with increasing magnetic field up to 2 T and turns into an onset of several peaks, characteristic of the soliton lattice. As the magnetic field is increased up to 8 T, the higher harmonic peaks become more pronounced. The onset temperature of the peaks at T_{N2} shifts only slightly from 3.71 K at 2 T to 3.80 K at 12 T. The transition temperature T_{N3} of the disappearance of the higher harmonic peaks at T_{N3} exhibits only weak magnetic field dependence as well and shifts only slightly to higher temperatures.

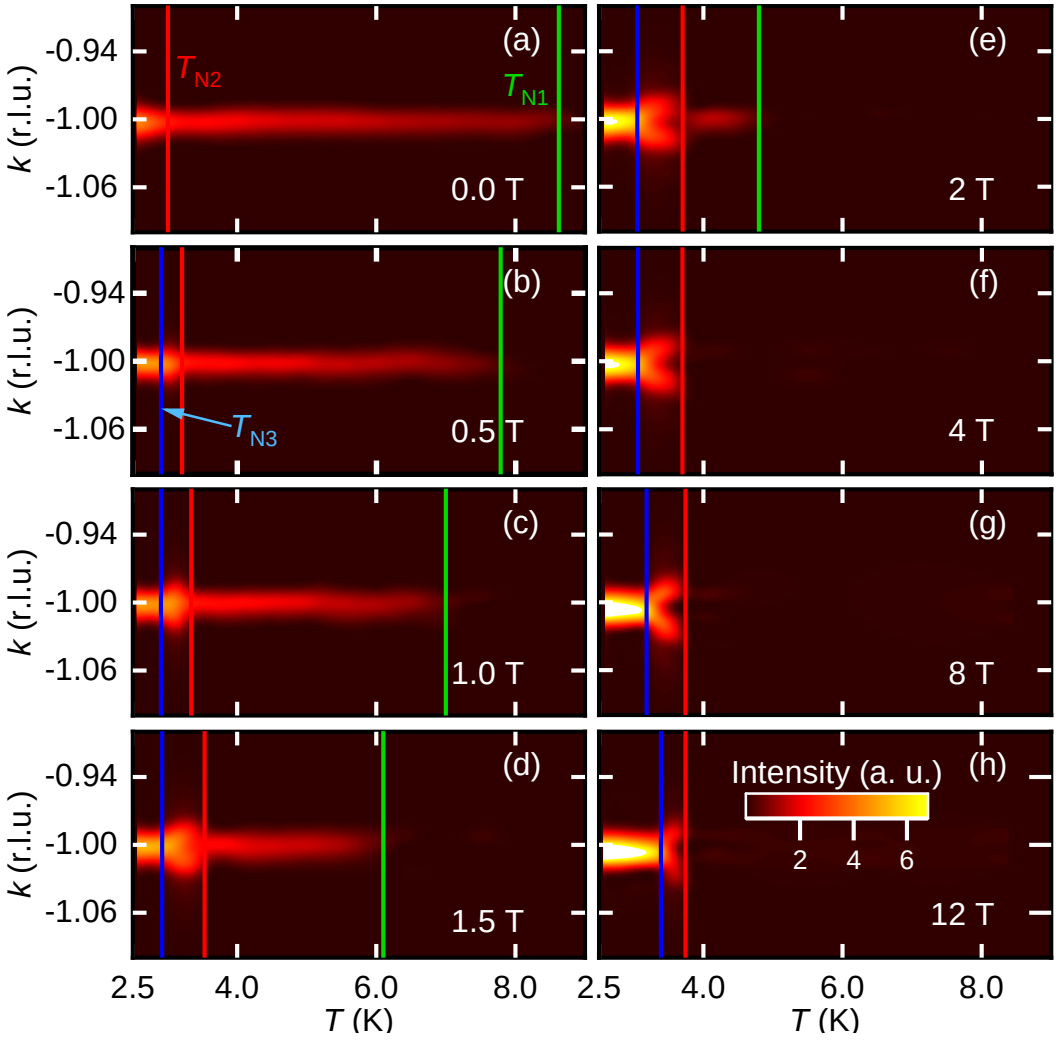

Figure 3.8: Temperature dependence of the neutron diffraction patterns of $TbFeO_3$ for different magnetic fields up to 12 T applied parallel to the ⟨001⟩ direction. The nuclear contribution was subtracted using the diffraction pattern recorded at 10.5 K in zero field in panel (a) and using the diffraction pattern recorded at 8.5 K at the respective magnetic field in panels (b)-(h).

3.5 Hard-Axis Heat Capacity

The measurement of the hard-axis heat capacity of $TbFeO_3$ is highly challenging, primarily due to the significant torque that is generated when a magnetic field is applied parallel to the $\langle 001 \rangle$ direction.

To conduct this measurement, the hard-axis heat capacity setup II was employed and the sample was securely fixed to the sample platform using Stycast covering the entire sample. However, the magnetic torque was sufficiently significant to cause a plastic deformation of the sample platform. Consequently, the extracted data must be treated with caution. For the measurement, large heat pulses were employed because this technique is less time consuming than the conventional thermal relaxation method and is more sensitive to first-order transition as the one at $T_{\mathrm{N2}} \approx 3\,K$ [99]. In contrast to the thermal relaxation method, which aims on heat pulses with a typical temperature rise of 2%, the large pulse method used here aimed on temperature rises of 30%. The recorded heat pulses were evaluated using the dual-slope method provided by the heat capacity software of the Quantum Desing PPMS. This method analyses the time derivative of the temperature variation of the sample during a heat pulse heat pulses to extract the corresponding heat capacity [48, 99].

Fig. 3.9 shows the temperature dependence of the specific heat for a selection of different magnetic fields. The specific heat at zero magnetic field shown here is in agreement with the result of previous measurements using commercially available heat capacity setups and with the literature [39, 100]. A broad maximum at $T_{\mathrm{N1}} = 7.92\,\mathrm{K}$ marks the transition between the HT and the IT phases. The sharp peak observed at $T_{\mathrm{N2}} = 3.06\,\mathrm{K}$ is characteristic for the first-order transition between the IT and the LT phases.

When a magnetic field is applied parallel to the $\langle 001 \rangle$ direction, the maximum at T_{N1} shifts to lower temperatures and the size of the maximum decreases. At a magnetic field of 4 T, the maximum disappears.

The sharp peak at T_{N2} shifts to higher temperatures for magnetic fields up to 2 T. For larger magnetic fields, T_{N2} decreases again. This decrease in temperature of the sharp peak may be a result of the increasing misalignment of the sample due to the magnetic torque bending the sample platform.

At a magnetic field of 1 T, an additional maximum emerges at $T_{\mathrm{N3}} = 3.04\,\mathrm{K}$, marking the transition between the IC and the LT phases. With increasing magnetic field, the maximum shifts to slightly lower temperatures and becomes a shoulder at magnetic fields of 4 T and 6 T.

The temperatures of the signatures at T_{N2} and at T_{N3} shift more strongly towards lower temperatures with increasing magnetic field than observed in the neutron diffraction measurement. It is likely that the strong temperature shifts of the two signatures result from the sample platform bending due to the large magnetic torque acting on the sample in a transverse magnetic field, leading to undesired easy-axis components of the magnetic field.

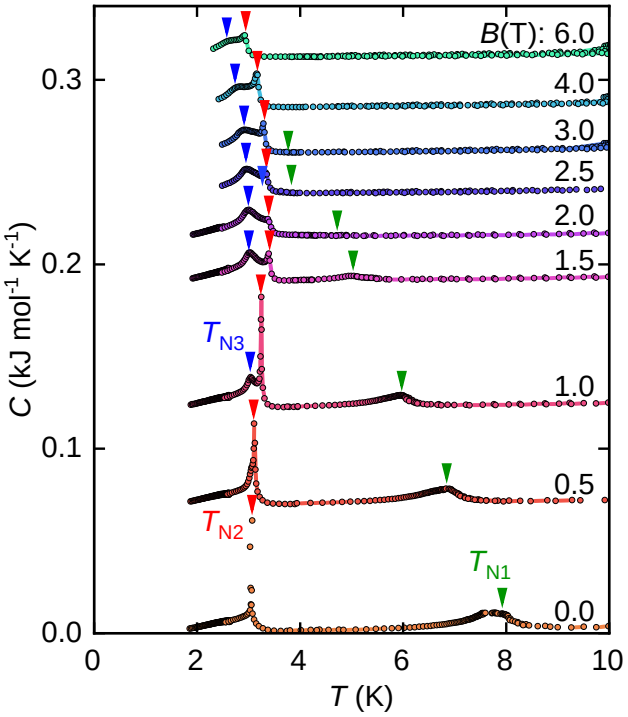

Figure 3.9: Specific heat of $TbFeO_3$ for different magnetic fields between 0 T and 6 T applied dominantly parallel to the ⟨001⟩ direction. The curves are plotted with offsets to avoid an overlap.

3.6 Summary and Outlook

To date, only one study has been published on the soliton lattice phase [15]. Therefore, further investigations into this complex magnetic texture in $TbFeO_3$ are necessary. Our study started with the synthesis of single-crystal $TbFeO_3$. From the synthesized material, cuboid samples were prepared for magnetometry, heat capacity and neutron diffraction experiments.

Our work presents a hard-axis magnetic phase diagram for magnetic fields up to 12 T. The intermediate phase is suppressed by a magnetic field parallel to the c-axis, and the IT phase is not observed above 4 T. Neutron diffraction experiments revealed the presence

of the soliton lattice phase for magnetic fields larger than 0.5 T, with a large number of satellite peaks observed. The satellite peaks remained clearly present at the maximum accessible magnetic field of 12 T.

A comparison of the respective signals showed the advantages of the transverse ac susceptibility over the longitudinal ac susceptibility for studying the magnetic properties of $TbFeO_3$ in a transverse magnetic field. At a magnetic field of 3 T, the transverse ac susceptibility showed distinct signatures in the temperature dependence, while the signal in the longitudinal ac susceptibility has disappeared. This disappearance of the signal is a consequence of the terbium spins not contributing to the c-axis susceptibility.

In the imaginary part of the transverse ac susceptibility a local maximum at a temperature T_{N3} was observed, indicating the low-temperature phase boundary of the soliton lattice phase. The emergence of this maximum required a small longitudinal magnetic field component. The longitudinal magnetic field component was provided by slightly canting the static magnetic field away from the c-axis towards the a-axis.

The heat capacity of $TbFeO_3$ in a transverse magnetic field was measured using a custom-built setup for anisotropic samples. The setup allowed to measure the heat capacity up to a magnetic field of 6 T. The emergence of a maximum at a temperature T_{N3} marks the presence of the soliton lattice phase. The large magnetic torque acting on the sample in a transverse magnetic field leads to an increased bending of the sample platform with increasing magnetic field. The deviations in the transition temperature between heat capacity and neutron diffraction experiments are most likely a result of the bending of the sample platform introducing easy-axis components of the magnetic field.

Future measurements are planned to study the dynamics of the potential stabilizing mechanism of the soliton lattice phase as proposed by Artyukhin et al. [15]. Inelastic neutron diffraction experiments employing a triple-axis spectrometer or a resonant spin-echo spectrometer may shed light on the stabilizing mechanism. In addition, a more rigid heat capacity setup was prepared to measure the hard-axis heat capacity of $TbFeO_3$ under a fixed magnetic field orientation.

4 Quantum Phase Transitions in the 1D-Ising System $CoNb_2O_6$

A phenomenon studied frequently in low-temperature quantum magnetism is the quantum phase transition from an magnetically ordered to a paramagnetic phase in the one-dimensional Ising chain induced by a transverse magnetic field. In literature, the columbite compound $CoNb_2O_6$ is regarded as a prototype realization of a quasi one-dimensional Ising spin chain system. $CoNb_2O_6$ in a transverse magnetic field was the topic of a plethora of recent studies, addressing quantum phase transitions and an emergent E8 symmetry [16, 101–104], different treatment of the inter-chain and intra-chain couplings [18, 105], an unexpected large heat capacity at the transverse-field quantum phase transition [35], and geometric frustration [106, 107]. However, the overall understanding of the physics in this compound still lacks detailed information on the exact shape of the transverse-field phase diagram. Additional intriguing question concern the relationship between the phase diagram and the hierarchy of energy scales of the system and how the quantum criticality influence the observed magnetic properties. We employ measurements of the transverse susceptibility, the heat capacity and the magnetocaloric effect to address these open questions. Most notably we provide a detailed magnetic phase diagram, that permits to study the evolution from the fundamental model of an Ising chain towards a playground for complex magnetism.

The following chapter starts with an overview of the physical background of quantum phase transitions, in particular in the context of Ising spin systems. Subsequently, the results of the growth of single-crystal $CoNb_2O_6$ and of the low-temperature experiments conducted are presented. A magnetic phase diagram under transverse magnetic fields is drawn based on the results obtained from measurements of the transverse susceptibility, the heat capacity and the magnetocaloric effect in a transverse magnetic field down to milli-Kelvin temperatures. Additionally, a magnetic phase diagram is presented for the case of a small misalignment angle between the hard magnetic axis and the magnetic field. Finally, the critical trajectories of the quantum phase transitions are evaluated.

4.1 Quantum Phase Transition

Quantum phase transitions represent a distinct class of phase transitions driven by quantum fluctuations induced by non-thermal parameters. The following description of (quantum) phase transitions is based on Refs. [28, 33, 108–110]. In general, phase transitions are classified as either first-order or second-order phase transition.

First-order phase transitions involve latent heat and allow for the coexistence of two

phases at the transition point. An example of a first-order phase transition is the process of melting ice. In the process of melting ice, a sudden change of the structural order parameter takes place. First-order phase transitions typically exhibit a delta peak-like signal in the specific heat. Second-order phase transitions are characterized by a continuous change of the order parameter and do not involve phase coexistence or latent heat. Examples of second-order phase transitions include the Curie point of ferromagnetic ordering and the superconducting phase transition. At the transition point, continuous phase transitions exhibit a lambda-shaped signal in the specific heat. Aside of these two type of transitions, there is the crossover. Strictly speaking, a crossover is not a phase transition as the order parameter remains finite at all times.

Landau theory is often used to describe the different phase transitions and crossovers. The core of this concept is the Landau free energy, which is a Taylor expansion in an order parameter with only terms allowed by the symmetry of the Hamiltonian [111]. The value of the order parameter is determined by minimizing the Landau free energy. Fig. 4.1 (A1) shows the Landau free energy as a function of an order parameter M. In the case of the disordered phase, there are local minima at finite values of M, but the global minimum is at $M = 0$. The orange curve displays the Landau free energy at the point of the first-order transition. In this case, there are three minima at different values of M, all with the same energy. This allows for the coexistence of the ordered and the disordered phases. For the ordered phase, represented by the blue curve, the minima at $M = 0$ is a local minimum, while the global minima can be found at an order parameter $M \neq 0$. Fig. 4.1 (A2) shows the order parameter as a function of an external parameter g in the case of a first-order transition. At the transition point, the order parameter M jumps discontinuously from zero to a finite value.

The Landau free energy for a second-order phase transition, for instance for an Ising system, can be written as

$$f = f_0 + aM^2 + bM^4 \tag{10}$$

where M is the order parameter and a and b are only dependent on the external parameter, for instance the temperature or magnetic field. b needs to be positive in any case to ensure a global minimum in the free energy while a changes its sign continuously across the second-order phase transition. The evolution of the Landau free energy across a second-order phase transition is shown in Fig. 4.1 (B1). In the disordered phase a is positive and hence the free energy has only one minimum at $M = 0$. This is shown as the green curve in Fig. 4.1 (B1). Towards the critical point, the curve becomes increasingly flatter near $M = 0$. In the ordered phase a becomes negative and two minima emerge at finite M,

illustrated by the blue curve in Fig. 4.1 (B1). In the ordered phase, a becomes negative as the external parameter moves away from the critical point. Therefore, the position of the minima continuously moves away from $M = 0$. The order parameter M as a function of the external parameter g for a second-order transition is shown in Fig. 4.1 (B2). In the disordered region for $g > 1$, the order parameter is zero. Starting from the critical point at $g = 1$, the order parameter M increases continuously as g decreases.

For a crossover, the order parameter always takes finite values. The change of the external parameter g results in a change of the energy landscape as shown in Fig. 4.1 (C1). This results in a change of the position of the minimum of the Landau free energy. The effect of the external parameter g on the order parameter in the case of an crossover is shown in Fig. 4.1 (C2). As the external parameter g decreases, the order parameter M increases continuously.

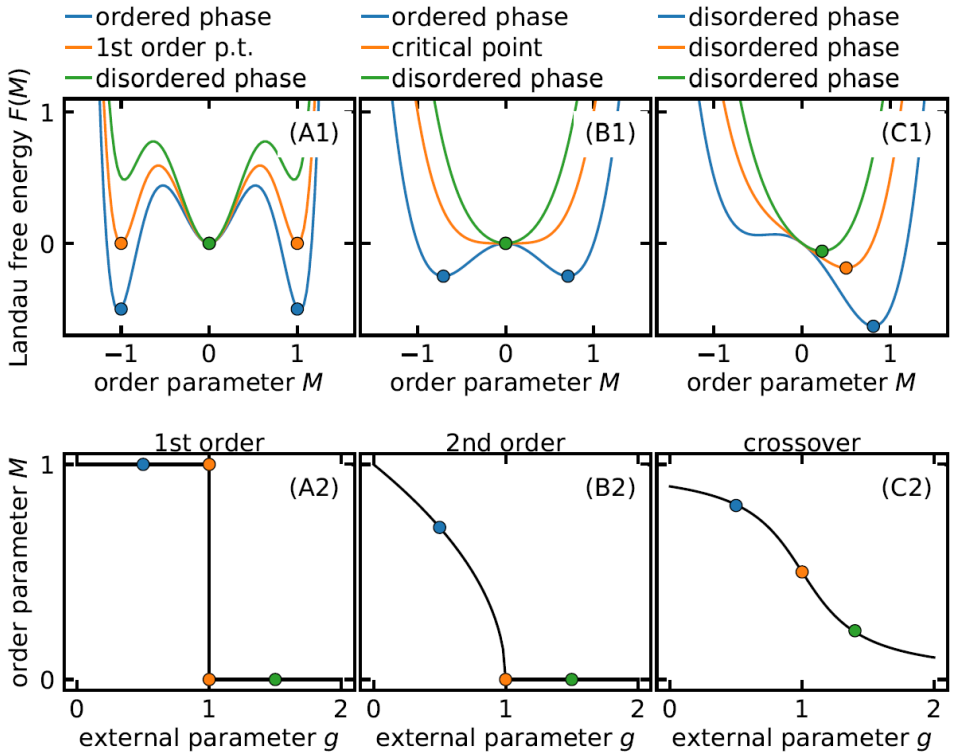

Figure 4.1: Visualization of the energy landscape of the Landau free energy and the order parameters of phase transitions in the context of Landau Theory. (A), (B) and (C) show the case of a first-order and second-order transition and of a crossover, respectively. Figure taken from Ref. [33].

Unlike ordinary temperature-induced phase transitions, quantum phase transitions are not driven by the suppression of an order parameter due to thermal fluctuations but by quantum fluctuations at a so-called quantum critical point. These quantum fluctuations

are induced by non-thermal parameters like magnetic field, pressure or chemical doping such that quantum phase transitions occur only at zero temperature. In many cases quantum phase transitions are second-order transitions.

Fig. 4.2 presents two schematic phase diagrams in the vicinity of a quantum critical point. In Fig. 4.2 (a), an ordered phase exists only at $T = 0$. This is exemplified by one- and two-dimensional Ising systems, where magnetic order is suppressed due to the Mermin-Wagner theorem [112]. In this case, no quantum phase transition is observed in reality. Nevertheless, the quantum critical point affects the phase diagram for $T \neq 0$, dividing it into three different regions separated by crossovers. In the thermally disordered regime, the long-range order is suppressed by thermal fluctuations. In the quantum disordered regime, it is suppressed by quantum fluctuations resulting from Heisenberg's uncertainty principle. The region between these two regimes is known as the quantum critical region. In this region in the vicinity of $r = r_c$, the quantum critical ground state is affected by the thermal fluctuations, which may result in unusual finite-temperature properties.

Fig. 4.2 (b) shows a phase diagram in which the ordered phase extends to finite temperatures. This allows for the observation of a phase transition in close proximity to the quantum critical point. As the temperature decreases, the classical critical region, where the phase transition is dominated by thermal fluctuations becomes narrower with decreasing temperature. The quantum critical region in Fig. 4.2 (b) behaves analogously to the case of order at only $T = 0$ in (a).

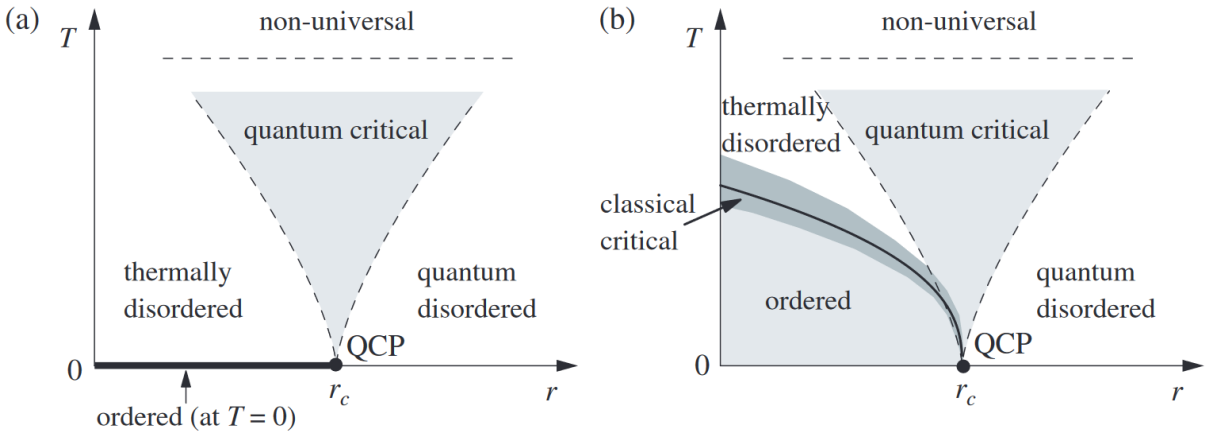

Figure 4.2: Schematic phase diagrams of systems with a quantum critical point with an ordered phase only at $T = 0\,\mathrm{K}$ (a) and for $T > 0\,\mathrm{K}$ (b). Figure taken from Ref. [108].

Research has demonstrated, that the presence of a quantum critical point strongly influences the physical properties at $T > 0$. The distinctive effects resulting from the unique fingerprint of a quantum critical point can persist up to relatively high temperatures. For

instance, $CePd_2Si_2$ exhibits a superconducting phase pocket in the vicinity of the quantum critical point upon the application of pressure [113], while $YbRh_2Si_2$ shows non-Fermi liquid behavior in a magnetic field [114]. In $CoNb_2O_6$, an energy spectrum governed by an emergent E8 symmetry was observed in the vicinity of a quantum critical point in a magnetic field transverse to the Ising axes [16].

4.2 Quasi-1D Ising chain magnetism in $CoNb_2O_6$

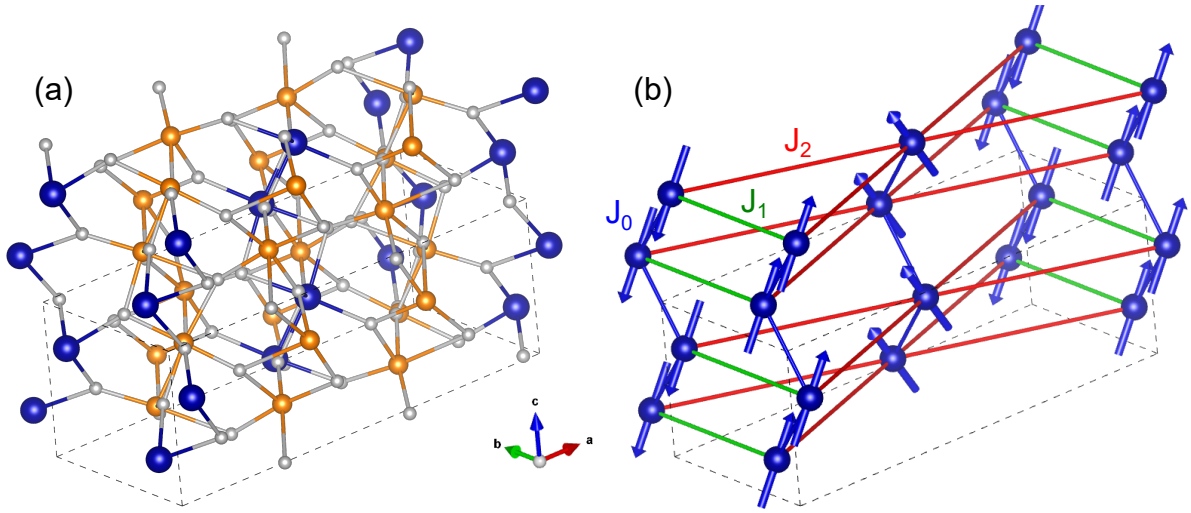

Figure 4.3: Atomic and magnetic lattice of $CoNb_2O_6$. (a) Crystal structure of $CoNb_2O_6$ with cobalt atoms in blue, niobium atoms in orange and oxygen atoms in grey. (b) Magnetic sublattice consisting of the cobalt atoms only. The directions of the Ising axes of the magnetic moments of the cobalt atoms is visualized by blue arrows. The blue lines connecting different cobalt atoms illustrate the ferromagnetic intra-chain coupling J_0 between different spins. The green and red lines visualize the different antiferromagnetic inter-chain couplings J_1 and J_2 between the spin chains. The crystal unit-cell is indicated by the dotted lines. Adapted from Ref. [42].

The orthorhombic compound $CoNb_2O_6$ is considered to be a prototype realization of a quasi one-dimensional Ising system [16, 102, 105, 107, 118–122]. A one-dimensional Ising system in a transverse magnetic field is in turn an archetypical example of a system exhibiting a quantum phase transition.

$CoNb_2O_6$ crystallizes in the orthorombic columbite structure with the space group *Pbcn* and lattice constants $a = 14.1475\,\text{Å}, b = 5.721\,\text{Å}$, and $c = 5.045\,\text{Å}$, as shown in Fig. 4.3 [36, 42, 123–125].The unit cell of the crystal structure is indicated by a dotted cuboid.

The cobalt atoms are arranged in a zig-zag chain-like pattern along the *c*-direction. Within the *ab*-plane, the cobalt atoms are arranged in isosceles triangles. The oxygen atoms in gray span an octahedron around each cobalt atom. The resulting crystal electric field in

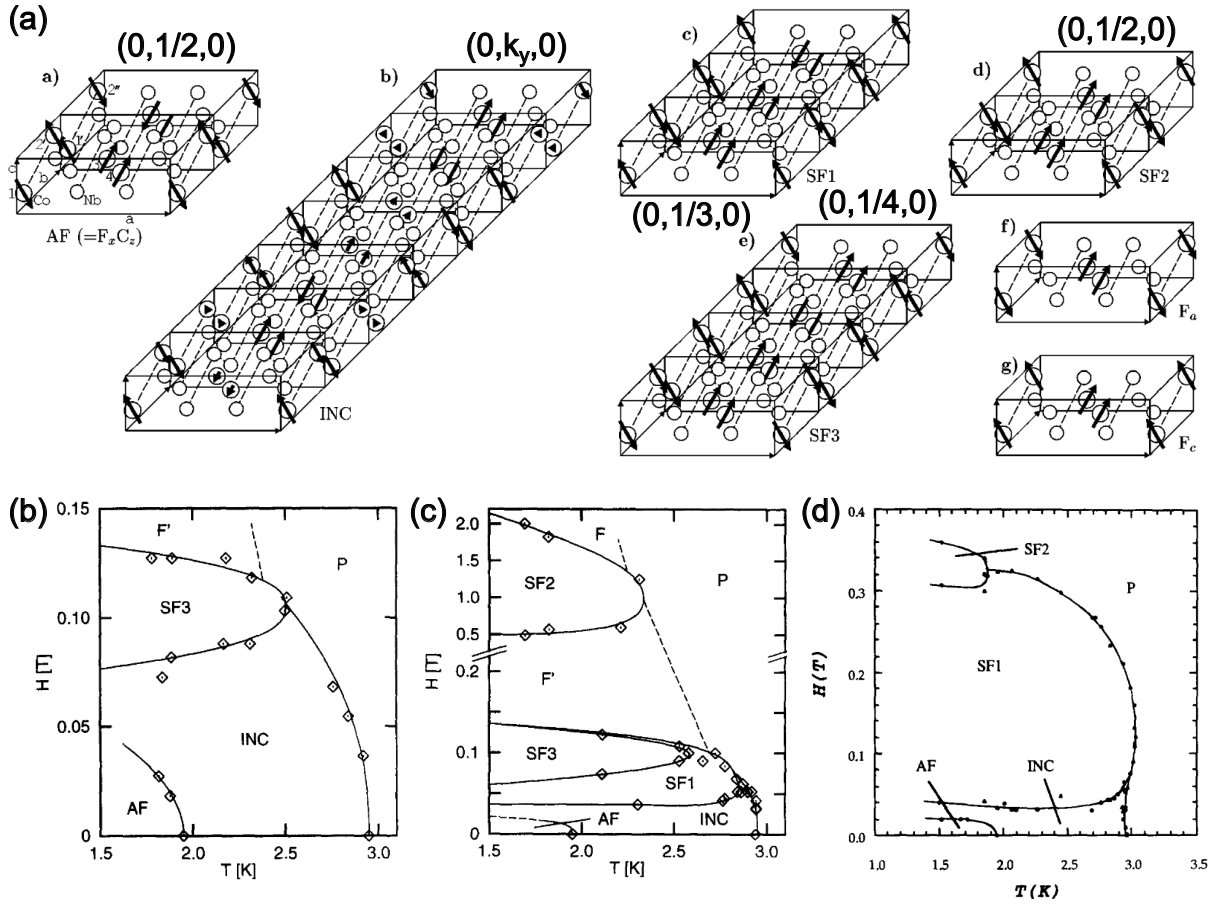

Figure 4.4: Magnetic phase diagrams for magnetic fields applied in different directions within the easy plane. (a) Visualizations of the different magnetic phases observed within the magnetic easy plane. For every supercell, the modulation vector $\vec{k}$ was added. In the case of the INC ordering, k_y takes values between 0.37 and 0.48 depending on temperature and applied magnetic field [115, 116]. Taken from Ref. [116]. (b) Phase diagram for field applied parallel to the a-axis. Diagram taken from Ref. [117]. (c) Phase diagram for field applied in a not specified direction between the a-axis and the c-axis. Diagram taken from Ref. [117]. (d) Phase diagram for field applied parallel to the c-axis. Diagram taken from Ref. [115].

combination with spin-orbit coupling induces an effective spin-1/2 magnetic moment on every cobalt atom with a magnitude of approximately $3\,\mu_B$ [37, 124]. The combination of spin-orbit coupling and the crystal environment is responsible for the Ising anisotropy with two easy axes lying in the ac-plane enclosing angles of $\pm$ 31° with the c-axis [17, 35, 42, 116, 126–128] (34° in Ref. [124], 29.6° in Ref. [115]). The two different directions of Ising axes give rise to a single hard axis along the $\langle 010 \rangle$ direction of the system.

The magnetic interaction between the cobalt moments is predominantly ferromagnetic. It is mediated by the superexchange along the c-direction and has a 1D-character [37]. The ferromagnetic interaction becomes relevant below 25 K [35, 36, 42, 125]. Due to the

Mermin-Wagner theorem, magnetic long range order is forbidden in one-dimensional and two-dimensional systems for temperatures above absolute zero. However, weak antiferromagnetic inter-chain couplings J_1 along the b-direction (shown as green lines in Fig. 4.3) and J_2 perpendicular to the c-direction (shown as red lines in Fig. 4.3) circumvent the Mermin-Wagner theorem. As a result of the combination of all interactions, the system develops long-range order below $T_{\mathrm{INC}} \approx 3\,\mathrm{K}$.

Between 2 K and 3 K the magnetic order of the cobalt moments is incommensurate and was identified as a spin-density wave along the b-direction with varying modulation vectors between (0,0.37,0) and (0,0.48,0) [37, 38, 115, 116, 118, 128]. The incommensurate magnetic structure (INC) is shown in Fig. 4.4 (a). Under decreasing temperature in zero magnetic field, a first-order transition was observed resulting in a commensurate antiferromagnetic order with the propagation vector (0,0.5,0) below 2 K [115, 118, 128]. This antiferromagnetic structure (AF) is also shown in Fig. 4.4 (a). At temperatures below 1 K, frequency-dependent signatures in the magnetic susceptibility [36, 42, 125] and an unusual behavior in calorimetric measurements indicate an anomalous behavior referred to as glassy or freezing behavior [35, 42, 125].

A plethora of studies have investigated the magnetic transitions and properties of $CoNb_2O_6$ and the corresponding phase boundaries when exposed to a magnetic field. These studies focus primarily on magnetic fields within the easy ac-plane [115–118, 124–126, 129], but also for fields applied parallel to the magnetically hard b-axis [35, 124, 130]. Different published magnetic phase diagrams for magnetic fields within the easy-plane and visualizations of the corresponding spin structures are shown in Fig. 4.4.

Fig. 4.4 (b) illustrates the magnetic phase diagram for a magnetic field parallel to the a-axis. In this scenario, a spin-flip phase (SF3) was observed above approximately 75 mT. At a critical magnetic field of 130 mT, a second spin-flip takes place resulting in a field-polarized phase (F'). In Fig. 4.4 (c) the magnetic phase diagram for the case of a magnetic field bisecting the a-axis and the c-axis is shown, featuring a manifold of different spin-flip transitions and phases (SF1, SF2, and SF3) [116, 117]. A magnetic field applied parallel to the c-axis gives rise to the phase diagram shown in Fig. 4.4 (d). For this configuration, the incommensurate phase (IC) is suppressed for fields above $H_{c1} \approx 40$ mT by the spin-flip phase SF1. An additional spin-flip phase pocket (SF2) emerges at temperature below 2 K and magnetic fields between $H_{c2} = 300\,\mathrm{mT}$ and 380 mT [115, 116, 124, 131]. Above 360 mT, the system was observed to be in a field-polarized paramagnetic phase. At lowest temperatures below 1.5 K, a hysteretic behavior of the phase transitions depending on the magnetic field sweep direction was reported [118, 132].

The angular dependence of the magnetization when canting the magnetic field direction from the easy c-axis towards the hard b-axis was subject of an early study by Maartense et al. [124]. The results show a $1/\cos(\theta_{bc})$ dependence of the critical transition fields observed when θ_{bc} is the angle in the bc-plane between the magnetic field and the c-axis. This behavior suggests that the magnetic properties are dominated in first approximation by the magnetic field projection perpendicular to the b-axis. In the close vicinity of the b-axis, however, this picture doesn't hold any more as the quantum criticality of the individual Ising chains in the transverse field component needs to be taken into account.

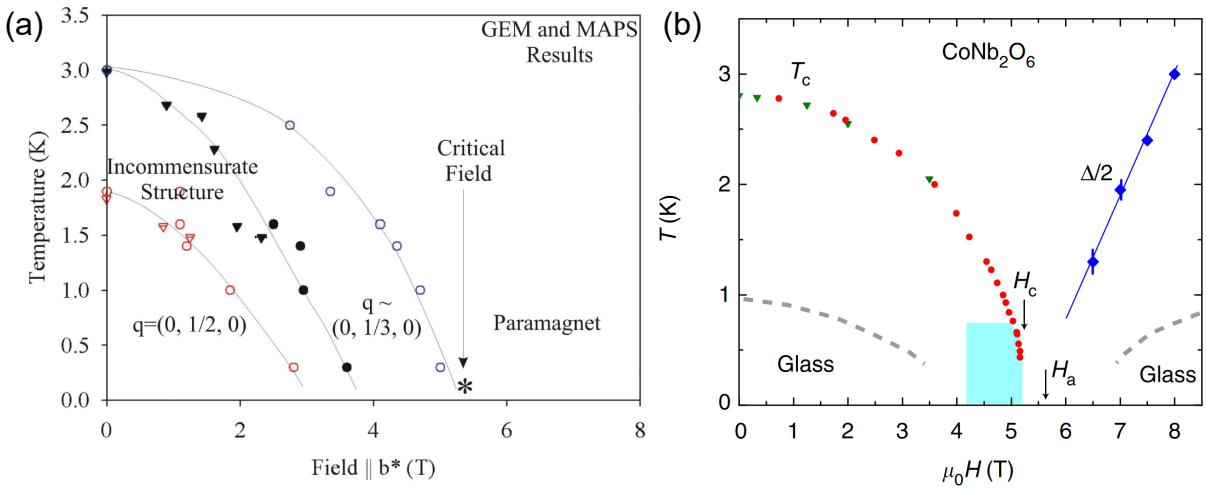

Figure 4.5: Former studies of the magnetic phase diagram for magnetic fields stated to be parallel to the b-axis. (a) Magnetic phase diagram drawn on the basis of neutron diffraction experiments. Diagram taken from Ref. [130]. (b) Magnetic phase diagram extracted from heat capacity measurements. Diagram taken from Ref. [35].

First studies focusing on the quantum phase transition in $CoNb_2O_6$ for a field applied parallel to the b-axis were carried out as part of a doctoral thesis using elastic and inelastic neutron diffraction experiments [130]. A central result of this study concerns the evolution of the magnetic phase boundaries under increasing magnetic field. The phase diagram extracted from these neutron diffraction experiments is shown in Fig. 4.5 (a). Between the incommensurate phase and the paramagnetic phase, the emergence of a spin-flip phase with modulation vector (0,1/3,0), equivalent to the SF1 phase induced by a magnetic field parallel to the c-direction, was observed. Furthermore, the quantum critical field was extracted from preliminary inelastic neutron diffraction experiments by R. Coldea showing an incomplete gap closing with an energy gap minimum at a magnetic field of $H_c = 5.3\,\mathrm{T}$.

The only published magnetic phase diagram for a transverse field geometry is extracted from a heat capacity study of $CoNb_2O_6$ [35] and is shown in Fig. 4.5 (b). The phase boundary between the paramagnetic and the ordered magnetic phase is marked by red circles and green triangles. However, in the heat capacity data presented in this publication, signatures of the incommensurate to antiferromagnetic transition at 2 K in zero field are missing. Consequently, the phase boundary between the incommensurate phase and the antiferromagnetic phase with propagation vector $q = (0, 1/2, 0)$ presented in the phase diagram in Fig. 4.5 (a) is completely missing in Fig. 4.5 (b). The gray dashed lines mark the phase boundaries of a glassy state, that was identified by an unusual frequency dependence of the thermal relaxation behavior in ac calorimetry measurements. The blue symbols illustrate the energy gap extracted from a fit of the measured heat capacity to the free fermion solution of the isolated Ising chain in a transverse field.

Ultrasound velocity measurements revealed a distinct softening of the elastic constant C_{66} towards the quantum critical point due to spin-orbit-strain-coupled fluctuations [133]. Domain growth kinetics also play a central role for $CoNb_2O_6$ at very low temperatures. Unexpected low power law dependencies of domain growth were found in neutron diffraction and ac susceptibility measurements [42, 126, 134].

A majority of the central literature focusing on $CoNb_2O_6$ concern spectroscopic measurements in transverse magnetic fields. As was derived theoretically by Zamolodchikov, the energy spectrum of the excited states of weakly coupled Ising chains match specific ratios at the quantum critical point [29]. The ratio between the energies of the first two excited states, for instance, is predicted to be the golden ratio. This is in accordance to the energy spectrum of a system with an emergent E8 symmetry where E8 describes a Lie group.

The first experimental observation of an E8 energy spectrum in $CoNb_2O_6$ was provided by inelastic neutron diffraction measurements where the ratio between the energies of the first two excited states was observed to approach the golden ratio towards a critical field of $B_{c,1D} \approx 5\,\mathrm{T}$, below the transition to the paramagnetic phase at $B_{c,3D} = 5.5\,\mathrm{T}$ [16]. Fig. 4.6 presents the central results of the study conducted by Coldea et al. In this study, the antiferromagnetic inter-chain coupling was modeled by adding a simple mean field term in the Hamiltonian. Figs. 4.6 (A) and (B) show energy scans at 4.5 T and 5 T. For both magnetic fields, two excited states, labeled m_1 and m_2, are observed. Figs. 4.6 (C) and (D) illustrate, that the energy ratio of the two excited states approach the golden ratio in the vicinity of 5 T, characteristic for a system exhibiting an E8 symmetry. The presence of an energy spectrum consistent with the energy spectrum of an emergent E8 symmetry was later also observed by means of THz-Spectroscopy [101]. Additional theoretical studies shed further light on the details of the Hamiltonian describing experimental observations

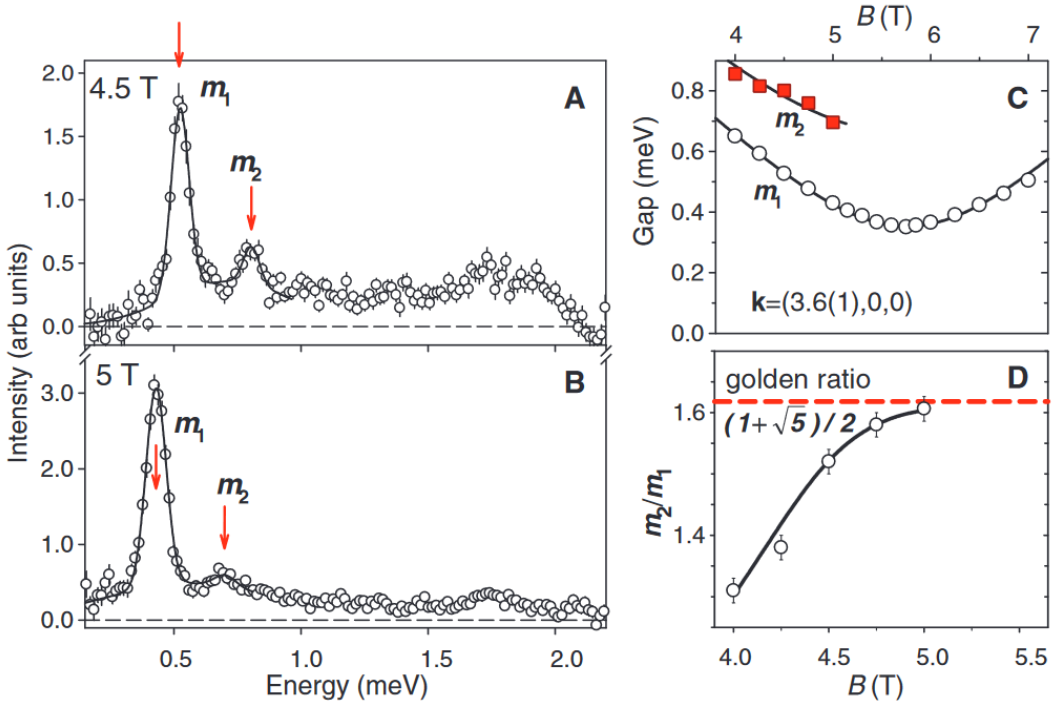

Figure 4.6: Magnetic-field dependence of the excited stated of $CoNb_2O_6$. (A) and (B) Observed neutron intensity as function of energy transfer at magnetic fields of 4.5 T and 5 T respectively. (C) Magnetic-field dependence of the energy gaps of the first two excited states. (D) Magnetic-field dependence of the ratio of the energies of the first two excited states approaching the golden ratio in the vicinity of the quantum critical point. Figure taken from Ref. [16].

in the ordered phase and the quantum paramagnetic phase, respectively [102, 135]. The single-ion properties, in particular the single-ion energy levels, the wave function of the crystal electric field and the g-factor were investigated by means of inelastic neutron scattering and paramagnetic resonance measurements [17].

Further studies focused on the understanding of the nature of the inter-chain and intra-chain interactions. The effect of different antiferromagnetic couplings on the resulting magnetic order was subject of a theoretical investigation [105]. In this study, the Ising chains were arranged in a triangular pattern with antiferromagnetic coupling and the influence of an isoscele distortion of the couplings on the magnetic order in a transverse field at zero temperature was evaluated. The effect of uniaxial pressure on the frustration of the interchain couplings was investigated using neutron diffraction by Kobayashi et al. [106]. Recent studies studies have dealt with modifications of the simple ferromagnetic exchange term considering a doubling of the unit cell along the chain due to a buckled ferromagnetic exchange [1, 18]. Inelastic neutron scattering experiments in the quantum paramagnetic regime revealed the need for two magnetic sites to model the experimental

data sufficiently [1]. Conceptually similar, a two site model advertised as twisted Kitaev chain was introduced to model Thz-spectroscopy data [18]. In consequence, recent interest has grown in the theoretical study of ferromagnetic Kitaev chains and perturbed Ising chain systems [22–24, 136–138]. The effective Hamiltonian became increasingly elaborate, including soliton and spinon excitations, in order to achieve a more accurate modeling of the experimental spectroscopy results to the best extent [19, 20, 139]. Recent work proposed a modified version of the Hamiltonian from Ref. [1] with a more elaborate treatment of the interchain actions to model the experimental observations. This modified Hamiltonian is characterized by an emergent $D_8^{(1)}$ symmetry instead of an E8 symmetry at the quantum critical point [140].

4.3 Single-Crystal Growth and Characterization

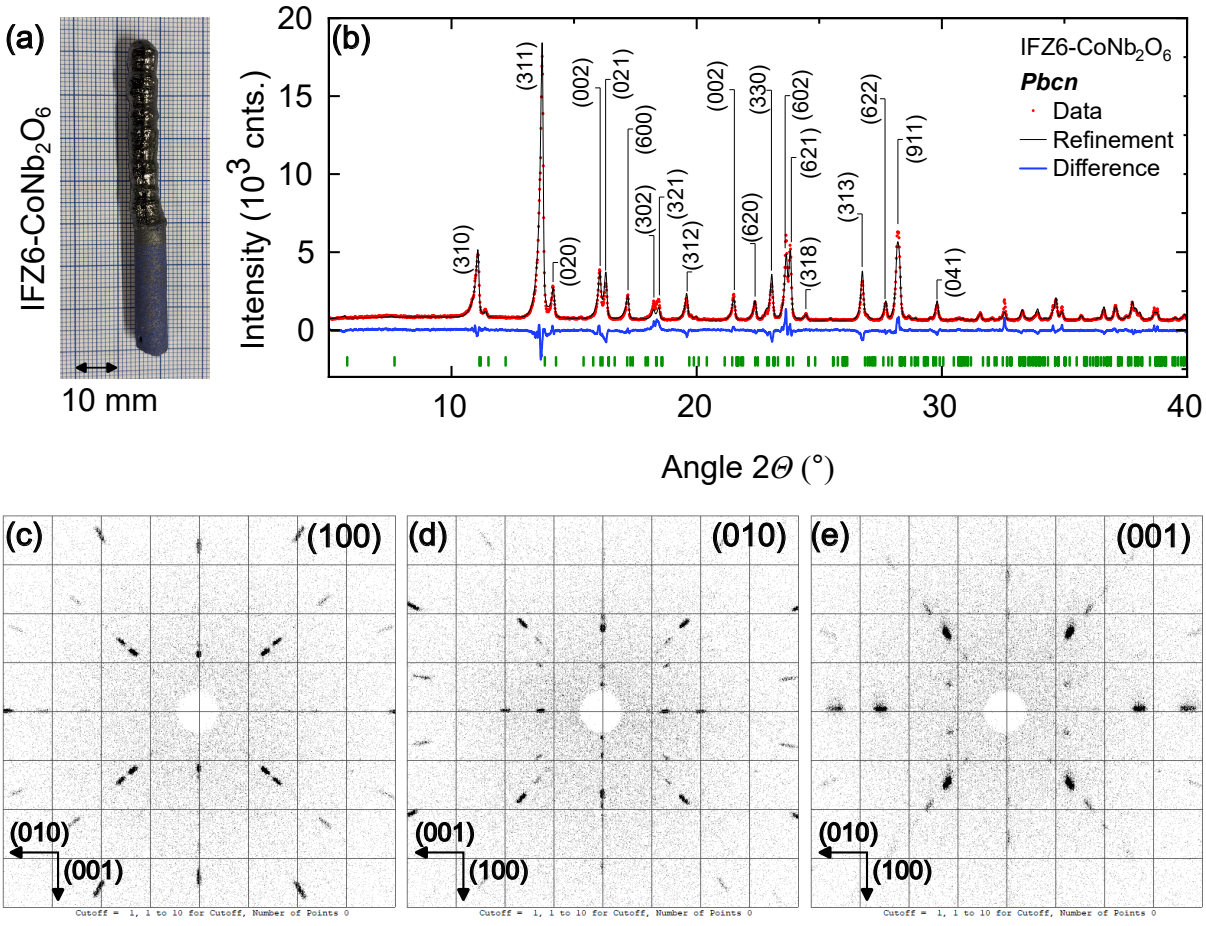

Figure 4.7: X-Ray diffraction with $CoNb_2O_6$: (a) Single-crystalline pieces of $CoNb_2O_6$. (b) Powder diffraction pattern and refinement. (c-e) Laue diffraction patterns along the three major orthorhombic axes.

Two successful growth attempts were carried, yielding two single crystals of $CoNb_2O_6$ referred to as IFZ2 and IFZ6. From the growth attempt IFZ2, a cuboid sample was prepared with a size of $1.8 \times 2.6 \times 2.4$ mm along the a, b, and c axes and a mass of 62.6 mg. This cuboid, labeled as IFZ2-A, was used for the preliminary magnetization, susceptibility and heat capacity measurements presented in section 4.4. The key measurements, namely the measurement of the transverse susceptibility, the heat capacity and the magnetocaloric effect down to milli-Kelvin temperature, were carried out on a spherical sample prepared from the growth attempt IFZ6. The spherical sample, labeled as IFZ6-A, has a diameter of 2.8 mm and a mass of 67.8 mg.

Fig. 4.7 (a) shows an image of the growth attempt IFZ6. From this attempt, float-zoned leftover material from the sample preparation was used for powder diffraction. Fig. 4.7 (b) displays the resulting powder diffraction pattern. The Rietveld refinement indicates excellent agreement with the experimental data. Moreover, no secondary phase is observed in the diffraction pattern. Laue diffraction patterns in Fig. 4.7 (c)-(e) demonstrate a good single crystallinity of sample IFZ6-A.

4.4 Magnetic Properties for magnetic fields applied parallel to high symmetry directions

Before delving into the thermodynamic properties of $CoNb_2O_6$ in a transverse magnetic field, the results of measurements for its characterization in zero magnetic field and for magnetic fields applied along the high symmetry directions are presented. Fig. 4.8 shows the temperature dependence of specific heat and ac susceptibility in zero magnetic field. All panels use a double-logarithmic scale.

The specific heat exhibits two prominent peaks at temperatures of $T_{\mathrm{INC}} = 2.98\,\mathrm{K}$ and $T_{\mathrm{N}} = 1.99\,\mathrm{K}$, as shown in Fig 4.8 (a). The peak at T_{INC} is in agreement with the literature. This peak indicates the phase transition from the paramagnetic phase to an incommensurate antiferromagnetic phase. The peak at T_{N} marks the phase transition from the incommensurate to an commensurate antiferromagnetic phase. However, the literature reports a shoulder at T_{N} rather than a sharp peak [42, 125]. Below 2 K, the specific heat decreases sharply.

The high-temperature part of the specific heat is tracked by data from $ZnNb_2O_6$, a non-magnetic analog (data taken from Ref. [125]). The specific heat curve of $CoNb_2O_6$ begins to deviate from the behavior of $ZnNb_2O_6$ for temperatures below 20 K. The difference between these two curves are a result of the magnetic contributions to the specific heat in $CoNb_2O_6$.

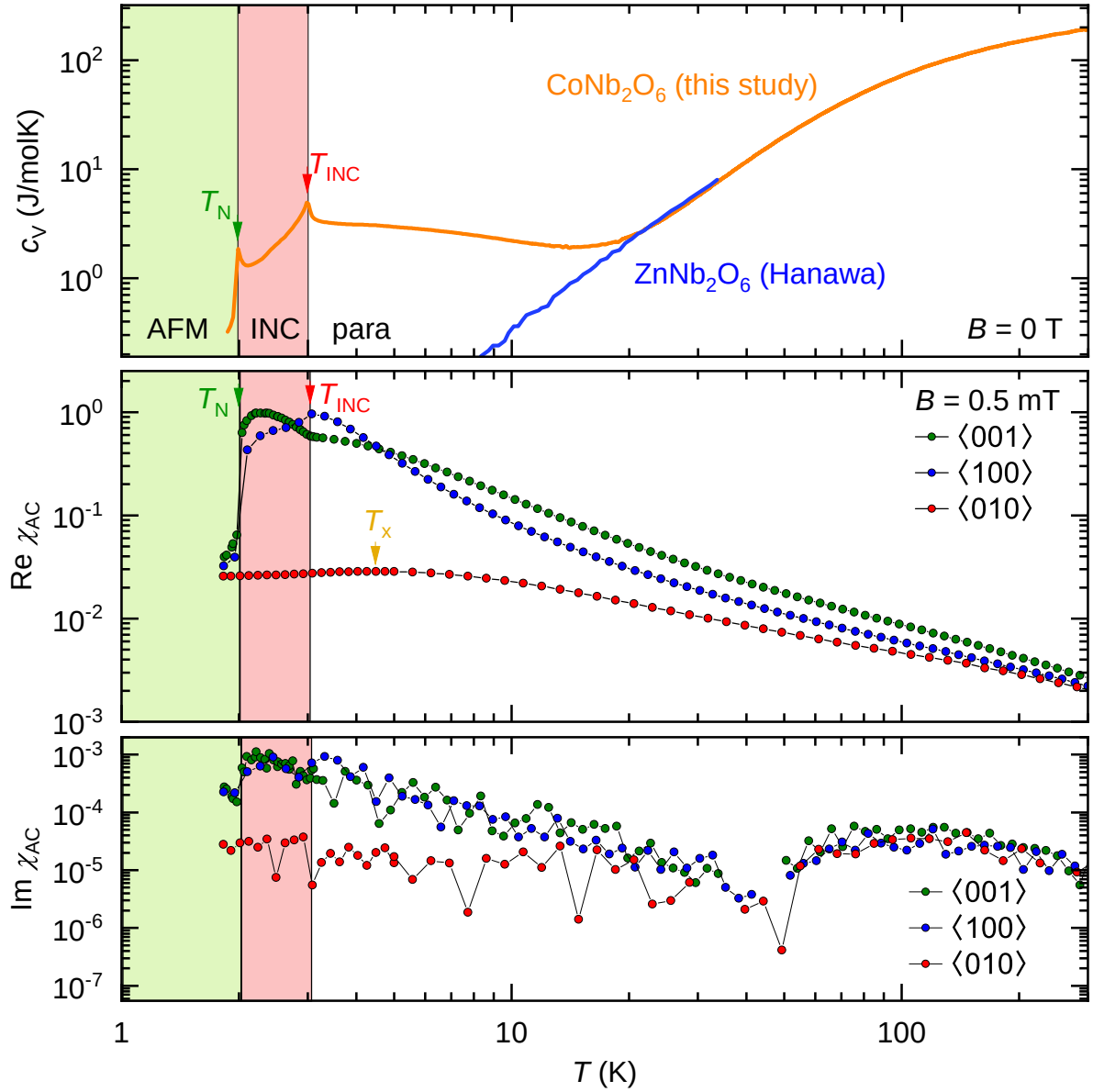

Figure 4.8: Thermodynamic properties. (a) Specific heat as a function of temperature for zero magnetic field with a double logarithmic scale. As a measure of the phonon contribution, data for nonmagnetic $ZnNb_2O_6$ is shown (blue curve) (Taken from Ref. [125]) in order to illustrate the phononic contribution to the specific heat of $CoNb_2O_6$. (b) and (c) Real and imaginary part of the longitudinal ac susceptibility as a function of temperature with a double logarithmic scale. The susceptibility was measured along the three orthorombic axes with a small applied field of 0.5 mT.

Fig. 4.8 (b) displays the temperature dependence of the real part of the longitudinal ac susceptibility along the three major crystallographic axes in a small magnetic field of 0.5 mT. The real parts of the ac susceptibility parallel to the ⟨100⟩ and ⟨001⟩ are in good agreement with the literature [37, 42, 125].

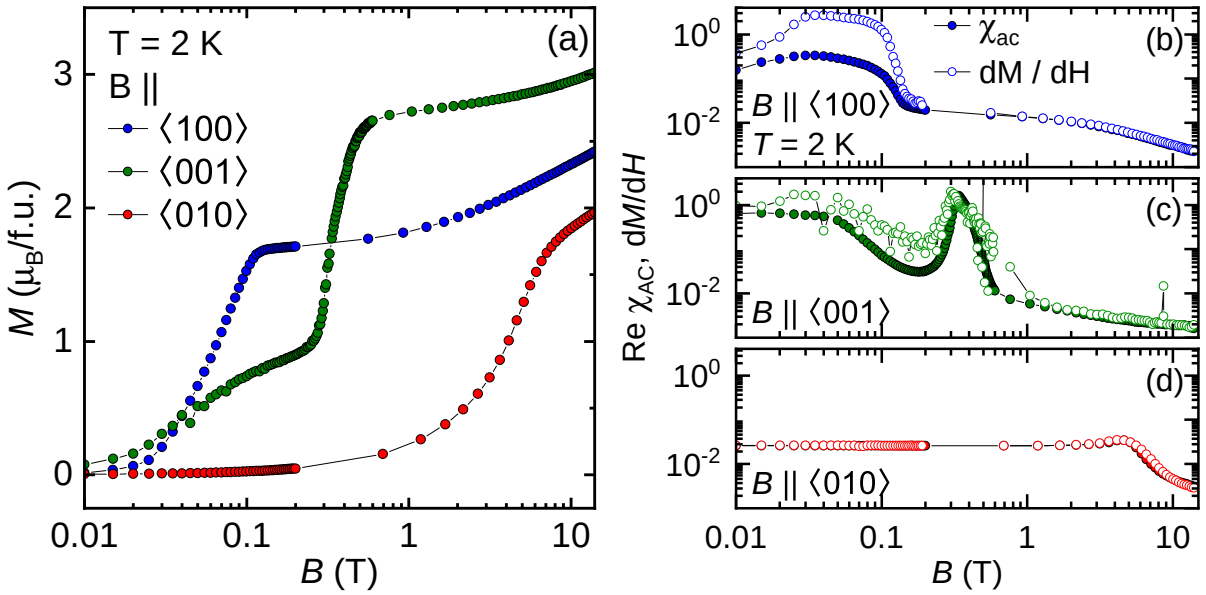

Figure 4.9: Magnetic field dependence of the magnetization and the susceptibility: (a) Magnetization along the three orthorombic axes as a function of magnetic field on a logarithmic scale. (b) Temperature dependence of the real part of the longitudinal ac susceptibility (solid symbols) in comparison with the derivative of the magnetization (open symbols) on a double logarithmic scale.

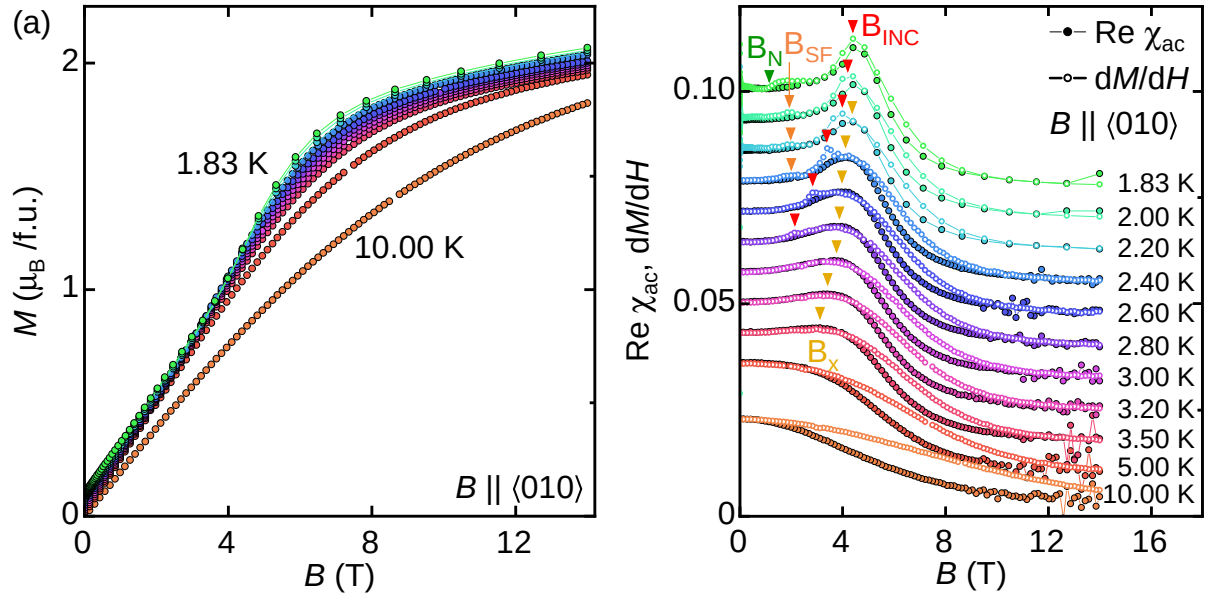

Figure 4.10: Magnetic field dependence of the magnetization and the susceptibility: (a) Magnetization along the ⟨010⟩ direction for different temperatures. (b) Real part of the longitudinal ac susceptibility and the derivative of the magnetization for various temperatures. The data in (b) is plotted with constant offsets.

A maximum in the ⟨100⟩ susceptibility and a kink in the ⟨001⟩ susceptibility at $T_{\mathrm{INC}} = 3.04\,\mathrm{K}$ mark the transition from the paramagnetic phase to the incommensurate anti-

ferromagnetic phase. Sharp drops in the susceptibilities parallel to the ⟨100⟩ and ⟨001⟩ directions at $T_N = 1.99\,K$ mark the transition from the incommensurate phase to the commensurate antiferromagnetic phase. The susceptibility parallel to the ⟨010⟩ direction shows no distinct signature, but rather a very broad maximum centered around $B_x = 4.49\,K$. This maximum may indicate a crossover from the paramagnetic regime to a regime dominated by the anisotropy of the cobalt spins.

Fig. 4.8 (c) shows the temperature dependence of the imaginary part of the ac susceptibility. The imaginary part of the susceptibility is several orders of magnitude smaller and shows no discernible signatures for all measured directions.

The second part of the preliminary thermodynamic characterization of the $CoNb_2O_6$ samples concerns the magnetic field dependence of the magnetic properties. Fig. 4.9 shows the magnetic field dependence of the magnetization and the longitudinal ac susceptibility at a constant temperature of 2 K.

The field dependence of the magnetization and the longitudinal ac susceptibility was measured along the three major crystallographic axes, as shown in Fig. 4.9 (a). Along the ⟨100⟩ direction, the magnetization increases steeply above 0.03 T and reaches a field polarized state at 0.13 T. The magnetization then increases with a smaller slope as the magnetic field increases further, possibly due to a canting of spins away from their local Ising axis. The behavior described can be observed more clearly in the derivative of the magnetization dM/dH, as shown in comparison with the ac susceptibility in Fig. 4.9 (b). For small magnetic fields, dM/dH increases slightly. However, at 0.13 T, dM/dH decreases sharply as the magnetic field increases. The ac susceptibility behaves similarly, but is larger in the magnetically ordered regime below 0.13 T.

For field along the ⟨001⟩ direction, the magnetization exhibits a two-step behavior. Below, 0.03 T, the slope of the magnetization curve increases upon application of a magnetic field. Above 0.05 T, the slope of the magnetization decreases again before rising sharply above 0.26 T. Above a magnetic field of 0.4 T, the slope of the magnetization then decreases again due to the onset of the saturation of the magnetic moments. At higher fields, the magnetization increases gradually. This behavior is also visualized in the dM/dH and the ac susceptibility curve, as shown in Fig. 4.9 (c). Notably, the ac susceptibility exhibits distinct signatures at 0.05 T (change of slope) and at 0.34 T (maximum).

The magnetization for field along the ⟨010⟩ axis is smaller than for the other two field directions, as shown in Fig. 4.9 (a). The magnetization increases continuously with the maximum slope occurring at a magnetic field of approximately 4.14 T. The field derivative of the magnetization dM/dH and the real part of the ac susceptibility are in

good agreement, as shown in Fig. 4.9 (d). In both curves, the maximum is observed at a magnetic field of 4.14 T.

In the following, the focus is on the magnetic properties for a magnetic field applied transverse to the Ising axes of $CoNb_2O_6$. Measurements of the magnetization and the longitudinal susceptibility provide first insights into the magnetic behavior of $CoNb_2O_6$ at temperatures above 1.83 K. Detailed measurements of the magnetic field dependence of the magnetization and the ac susceptibility parallel to the $\langle 010 \rangle$ direction are presented in Fig. 4.10. Fig. 4.10 (a) presents the magnetic field dependence of the magnetization along the $\langle 010 \rangle$ direction measured between 1.83 K and 10 K and fields of up to 14 T. At 10 K, the behavior of the magnetization indicates paramagnetic behavior as a function of magnetic field. With decreasing temperature the magnetization curves start to deviate from the paramagnetic behavior. At 1.83 K, the magnetization is consistent with the theoretical prediction for the magnetization of an Ising chain in a transverse magnetic field at zero temperature [141, 142].

Fig. 4.10 (b) shows a comparison between the ac susceptibility and the derivative of the static magnetization measured as a function of field parallel to the $\langle 010 \rangle$ direction for temperatures from 1.83 K to 10 K. At 10 K, both the ac susceptibility and $\mathrm{d}M/\mathrm{d}H$ decrease monotonically as the magnetic field increases. However, for a simple paramagnet, it is expected that these two curves should be identical to each other. In this case, the ac susceptibility decreases faster than $\mathrm{d}M/\mathrm{d}H$. This may be due to the presence of ferromagnetic fluctuations at this temperature, resulting in slow reorientation processes. The differences between the ac susceptibility and $\mathrm{d}M/\mathrm{d}H$ in the paramagnetic regime become smaller as the temperature decreases.

With decreasing temperature, a broad maximum emerges in both the ac susceptibility and $\mathrm{d}M/\mathrm{d}H$ simultaneously. This maximum is first observed in the magnetic fields dependence at a temperature of 3.5 K and at a magnetic field $B_\mathrm{x} = 3.11\,\mathrm{T}$ and is located in the paramagnetic regime. This maximum indicates a crossover to a regime dominated by the anisotropy of the cobalt magnetic moments. At a temperature of 2.8 K, a small kink appears at a magnetic field of $B_\mathrm{C} = 2.12\,\mathrm{T}$. This kink is identified as a result of the phase transition from the paramagnetic phase to the incommensurate magnetic phase. This kink shifts to larger magnetic fields as the temperature decreases and becomes a maximum. Between temperatures of 2 K and 2.4 K, a small hump appears at a magnetic field of $B_\mathrm{SF} \approx 2\,\mathrm{T}$. This hump can most likely be associated with a spin-flip transition due to a slight misalignment of the sample with respect to the magnetic field direction. This is consistent with phase diagrams presented in section 4.5.2.

At the lowest temperature of 1.83 K, there appears to be an increase in $\mathrm{d}M/\mathrm{d}H$ at a magnetic field of $B_\mathrm{N} = 1.14\,\mathrm{T}$. The position of this increase is in line with the transition fields obtained from the transverse susceptibility measurements for the phase boundary of the commensurate antiferromagnetic phase.

An additional maximum is observed in the paramagnetic regime. This broad maximum emerges at a temperature of 3.5 K at a magnetic field $B_\mathrm{x} = 3.11\,\mathrm{T}$. In analogy to the maximum of the susceptiblity along the $\langle 010 \rangle$ direction observed in Fig. 4.8 (b), the maximum here may also indicate a crossover from a regime dominated by the anisotropy of the magnetic system to the paramagnetic regime. As the temperature decreases, the maximum shifts to larger magnetic fields. Towards the lowest temperatures presented in this panel, the maxima at B_x and B_INC merge to a single maximum.

4.5 Thermodynamic Properties for a magnetic field parallel to $\langle 010 \rangle$

In the following, the results of the detailed measurements of the transverse susceptibility, the heat capacity and the magnetocaloric effect are presented for a static magnetic field (dominantly) parallel to the $\langle 010 \rangle$ direction. Although $CoNb_2O_6$ is a prominent example for the study of quantum phase transitions of an Ising chain in a transverse magnetic field, a detailed hard-axis magnetic phase diagram for this material is still missing in the literature. A central result of this work is a detailed transverse-field magnetic phase diagram for $CoNb_2O_6$ based on measurements of the thermodynamic quantities.

4.5.1 Susceptibility in Transverse Magnetic Fields

Figure 4.11 shows the transverse-field magnetic phase diagram obtained from susceptibility and calorimetric measurements. The underlying color plots in Fig. 4.11 (a) and (b) show the real and imaginary part of the transverse susceptibility, respectively, with purple color representing small values and red color representing large values. The data points were inferred from measurements of the transverse susceptibility, the heat capacity, and the magnetocaloric effect, indicating the boundaries between the different magnetic phases. The extent of the paramagnetic phase (para), the incommensurate phase (IC), and the commensurate antiferromagnetic phase (AFM) are displayed in both panels of Fig. 4.11. Additionally, two region labeled as 'glassy' are shown. In equivalence to literature results, $CoNb_2O_6$ exhibits an unusual thermal relaxation in these glassy regions [35]. Measurements of the longitudinal susceptibility indicate an additional regime outside of the ordered phase and characterized by a dominant anisotropy (AD). The boundary

between the paramagnetic phase and the anisotropy-dominated phase is observed as a maximum in the longitudinal susceptibility.

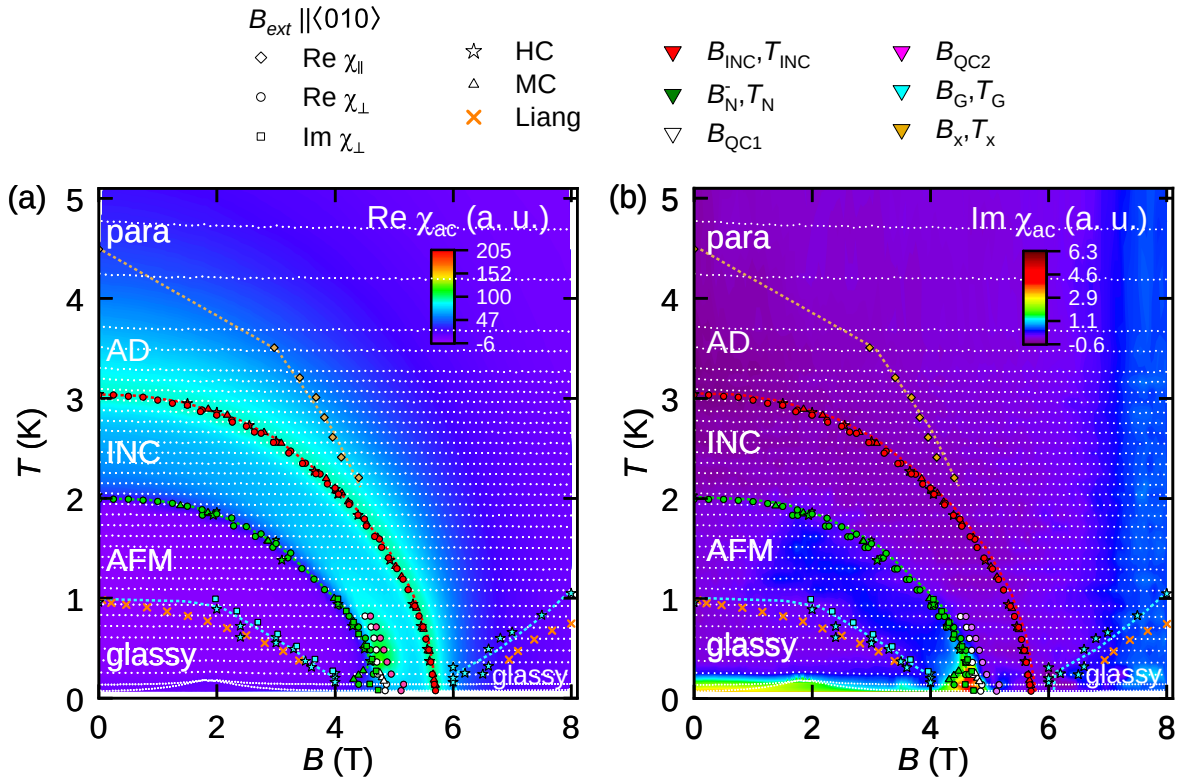

Figure 4.11: Color plots of the transverse susceptibility. (a) Real part of the transverse susceptibility. (b) Imaginary part of the transverse susceptibility. Data points were inferred from measurements of the longitudinal and transverse susceptibility, the heat capacity (HC), and the magnetocaloric effect (MC). White dots indicate where magnetic field sweeps were carried out. Data points indicating the boundaries of the glassy regime from Liang et al. [35] are also included.

Fig. 4.11 (a) and (b) show five distinct regimes in zero magnetic field. Starting at high temperatures, the paramagnetic phase (para) is stable down to $T_x = 4.49\,\mathrm{K}$. At T_x, a crossover is observed resulting in a regime dominated by the anisotropy of the cobalt moments (AD) down to and $T_{INC} = 3.04\,\mathrm{K}$. Between T_{INC} and $T_N = 1.94\,\mathrm{K}$, the incommensurate magnetic order (IC) is stabilized. At T_N, a first-order phase transition takes place from the incommensurate to a commensurate antiferromagnetic order. Below $T_G \approx 1\,\mathrm{K}$, an unusual thermal relaxation is observed which has been interpreted in the literature as a glassy behavior [35] or a freezing transition [42].

As the magnetic field increases, all transition temperatures, T_{INC}, T_N, and T_G, decrease continuously. The underlying color plot of the real part of the transverse susceptibility in

Transition temperature	Signature	Color
T_N	point of inflection extracted from the zero crossing of the second derivative of $\mathrm{Re}(\chi_{ac}^{\perp})$	green
T_{INC}	maximum in $\mathrm{Re}(\chi_{ac}^{\perp})$	red

Table 2: Overview of the signatures attributed to different phase transitions in the temperature dependence of the transverse susceptibility for perfect transverse-field orientation in Fig. 4.12

Fig. 4.11 (a) shows a maximal signal in the vicinity of T_{INC} and very low susceptibility in the antiferromagnetic phase below T_N. At temperatures below 1 K and magnetic fields slightly larger than B_N^-, additional fine structure is observed. This fine structure is located at the same position as signatures in the imaginary part of the transverse susceptibility and in the magnetocaloric effect indicating the presence of an additional phase pocket.

Fig. 4.11 (b) displays the same magnetic phase diagram with the imaginary part of the transverse susceptibility as color map. A slightly enhanced signal in the imaginary part of the susceptibility is observed in the temperature and magnetic field regime of the antiferromagnetic phase between T_N and T_G. The signal in this region is larger than in the glassy regime below T_G. In finite fields, the imaginary part of the susceptibility reveals a significant signal at low temperatures below 1 K near the magnetic field B_N^-. Additionally, for temperatures below 200 mK, the signal in the imaginary part of the transverse susceptibility is also enhanced for magnetic fields below B_N^-.

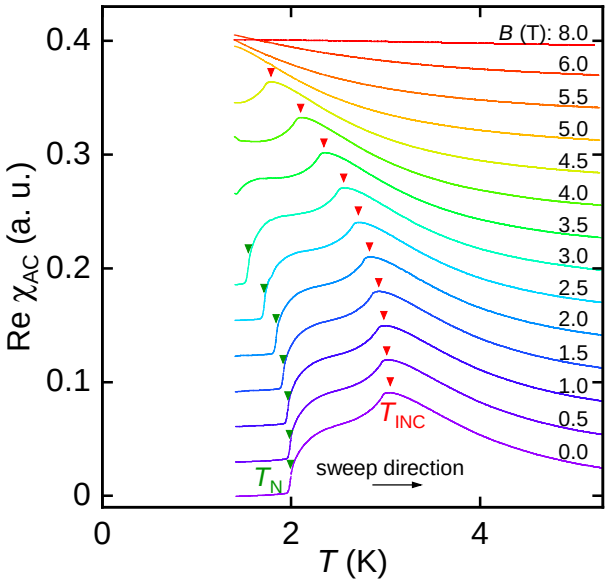

Figure 4.12: Temperature dependence of the transverse susceptibility for different transverse magnetic fields. The data is plotted with constant offsets.

The temperature dependence of the real part of the transverse susceptibility is shown in Fig. 4.12 covering temperatures between 1.4 K and 5.5 K and constant magnetic fields up to 8 T. The temperature dependence in zero magnetic field is consistent with literature and preliminary measurements conducted in the PPMS shown in Fig. 4.8 (b).

According to the literature, two signatures marking phase transitions can be identified in zero magnetic field. At $T_{\mathrm{INC}} = 3.04\,\mathrm{K}$, a maximum indicates the transition from the paramagnetic to the incommensurate phase. At $T_{\mathrm{N}} = 1.94\,\mathrm{K}$, the point of inflection can be associated with the transition from the incommensurate to commensurate antiferromagnetic phase. Both, the maximum at T_{INC} and the point of inflection at T_{N} shift to lower temperatures as the magnetic field increases. No additional signatures emerge with increasing magnetic field for temperatures above 1.4 K. Table 2 provides an overview of the signatures tracked in the temperature dependence of the transverse susceptibility.

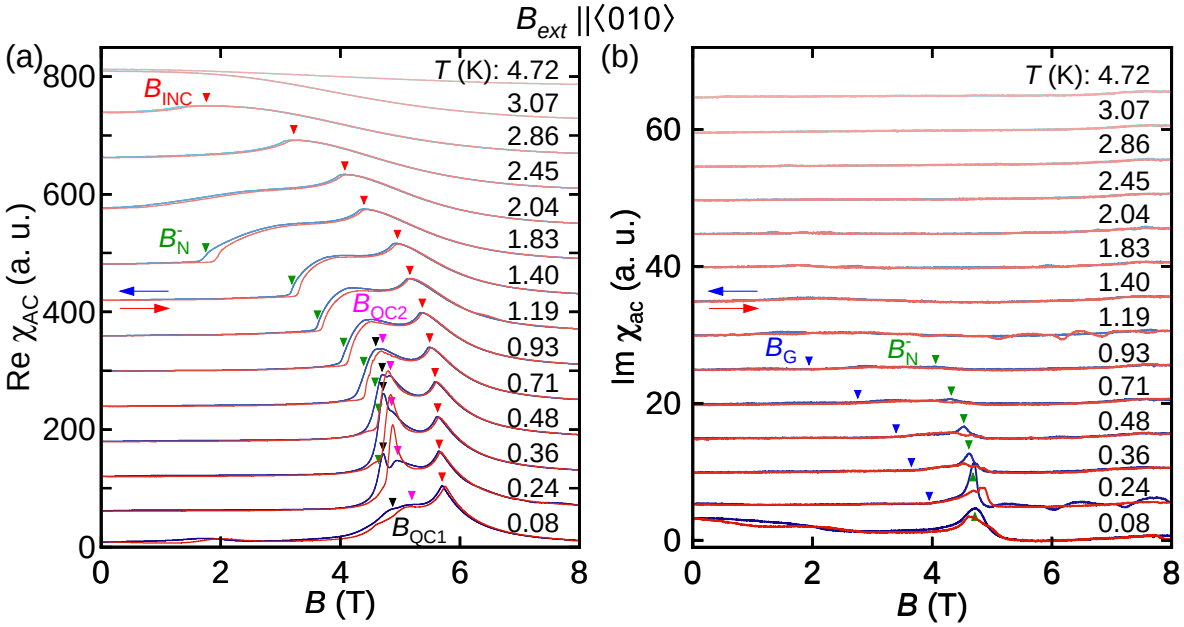

Figure 4.13: Magnetic field dependence of the transverse susceptibility for selected temperatures. The data is plotted with constant offsets. (a) Real part of the transverse susceptibility. (b) Imaginary part of the transverse susceptibility.

Fig. 4.13 (a) displays the magnetic-field dependence of the real part of the transverse susceptibility for fields up to 8 T for a selection of fairly constant temperatures ranging from 4.72 to 0.08 K. A small temperature drift of the bath temperature as shown in Fig. 2.12 (a) resulted from the influence of the magnetic field on the readout of the control thermometer of the dilution insert. The trajectories of the magnetic field sweeps are indicated by the white dotted lines in Fig. 4.11. No signature is detected in the

Transition field	Signature	Color
B_{N}^{-}	point of inflection extracted from zero crossing of the second derivative of the real part of $\mathrm{Re}(\chi_{\mathrm{ac}}^{\perp})$	green
B_{INC}	maximum in $\mathrm{Re}(\chi_{\mathrm{ac}}^{\perp})$	red
B_{QC1}	maximum/shoulder in $\mathrm{Re}(\chi_{\mathrm{ac}}^{\perp})$	black
B_{QC2}	maximum/shoulder in $\mathrm{Re}(\chi_{\mathrm{ac}}^{\perp})$	magenta
B_{G}	onset of increase of $\mathrm{Im}(\chi_{\mathrm{ac}}^{\perp})$	blue

Table 3: Overview of the signatures attributed to different phase transitions in the magnetic field dependence of the transverse susceptibility for perfect transverse-field orientation in Fig. 4.13

magnetic field dependence for temperatures above 2.86 K. At 2.86 K, a maximum emerges at $B_{\mathrm{INC}} = 1.77\,\mathrm{T}$, indicating the incommensurate to paramagnetic transition. As the temperature decreases, the maximum at the magnetic field B_{INC} shifts to higher magnetic fields, becomes sharper and converges towards $B_{\mathrm{INC}} = 5.7\,\mathrm{T}$ at 80 mK, which is the lowest temperature measured.

By comparing the temperature dependence of the transverse susceptibility in Fig. 4.12 with the magnetic-field dependence in Fig. 4.13 (a), an additional signature can be identified as the point of inflection (green triangles) at a temperature of 1.83 K and a magnetic field of $B_{\mathrm{N}}^{-} = 1.75\,\mathrm{T}$. This point of inflection can be associated with the incommensurate to commensurate antiferromagnetic phase transition and the transition field B_{N} exhibits a hysteretic behavior depending on the sweep direction. As the temperature decreases, the point of inflection at the magnetic field B_{N}^{-} approaches 4.65 T at 240 mK and then decreases to 4.4 T at 137 mK. At 80 mK, the signature is not distinct enough to be further tracked.

Below 710 mK, two additional signatures emerge: two maxima at the fields $B_{\mathrm{QC1}}^{-} = 4.59\,\mathrm{T}$ and $B_{\mathrm{QC2}}^{-} = 4.71\,\mathrm{T}$ for the decreasing field sweep and a maximum and a shoulder for the increasing field sweep. These maxima and shoulder might be connected to the presence of additional phase pockets at low temperatures. Theoretical predictions suggest the existence of additional phases at zero temperature due to isosceles distortions of the antiferromagnetic inter-chain couplings of Ising chains [105].

Fig. 4.13 (b) shows the magnetic field dependence of the imaginary part of the transverse susceptibility up to 8 T for fairly constant temperatures ranging from 4.72 K to 0.08 K. The imaginary part of the susceptibility does not exhibit any signatures for temperatures above approximately 1 K.

At temperatures below 930 mK, a small maximum emerges at $B_{\mathrm{N}}^{-} = 4.05\,\mathrm{T}$, becoming more prominent as the temperature decreases further. The evolution of this maximum

at the critical field B_N^- corresponds well with the evolution of the position of the critical fields of the incommensurate to commensurate antiferromagnetic transition in the magnetic phase diagram extracted from the real part of the susceptibility. The broadening and increase of this maximum at very low temperatures may suggest the presence of additional phases in the vicinity of the incommensurate to commensurate antiferromagnetic transition.

Furthermore, the onset of a step-like signature can be observed at very low temperatures below 1 K, barely visible at 930 mK and at $B_G = 1.94\,T$ marked with a blue triangle, but increasingly prominent towards lower temperatures. This onset of the increase of the imaginary part of the susceptibility at B_G matches well with the phase boundary of a glassy phase reported in Ref. [35] within the ordered phase regime. However, no indications of the glassy regime in the paramagnetic phase as reported in this publication could be found in this susceptibility measurement. The increase of the imaginary part of the susceptibility at 80 mK and at magnetic fields below 2 T remains unexplained.

An overview of all signatures tracked in the magnetic field dependence of the transverse susceptibility can be found in table 3.

4.5.2 Effects of Misalignment on the Transverse Susceptibility

As demonstrated for instance by Wendl et al. in their study on the influence of longitudinal magnetic field components on the transverse-field quantum phase transition in the 3D-Ising compound $LiHoF_4$ [31], an intentional misalignment of the magnetic field can be crucial in comprehending the nature of quantum phase transitions. Compared to $LiHoF_4$, which has a hard plane anisotropy, $CoNb_2O_6$ has only one hard axis. This results in a much larger parameter space when studying the effects of an intentional misalignment of the magnetic field. To narrow the parameter space of misalignment angles down in this work on $CoNb_2O_6$, the focus was on an intentional misalignment from the $\langle 010 \rangle$ direction towards the $\langle 001 \rangle$ direction by approximately 0.9°. This defined misalignment angle can be realized in analogy to Fig. 2.14 (c), when the magnetic field is perpendicular to the $\langle 100 \rangle$ direction.

Fig. 4.14 presents the magnetic phase diagram, when the misaligned angle of 0.9° is introduced between the magnetic field and the $\langle 010 \rangle$ direction. The phase boundaries T_N and T_{INC} behave similarly for small magnetic fields below 2 T when compared to the perfect transverse orientation, cf. Fig. 4.11. Between 2 T and 3 T and between 2 K and 3 K, additional maxima are observed in the transverse susceptibility indicating the

presence of an emergent phase transition as a result of the introduction of longitudinal field components.

The top scale in Fig. 4.14 shows the strength of the magnetic field projected on the ⟨001⟩ direction. On this scale the transition field of the emergent phase transition at B_{SF} is of a similar size as the transition field of the spin flip transition at B_{SF1} or $B_{FR} \approx 40\,\mathrm{mT}$ in Fig. 4.4 (c) observed in the literature for a magnetic field parallel to the ⟨001⟩ direction [115, 117, 143]. The similarity between the transition fields suggests, that the emergent phase under a misaligned magnetic field might be associated with the spin-flip or ferrimagnetic phase known from the *c*-axis phase diagram.

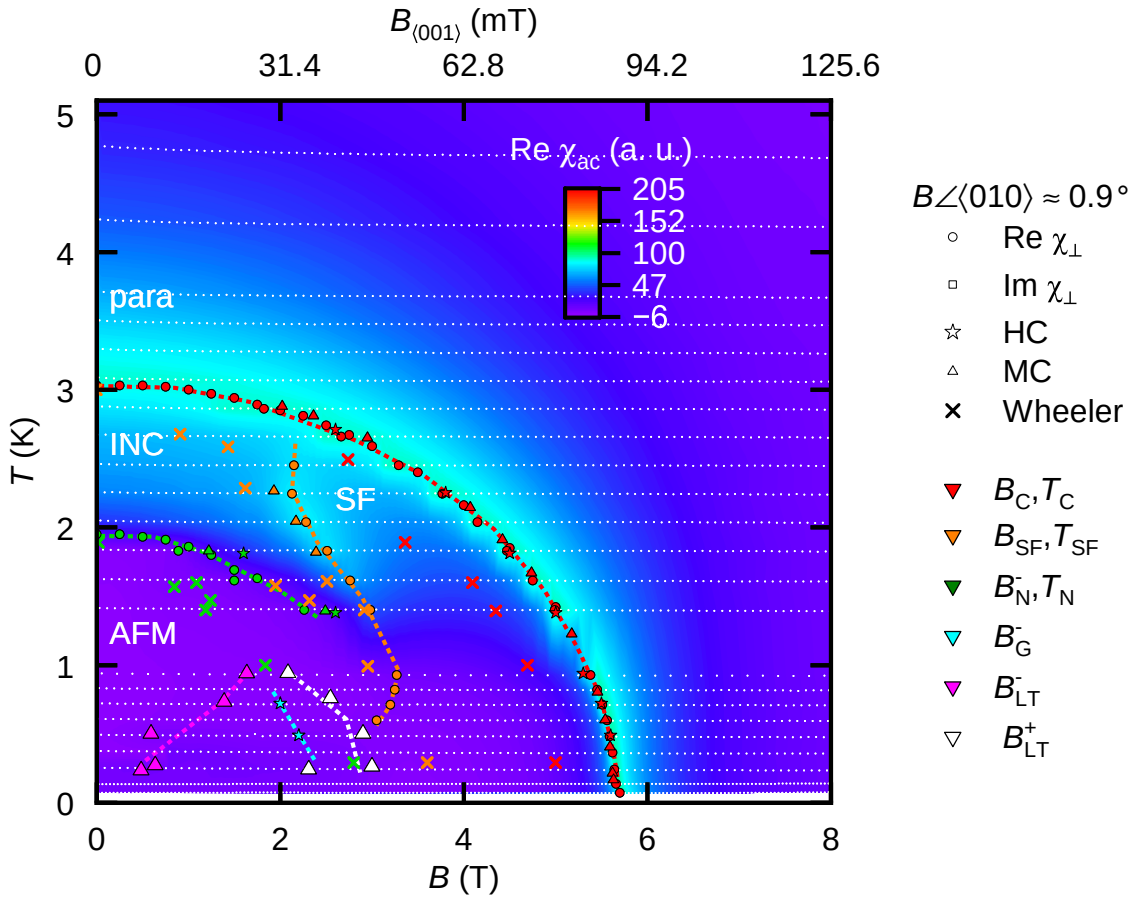

Figure 4.14: 2D color plot of the transverse susceptibility as a function of temperature and transverse magnetic field with a small misalignment. Data points were inferred from measurements of the transverse susceptibility, the heat capacity (HC), and the magnetocaloric effect (MC). White dots indicate the position of the recorded magnetic field sweeps. Data points of the phase diagram from the doctoral thesis of E. Wheeler [35] are also included. The top scale shows the projection of the magnetic field on the ⟨001⟩ direction due to misalignment.

As the temperature decreases further, below 1 K the maximum at B_{SF} turns into a shoul-

der and gradually becomes less prominent before disappearing entirely below 500 mK. At lowest temperatures, the point of inflection at B_N^- has vanished as well in the transverse susceptibility and consequently only the maximum at B_{INC} can be tracked. Additionally, signatures in the heat capacity and the magnetocaloric effect were observed below 1 K. In the following, the temperature and magnetic field dependence of the transverse susceptibility will be focused in more detail.

Fig. 4.15 shows the temperature and magnetic field dependence of the transverse susceptibility under a slightly misaligned magnetic field. In the measurement of the temperature dependence for constant magnetic fields in Fig. 4.15 (a), the evolution of the two signatures known from zero field at T_C and T_N indicating the two phase transitions (red and green triangles) with increasing field is akin to that under perfect transverse-field orientation of the magnetic field. However, at a temperature of $T_{SF} = 1.93$ K and at a magnetic field of 2.5 T, a small hump emerges (orange triangle) that could indicate the emergence of an additional transition.

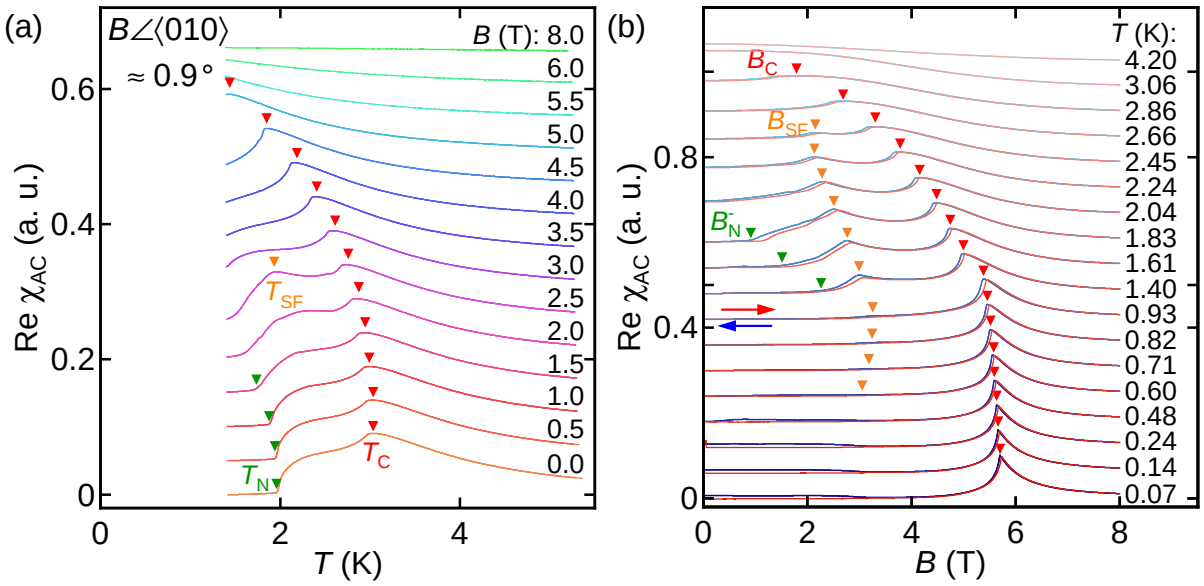

Figure 4.15: Temperature and magnetic field dependence of the transverse susceptibility for a magnetic field slightly canted away from the hard axis ⟨010⟩. The data is plotted with constant offsets. (a) Temperature dependence of the real part of the transverse susceptibility. (b) Magnetic field dependence of the real part of the transverse susceptibility.

In the magnetic field dependence at fairly constant temperatures in 4.15 (b), for both increasing and decreasing magnetic fields, a distinct hump is observed. This provides strong indications of an additional phase pocket starting at temperatures below 2.45 K and at a magnetic field of $B_{SF} = 2.15$ T. In 4.15 (b), the hump at B_{SF} shifts to slightly

Transition parameter	Signature	Color
T_N	point of inflection extracted from zero crossing of the second derivative of the real part of $\mathrm{Re}(\chi_{ac}^{\perp})$	green
T_C	global maximum in $\mathrm{Re}(\chi_{ac}^{\perp})$	red
T_{SF}	local maximum in $\mathrm{Re}(\chi_{ac}^{\perp})$	orange
B_N^-	point of inflection extracted from zero crossing of the second derivative of $\mathrm{Re}(\chi_{ac}^{\perp})$	green
B_C	maximum in $\mathrm{Re}(\chi_{ac}^{\perp})$	red
B_{SF}	maximum/shoulder in $\mathrm{Re}(\chi_{ac}^{\perp})$	orange

Table 4: Overview of the signatures attributed to different phase transitions in the magnetic field and temperature dependence of the transverse susceptibility for intentionally tilted magnetic field orientation in Fig. 4.15

higher magnetic fields as the temperature decreases. Below 930 mK, the magnetic-field shift of B_{SF} reverses and instead shifts to slightly smaller magnetic fields before the hump disappears at 480 mK.

At temperatures below 600 mK, only the maximum indicating the transition between the paramagnetic and an ordered magnetic phase is observed. This is in contrast to the measurement with a perfect magnetic field alignment shown in Fig. 4.18. At temperatures below 240 mK, a hysteretic behavior of the susceptibility between the up- and the downsweep can be observed for magnetic fields below 3 T. A similar hysteretic behavior at very low temperature for a field parallel to the magnetically easy $\langle 001 \rangle$ direction was observed in the literature [132, 143].

Table 4 provides an overview of all signatures observed in Fig. 4.15.

4.5.3 Heat Capacity in Transverse Magnetic Fields

Heat capacity measurements play a key role in obtaining a better understanding of the fundamentals of the nature of phase transitions and the underlying physics of a system. Studies on the calorimetric properties of $CoNb_2O_6$ have primarily focused on its zero-field behavior and the effect of a magnetic field parallel to the $\langle 100 \rangle$ direction [42, 125].

Published experimental results for a magnetic field applied parallel to the $\langle 010 \rangle$ direction recorded using an AC calorimetry method show surprising features such as a prominent peak in C/T at the quantum critical point [35]. This peak is explained by the presence of gapless excitations . However, the presented phase diagram in this publication is lacking detailed information of the exact extend of the different magnetic phases. In particular, the incommensurate to commensurate antiferromagnetic transition known to be present

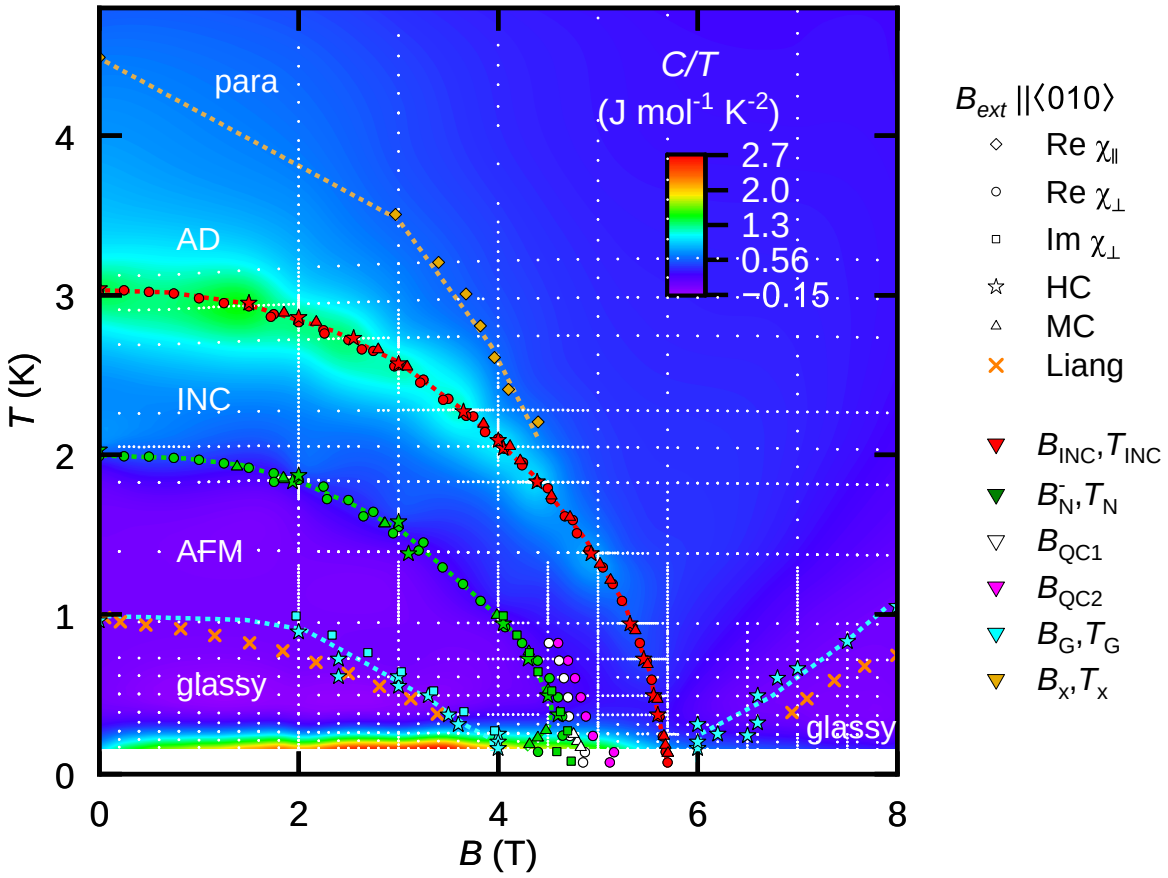

Figure 4.16: 2D color plot of C/T as a function of temperature and transverse magnetic field. Data points were inferred from measurements of the longitudinal and transverse susceptibility, the heat capacity (HC), and the magnetocaloric effect (MC). White dots indicate the position of the recorded heat pulses. Data points of the glassy regime from Liang et al. [35] are also included.

at $T_N \approx 2\,K$ in zero field is ambiguous in the data. Hence, this phase boundary was not inferred from the data in this publication.

This section presents extensive specific heat data for magnetic field parallel to the magnetically hard ⟨010⟩ direction. The magnetic field was orientated using the same process as described in section 2.4. Instead of the transverse susceptibility, the magnetocaloric effect was measured for the process of aligning the magnetic field. Fig. 4.16 shows the transverse field magnetic phase diagram from Fig. 4.11, but with a 2D color plot of C/T underlying the data points. Small white dots indicate the position of the recorded heat pulses.

A large specific heat signal was found in the vicinity of $T_{INC} = 3.04\,K$ at zero magnetic field. With increasing magnetic field, the signal around T_{INC} becomes progressively

Transition temperature	Signature	Color
T_N	maximum in C	green
T_{INC}	maximum in C	red
T_G	onset of a rising coupling parameter τ_2 extracted from the heat capacity fit (see Fig. 4.26)	blue

Table 5: Overview of the signatures attributed to different phase transitions in the temperature dependence of the heat capacity for perfect transverse field orientation in Fig. 4.17

smaller.

For temperatures below T_N, the specific heat becomes very small, as indicated by the purple shading. Towards the lowest temperatures below 300 mK and magnetic fields below 5 T, however, an increasingly enhanced signal of unknown origin is observed. In the same region of the phase diagram, an enhanced signal in the imaginary part of the transverse susceptibility was observed as shown in Fig. 4.11 (b). Two regimes with unusual thermal relaxation were also identified by the heat pulse method used here. The details of these so-called glassy regimes are described in section 4.5.7. In the following, the temperature and magnetic field dependence of the specific heat is described in more detail.

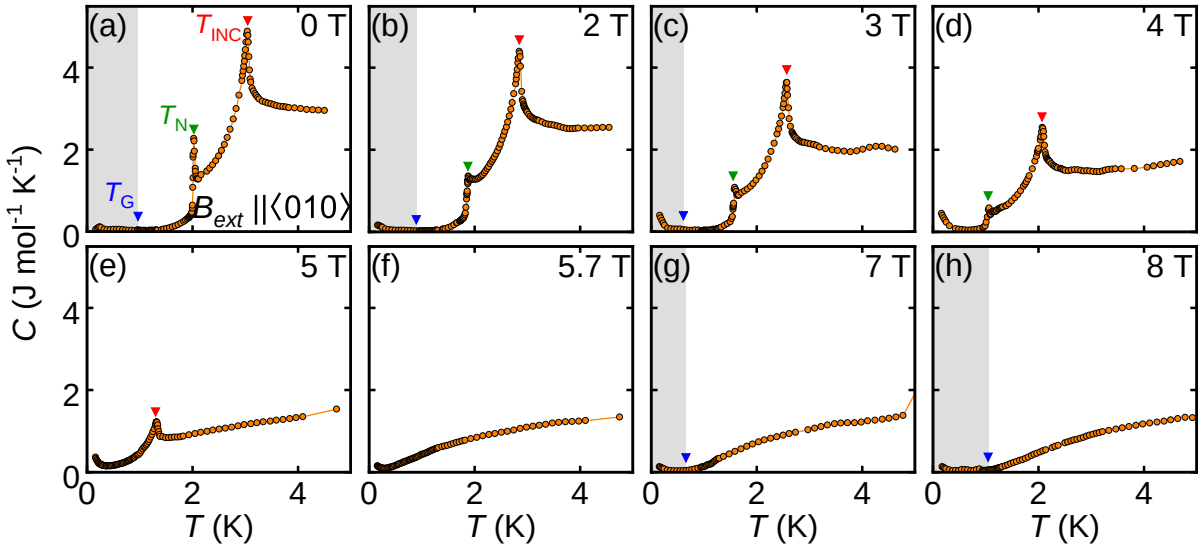

Figure 4.17: Temperature dependence of the specific heat for different transverse magnetic fields between 0 T and 8 T parallel to the ⟨010⟩. The gray shading area marks regions with anomalous thermal relaxation impeding the fit of the heat pulse.

Fig. 4.17 shows the temperature dependence of the specific heat between temperatures of 160 mK and 5 K for a selection of constant magnetic fields up to 8 T. The gray shading marks regions of anomalous thermal relaxations as described in section 4.5.7. In Fig.

Transition field	Signature	Color
B_{N}^{-}	maximum/shoulder in C	green
B_{INC}	maximum in C	red
B_{G}	shoulder in C and onset of a rising coupling parameter τ_2 extracted from the heat capacity fit (see Fig. 4.27)	blue

Table 6: Overview of the signatures attributed to different phase transitions in the magnetic field dependence of the heat capacity for perfect transverse field orientation in Fig. 4.18

4.17 (a), the specific heat is shown for zero magnetic field. Two prominent peaks at $T_{\mathrm{N}} = 2.03\,\mathrm{K}$ and at $T_{\mathrm{INC}} = 3.04\,\mathrm{K}$ indicate the transition temperatures in zero magnetic field of the incommensurate (INC) to commensurate antiferromagnetic (AFM) transition and of the incommensurate (INC) to paramagnetic (para) transition, respectively. With increasing magnetic field, both peaks become smaller and shift to lower temperatures. At a magnetic field of 5 T as shown in Fig. 4.17 (e), only one peak remains at $T_{\mathrm{INC}} = 1.32\,\mathrm{K}$. For magnetic fields of 5.7 T and larger in Figs. 4.17 (f)-(h) no discernible signature is observed.

The gray shaded area marks the glassy regime. In this region, the fit did not work reliably due to a non-trivial thermal relaxation of the sample. Therefore, the data points in this region need to be treated with caution. The temperature T_{G} marking the boundary of this regime was extracted from the parameter τ_2, which usually serves as a measure for the thermal coupling of the sample to the platform and is derived from the fit of the heat pulse. However, in these regions, a large value of τ_2 results from an inadequate model for the fit. More details can be found in section 4.5.7.

At zero magnetic field in Fig. 4.17 (a), T_{G} was found to be 0.96 K, in good agreement with similar effects observed in the literature [35, 42]. With increasing magnetic field, T_{G} shifts to lower temperatures. Between 4 T and 5.7 T, the thermal relaxation was observed to behave normally over the entire temperature range, as shown in Fig. 4.17 (d)-(f). At 7 T, non-exponential thermal relaxation was observed below $T_{\mathrm{G}} = 0.66\,\mathrm{K}$. As the magnetic field was further increased, T_{G} was observed to shift to higher temperatures. At temperatures below 1 K, small anomalous increases of the specific heat with decreasing temperature were observed for all measured fields. However, the data are only reliable for magnetic fields between 4 T and 6 T at milli-Kelvin temperatures because the glassy behavior of the thermal properties of the sample massively impedes the heat capacity measurements. Further investigation is required to determine the origin of these anomalous increases.

Fig. 4.18 presents recorded specific heat data as a function of magnetic field for decreasing and increasing fields between 0 T and 8 T and for a selection of fairly constant

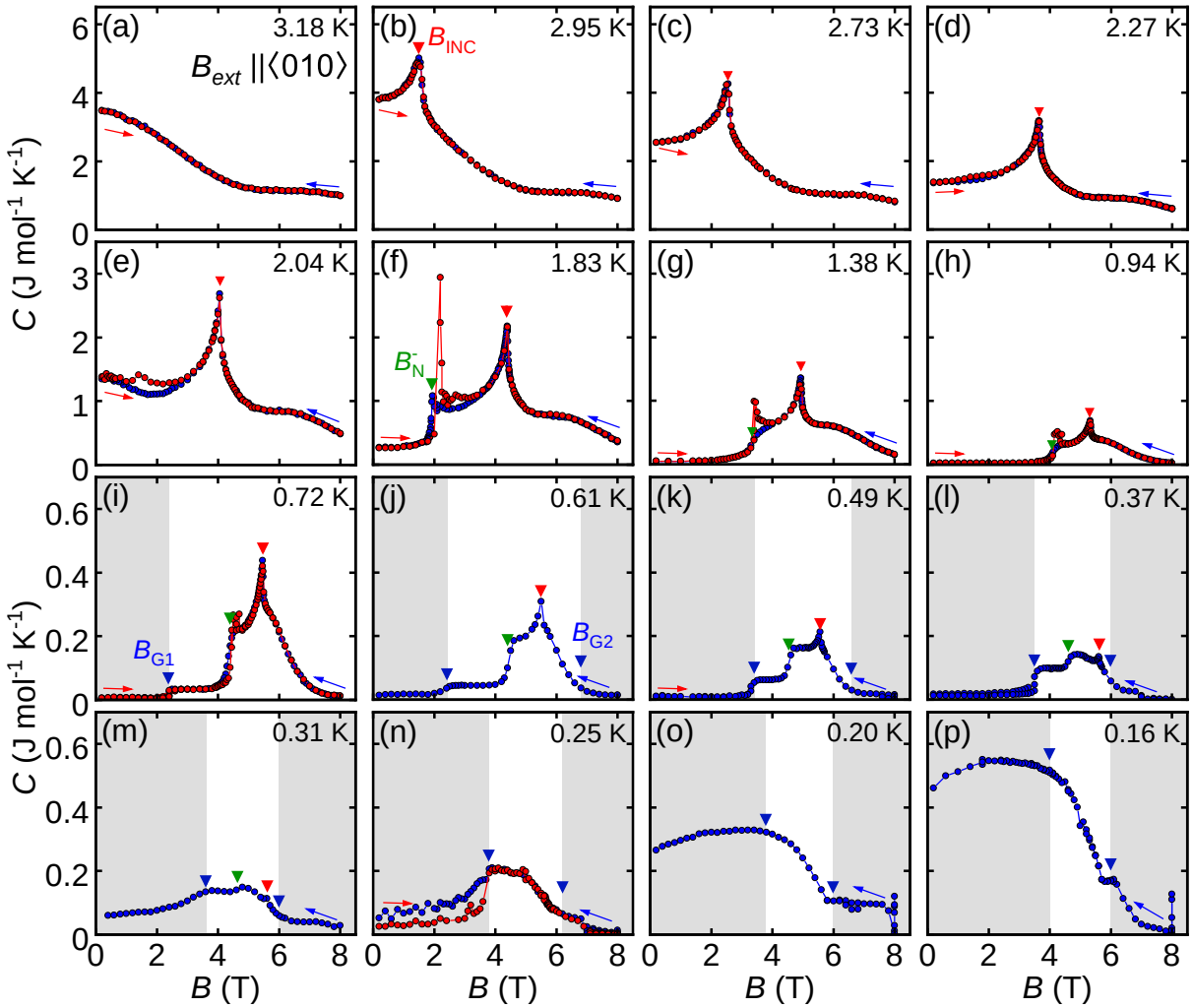

Figure 4.18: Magnetic field dependence of the specific heat for different temperatures. The gray shaded area marks the glassy regimes with anomalous thermal relaxation. In these regimes, the data points need to be treated with caution. The glassy regime is addressed in a later section.

temperatures between 160 mK and 3.18 K.

Starting from a temperature of 3.18 K in Fig. 4.18 (a), no distinct signature is observed. However, worth mentioning is the tail in the specific heat at magnetic fields above 5 T, where the specific heat does not continuously go down to zero with increasing magnetic field, but rather remains constant between 5 T and 7 T. Clear indications of such a plateau are found down to 720 mK. These plateaus may be associated with the plateaus in the temperature dependence of the heat capacity in Fig. 4.17 observed in the paramagnetic phase for temperatures larger T_{INC}. At temperatures below 310 mK, plateaus are observed, but superimposed with the region of anomalous thermal relaxation. Hence, these data points need to be treated with caution. At 2.95 K in Fig. 4.18 (b), a prominent peak

at B_{INC} =1.5 T marks the transition between the paramagnetic and the incommensurate phase. As the temperature decreases, the peak at B_{INC} becomes smaller and continuously shifts to higher magnetic fields.

At 2.04 K in Fig. 4.18 (e), a hysteretic behavior between 1 T and 2 T is observed. As the temperature is further decreased, the hysteretic behavior of the heat capacity becomes characteristic for the transition between the incommensurate and the commensurate antiferromagnetic phase (INC-C-AFM). As can be seen in Fig. 4.18 (f), when the magnetic field is ramped up, a large peak in the heat capacity is observed at $B_N^+ = 2.2$ T. For decreasing fields, a shoulder is observed at the transition field of $B_N^- = 1.94$ T, which becomes smoother as the temperature decreases. The signatures at B_N^+ marking the INC-C-AFM transition shift to higher magnetic fields with decreasing temperature.

An additional step-like signature emerges at 720 mK at $B_{G1} = 2.4$ T marked with a blue triangle in Fig. 4.18 (i). With decreasing temperature, this signature moves to higher magnetic fields. For magnetic fields below this signature at B_{G1}, the thermal relaxation method used was compromised due to the anomalous behavior of the thermal relaxation. Therefore, the data points in this gray shaded region are not reliable. Nevertheless, the evolution of the signature fits well with the glassy or freezing behavior mentioned in Refs. [35, 42].

At temperatures below 310 mK, the field dependence of the specific heat changes drastically, exhibiting a broad feature between 0 T and 6 T, that becomes increasingly prominent as the temperature decreases, as shown in Fig. 4.18 (m). At 160 mK in Fig. 4.18 (p), this signature dominates the specific heat.

Starting at 610 mK in Fig. 4.18 (j), a blue triangle and the gray shaded area on the right side indicate a second regime with an anomalous thermal relaxation resulting in unreliable data points. The transition field B_{G2} was extracted from τ_2, a time constant that describes the thermal coupling of the sample and is obtained from a fit to the heat pulse. Details on the evaluation of τ_2 are described in section 4.5.7.

At 160 mk in Fig. 4.18 (p), there is also a step-like signature at 6 T. This signature is also connected to the glassy state in the paramagnetic phase presented in Ref. [35], because for higher fields than 6 T at this temperature, the thermal relaxation method was also compromised.

4.5.4 Effects of Misalignment on the Heat Capacity

Fig. 4.19 shows the temperature dependence of the heat capacity in a slightly misaligned magnetic field. The misalignment angle between the magnetic field and the ⟨010⟩ direction was 0.9°. Data points at temperatures between 1 K and 1.4 K where not recorded, because these temperature are outside of the regimes where a DR insert provides stable temperatures without extensive maintenance.

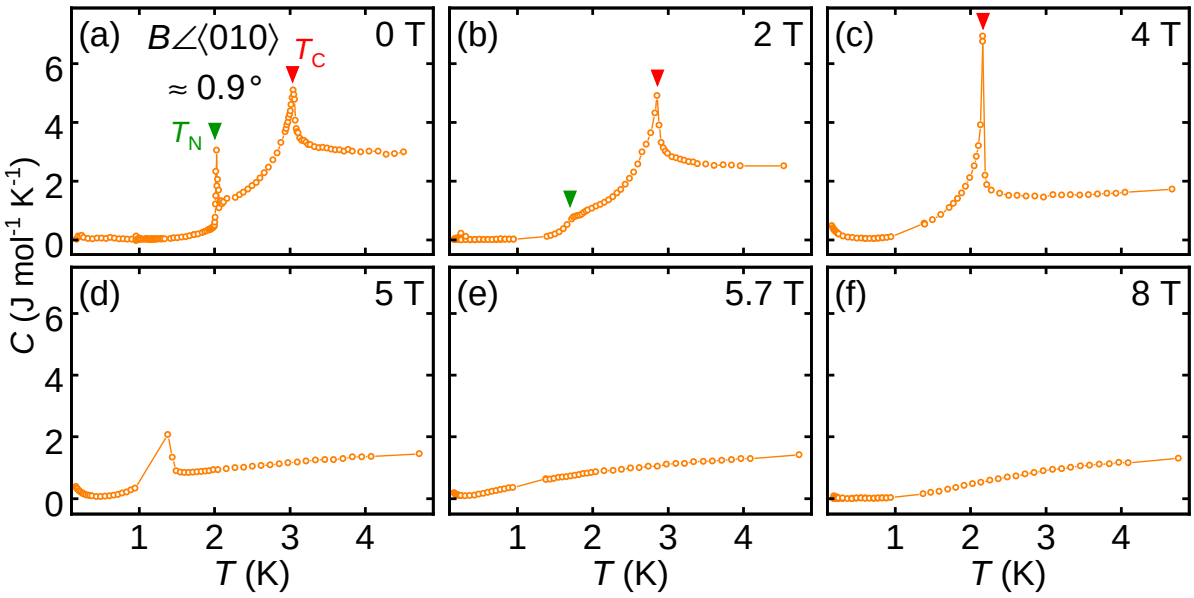

Figure 4.19: Temperature dependence of the specific heat for different constant magnetic fields between 0 T and 8 T with an misalignment angle of 0.9° between the b axis and the direction of the magnetic field.

At zero magnetic field, two peaks in the heat capacity are located at $T_N = 2.02\,K$ and at $T_{INC} = 3.04\,K$, as displayed in Fig. 4.19 (a), consistent with the result for a perfect transverse field configuration in Fig. 4.17 (a). For a constant magnetic field of 2 T, the two signatures from zero field have both shifted to lower temperatures and the INC-to-AFM transition at T_N (green triangle) turns from a peak into a less distinct shoulder.

Transition temperature	Signature	Color
T_N	maximum/shoulder in C	green
T_C	maximum in C	red

Table 7: Overview of the signatures attributed to different phase transitions in the temperature dependence of the heat capacity for an intentionally misaligned magnetic field orientation in Fig. 4.19

At 4 T, the peak indicating the INC-to-paramagnetic transition (red triangle) at T_{INC} becomes sharper and larger in size. The INC-to-AFM transition is not visible in the

measured data, as it is presumably in the temperature range between 1 K and 1.4 K. At 5 T, only the start of the upturn of the INC-to-paramagnetic transition is observable, but the majority of the signature is presumably in the region between 1 K and 1.4 K. At 5.7 T and 8 T, no signature is detected.

Table 7 provides an overview of all signatures tracked in the temperature dependence of the heat capacity for a slightly misaligned magnetic field orientation.

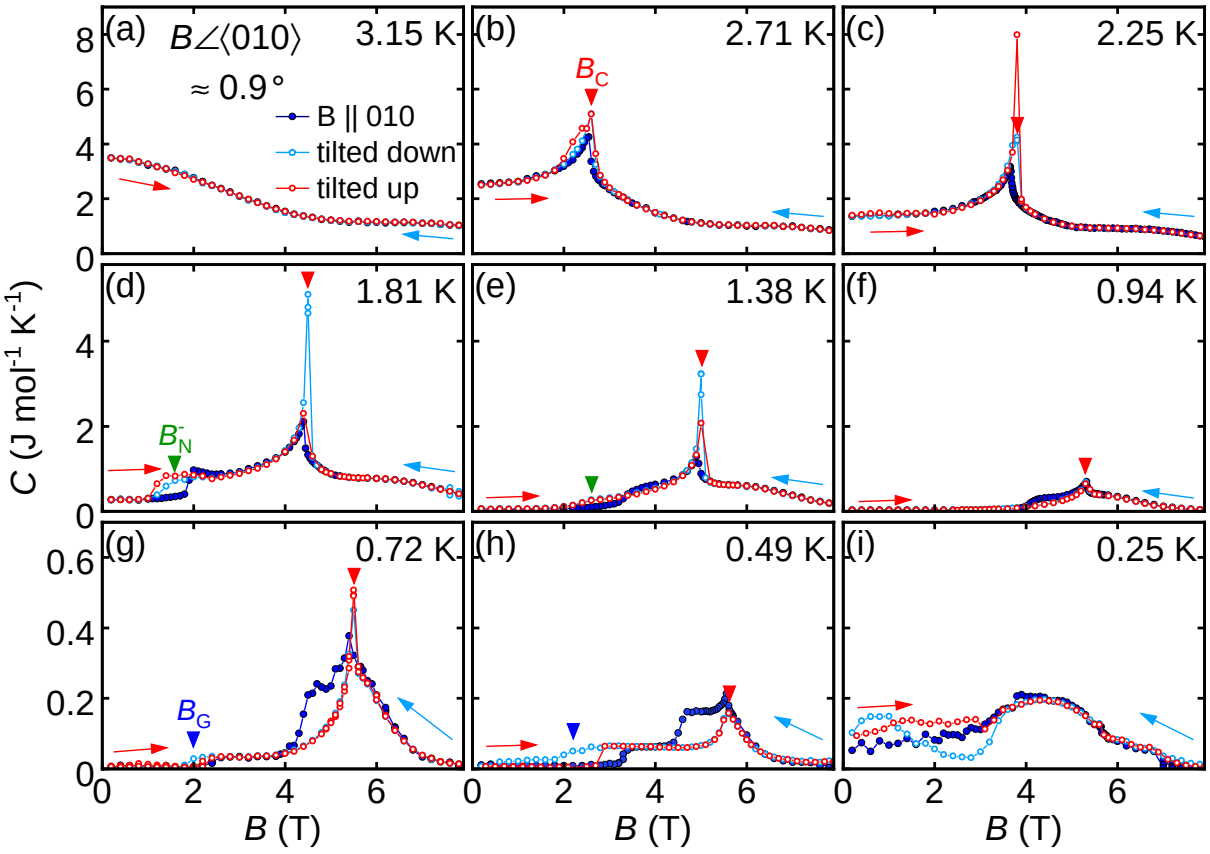

Figure 4.20: Magnetic field dependence of the specific heat for different temperatures in a tilted magnetic field. The angle between the ⟨010⟩ direction and the magnetic field was 0.9°. The heat capacity for decreasing and increasing magnetic field with a misalignment angle is shown with open symbols with blue and red color, respectively. The results of the heat capacity measurement for a perfect transverse field orientation and decreasing magnetic field are plotted for comparison using solid blue symbols.

Fig. 4.20 shows the magnetic-field dependence of the heat capacity in a tilted magnetic field at fairly constant temperatures. For the comparison, the results for a perfect transverse orientation of the magnetic field are shown as well. The curves showing the measured heat capacity for increasing and decreasing tilted magnetic field are plotted with open symbols. The result of the measurement of the heat capacity with perfect transverse field

orientation is plotted with solid symbols.

In the paramagnetic regime at 3.15 K, there is no difference between transverse and tilted orientation. Between 2.71 K and 1.38 K, the peak indicating the INC-to-paramagnetic transition at B_{INC} (red triangle) is always larger and at a higher magnetic field when the magnetic field is slightly misaligned.

The shoulder at B_{N}^{-} indicating the INC-to-AFM transition (green triangle) at temperatures of 1.81 K and 1.38 K, as shown in Figs. 4.20 (d) and (e), is located at lower magnetic fields for the case of a misaligned magnetic field orientation compared to the perfect transverse orientation.

As shown in Figs. 4.20 (g) and (h), at 720 mK and at 490 mK, the shoulder at B_{G} indicating the transition to the glassy state (blue triangle) is located at lower magnetic fields, when the magnetic field is slightly misaligned with respect to the hard magnetic axis of the system. At 250 mK, an additional hump centered around 1 T is observed, when the magnetic field is misaligned and decreasing, as shown in Fig. 4.20 (i). For increasing magnetic field, the heat capacity is larger up to a magnetic field of 4 T compared to the perfect transverse magnetic field orientation.

Table 8 provides an overview of all signatures tracked in the magnetic-field dependence of the heat capacity for a slightly misaligned magnetic field orientation.

Transition field	Signature	Color
B_{N}^{-}	shoulder in the heat capacity	green
B_{C}	maximum in the heat capacity	red
B_{G}	shoulder in the heat capacity	blue

Table 8: Overview of the signatures attributed to different phase transitions observed in the magnetic field dependence of the heat capacity for an intentionally misaligned magnetic field orientation in Fig. 4.20

4.5.5 Magnetocaloric effect and Change of Entropy in Transverse Magnetic Fields

Magnetocaloric measurements provide information about phase transitions and their nature, as well as information about the entropy contained in the magnetic system [33, 49]. For this measurement, the platform temperature was measured while the magnetic field was swept.

Fig. 4.21 shows the magnetocaloric effect for increasing and decreasing magnetic field superimposed on the magnetic phase diagram. The phase diagram was extracted from susceptibility, heat capacity, and magnetocaloric measurements. The blue curve in Fig.

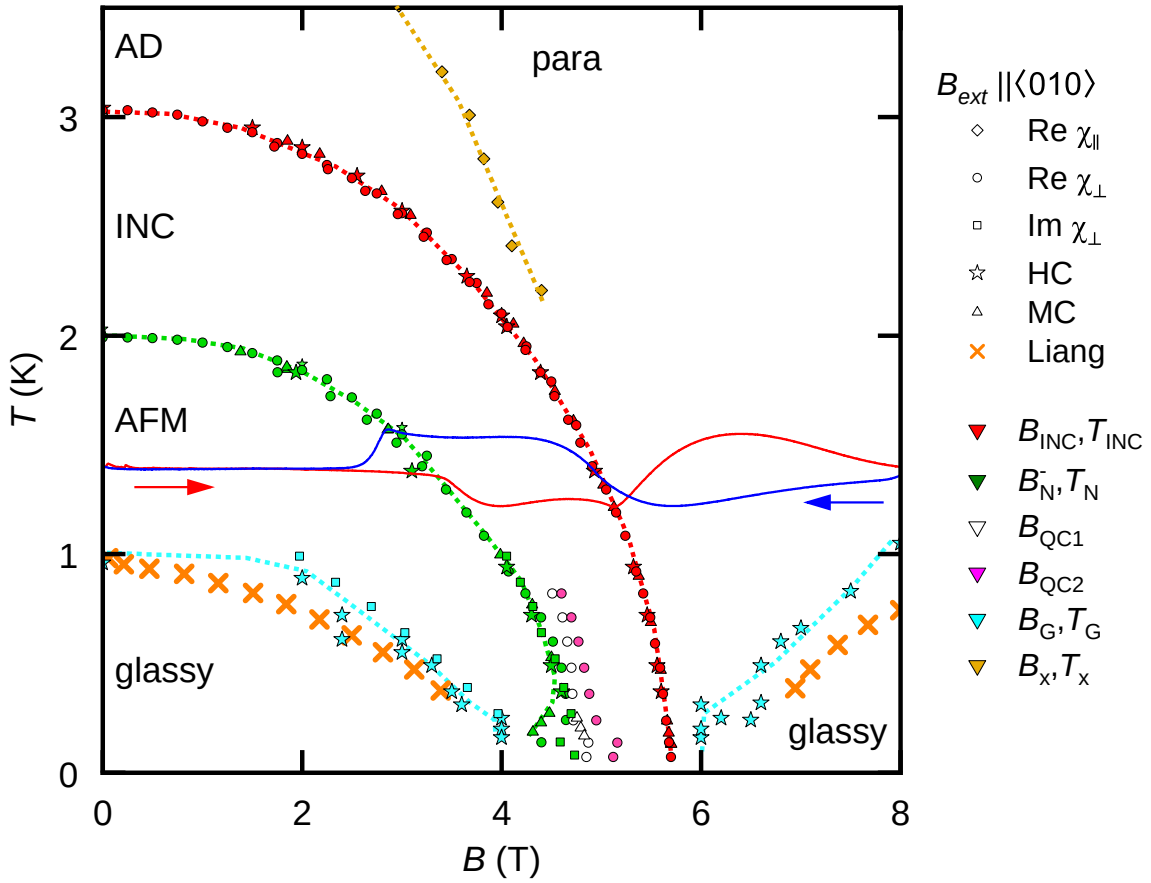

Figure 4.21: Magnetocaloric effect for increasing (red) and decreasing (blue) field values. Data are superimposed on the magnetic phase diagram of $CoNb_2O_6$. Data points of the phase boundaries were inferred from measurements of the longitudinal and transverse susceptibility, the heat capacity (HC), and the magnetocaloric effect (MC).

4.21 represents the temperature variation for a decreasing magnetic field. The maximum near $B_N = 2.84\,T$ and $T_N = 1.57\,K$ in the downsweep corresponds to the incommensurate to antiferromagnetic phase transition. The red curve in Fig. 4.21 displays the temperature variation of the platform for an increasing magnetic field. The minimum at $B_{INC} = 5.14\,T$ and $T_{INC} = 1.22\,K$ in the upsweep corresponds to the paramagnetic to incommensurate transition. In the following, magnetocaloric field sweeps for different bath temperatures are presented and discussed.

B_N^-	shoulder in the magnetic field sweep with negative ramp rate	green
B_{INC}	minimum in the magnetic field sweep with positive ramp rate	red
B_{QC2}^+	minimum in the magnetic field sweep with positive ramp rate	magenta

Table 9: Overview of the signatures attributed to different phase transitions in the magnetocaloric measurements for a perfect transverse field orientation as in Fig. 4.22

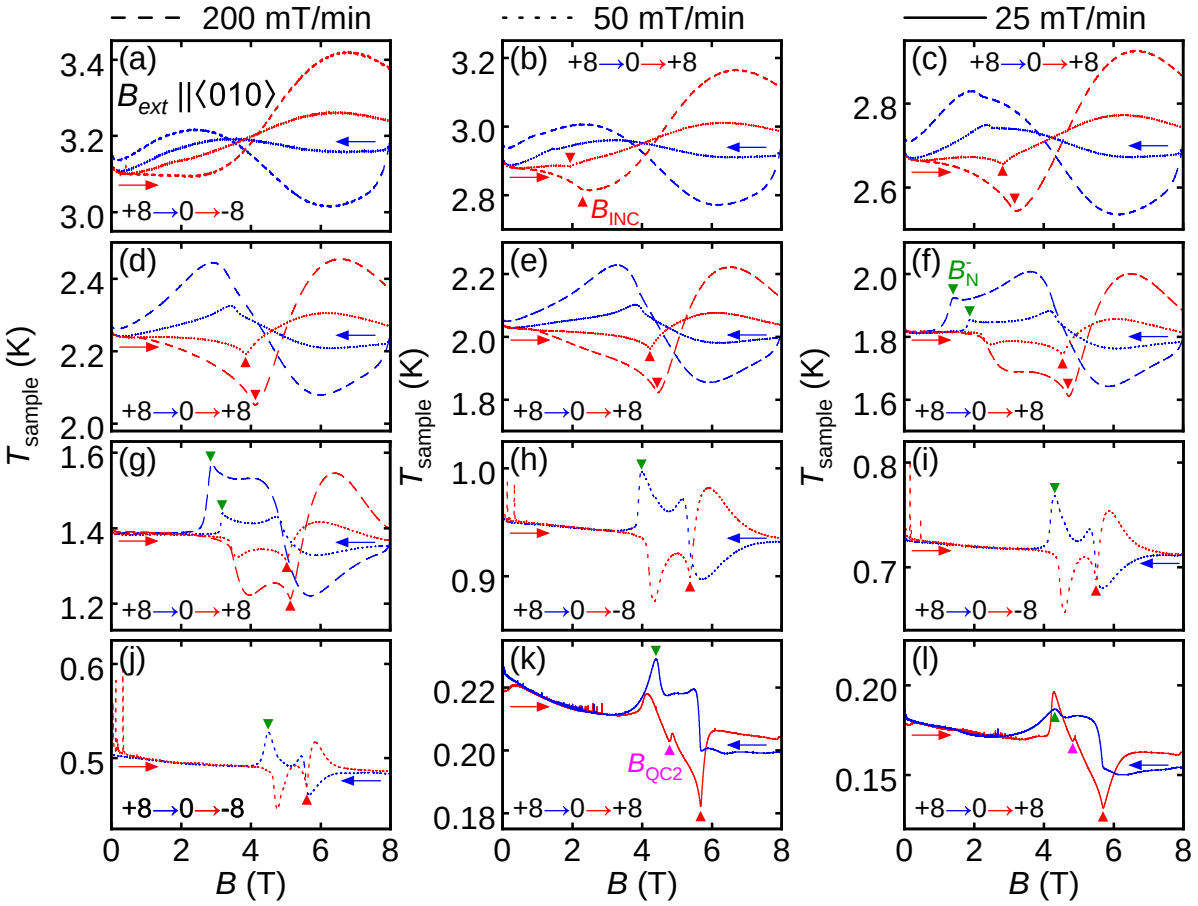

Figure 4.22: Magnetocaloric effect for various bath temperatures for a perfect transverse magnetic field orientation. Triangles highlight the different phase transitions observed. (a)-(g) Sweep rates of 200 mT/min (dashed lines) and 50 mT/min (dotted lines). (h)-(j) Sweep rate of 50 mT/min (dotted lines). (k)-(l) Sweep rate of 25 mT/min (solid lines). In the case of (a), (h)-(j), the magnetic field was inverted between the sweeps with decreasing and increasing field ramps. An inversion of the field after zero crossing lead to flux jumps of the magnet setup between 0 T and 1 T as can be seen in (h)-(j).

Fig. 4.22 shows the temperature variation during a magnetic field sweep for a selection of different base temperatures ranging down to milli-Kelvin temperatures and with different ramp rates. In the case of Figs. 4.22 (a) and (h)-(j) the magnetic field was inverted after the downsweep (+8 T to 0 to -8 T), resulting in undesired temperature spikes at fields below 1 T due to flux jumps of the sample magnet. In the case of Figs. 4.22 (b)-(g) and (k)-(l), the field was not inverted (+8 T to 0 to +8 T) to prevent the temperature spikes. Higher ramp rates lead to larger magnetocaloric variations of the platform temperature. In Fig. 4.22 (a)-(g) magnetocaloric field sweeps are shown with sweep rates of 50 mT/min and 200 mT/min. The magnetocaloric effect in Fig. 4.22 (h)-(j) is recorded with a sweep rate of 50 mT/min while in Fig. 4.22 (k) and (l), the sweep rate was 25 mT/min

No signature in the temperature variation as a function of field is observed above 3 K in the paramagnetic phase, as shown in Fig. 4.22 (a). Below 3 K (starting in Fig. 4.22 (b)) a small kink is observed in the upsweep curve. The kink is marked with a red triangle at fields of B_{INC} =2.32 T for a ramp rate of 200 mT/min and B_{INC} =1.94 T for a ramp rate of 50 mT/min. These kinks in the temperature variations can be attributed to the transition from the paramagnetic the incommensurate state. These kinks transform into a distinct minimum as the temperature decreases and the transition field B_{INC} shifts to larger magnetic fields. The distinct minima observed in the curves with negative ramp rate at the magnetic fields B_{INC} follow the same evolution as was observed in susceptibility and heat capacity measurements.

A signature indicating the transition from paramagnetic to incommensurate is also observed in the curve representing the sweep with a negative ramp rate of the magnetic field. The signature is less prominent for a negative ramp rate, because the red phase boundary at T_{INC}/B_{INC} is crossed more parallel on the trajectory in a phase diagram indicated by the blue line, as shown in Fig. 4.21. A more parallel crossing of a phase boundary results in a smoothing of the signal and consequently less distinct signatures in observed quantities.

In Fig. 4.22 (f), two maxima marked with green triangles at magnetic fields B_N^- =1.41 T for a ramp rate of 200 mT/min and at B_N^- =1.88 T for a ramp rate of 50 mT/min indicate the transition between the incommensurate and the commensurate antiferromagnetic phase. The influence of the INC-to-AFM transition on the temperature variation during a sweep with positive ramp rate is also observed, but it is less pronounced. The evolution of these maxima match well with the transition fields extracted from the susceptibility and heat capacity measurements.

In Figs. 4.22 (f)-(j), the curves with positive and negative ramp rate show continuous evolution of the different signatures, while there is a drastic change in overall behavior between Figs. 4.22 (j) and (k). In Fig. 4.21 (j), when sweeping the magnetic field with a positive ramp rate (red curve), the temperature decreases between 4.2 T and 4.8 T, typically a result of a gain in entropy. In Figs. 4.22 (k) and (l) however, the temperature increases at 3.9 T and 4.1 T, respectively. This may be related to a decrease in entropy for these magnetic fields and temperatures. This change of the overall characteristic of the temperature variation is accompanied by the emergence of a sharp minimum at a magnetic field B_{QC1} = 4.79 T, as shown in Fig. 4.22 (k). However, for negative ramp rates, the overall behavior of the temperature variations towards the lowest temperatures does not change significantly.

The change of entropy within the system for different magnetic fields can be extracted by combining the results of the measurement of the heat capacity and the change of temperature during a magnetic field sweep. The procedure to extract the change of entropy is described in section 2.3.5. To determine the required values of the heat capacity, existing data points were interpolated to create a fine two dimensional grid of C/T as a function of temperature and magnetic field. Fig. 4.16 provides a visualization of the interpolated data set of C/T. By combining the 2D heat capacity grid with the measurement of the magnetocaloric variations of the temperature, the change in entropy was calculated using Eq. 9. The results are shown in Fig. 4.23

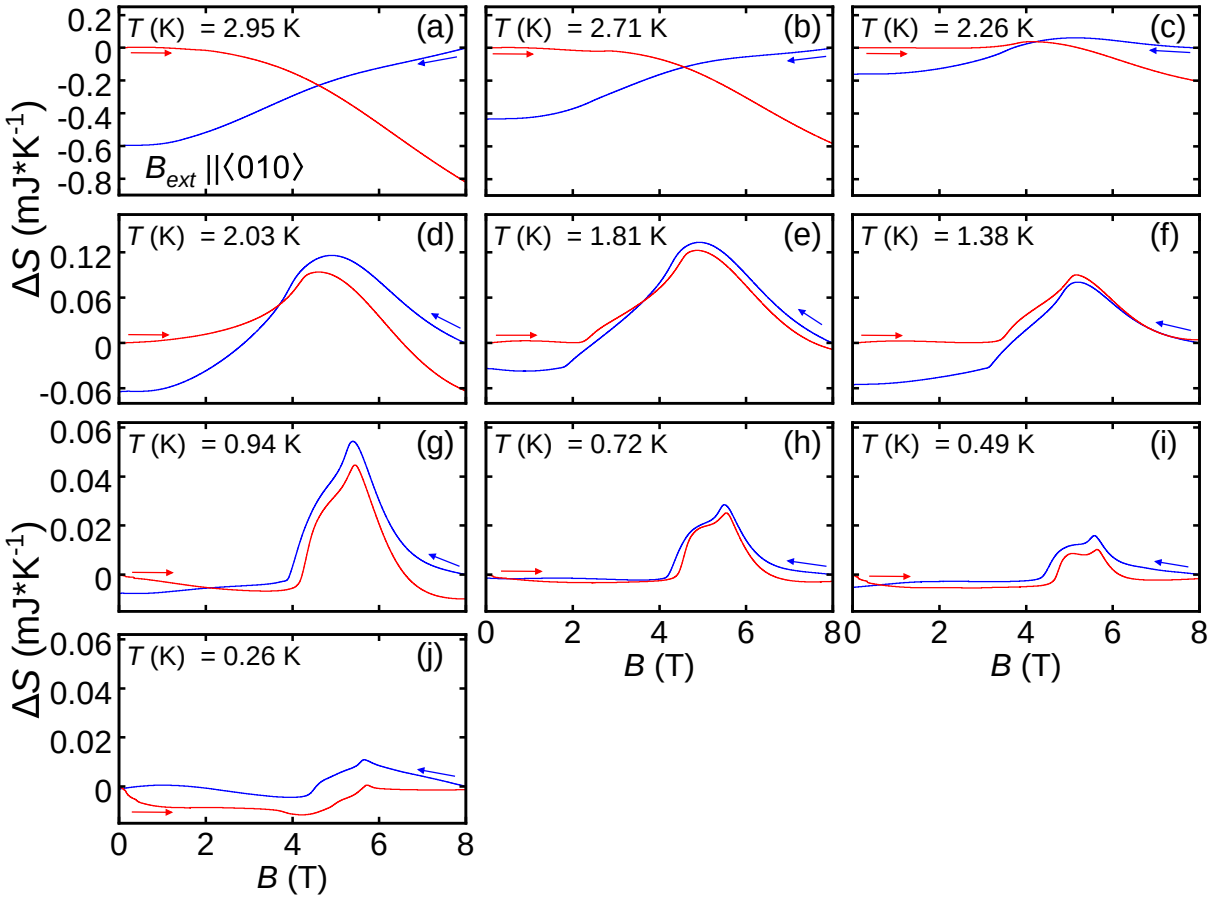

Figure 4.23: The magnetic field dependence of the change of entropy ΔS extracted from the measurement of the magnetocaloric effect and the heat capacity for different bath temperatures. The blue and red curve show the change of entropy extracted from the measurement with decreasing and increasing magnetic field, respectively.

In Fig. 4.23 (a), for the highest temperature of the bath measured, the entropy decreases as the magnetic field is swept in any direction. As the temperature decreases, the change in entropy becomes smaller and a broad maximum emerges starting from 2.26 K at $B =$

4.10 T (see Fig. 4.23 (c)). In addition, a small kink at 2.2 T is observed at a temperature of 1.81 K in Fig. 4.23 (e). This kink indicates the transition between the incommensurate and the commensurate antiferromagnetic phase.

With decreasing temperature, the extracted curves for the positive and negative ramp rate become more congruent. The best congruence is observed at 720 mK in Fig. 4.23 (h). At this temperature the change of entropy shows clear similarities to the temperature dependence of the susceptibility in zero magnetic field when probed along the $\langle 100 \rangle$ direction as shown in Figs. 4.12 and 4.13

4.5.6 Effects of Misalingment on the Magnetocaloric Measurements

Magnetocaloric field sweeps were also investigated for a magnetic field slightly tilted away from the $\langle 010 \rangle$ axis towards the $\langle 001 \rangle$ axis. The misalignment angle was 0.9° between the $\langle 010 \rangle$ axis and the magnetic field direction. This magnetic field orientation is equivalent to the orientation used to study the effects of misalignment on the transverse susceptibility and the heat capacity.

Fig. 4.24 shows the magnetic field dependence of the magnetocaloric temperature variations in a tilted magnetic field for a selection of different temperatures of the thermal bath. The temperature variation with a positive and negative ramp rate of the magnetic field is displayed in red and blue, respectively, across the different panels.

In Fig. 4.24 (a), a downward kink is observed for a positive ramp rate at a magnetic field $B_C = 2.37\,\mathrm{T}$ and a temperature of the sample of $T_C = 2.81\,\mathrm{K}$. This kink is associated with the transition from the paramagnetic phase to an ordered magnetic phase. The kink becomes a distinct minimum as the temperature continues to decreases in Figs. 4.24 (b)-(k). The temperature and magnetic field evolutions agree well with the results for T_C obtained from the measurements of the transverse susceptibility and the heat capacity.

In Fig. 4.24 (c) a small dip in temperature is marked by an orange triangle at $B_{SF} = 1.89\,\mathrm{T}$. This dip indicates an additional transition, that was not present in the measurement with perfect transverse orientation of the magnetic field in Fig. 4.22. In Figs. 4.24 (d) and (e), this dip is more pronounced, but shifts only slightly in magnetic field. In Figs. 4.24 (f)-(k), this dip in temperature is not longer observed.

In Fig. 4.24 (e), an additional shoulder at $B_N^- = 1.13\,\mathrm{T}$ marked by a green triangle in the temperature variation for negative ramp rate of the magnetic field. This shoulder indicates the transition to the commensurate antiferromagnetic phase. In Fig. 4.24 (f) the

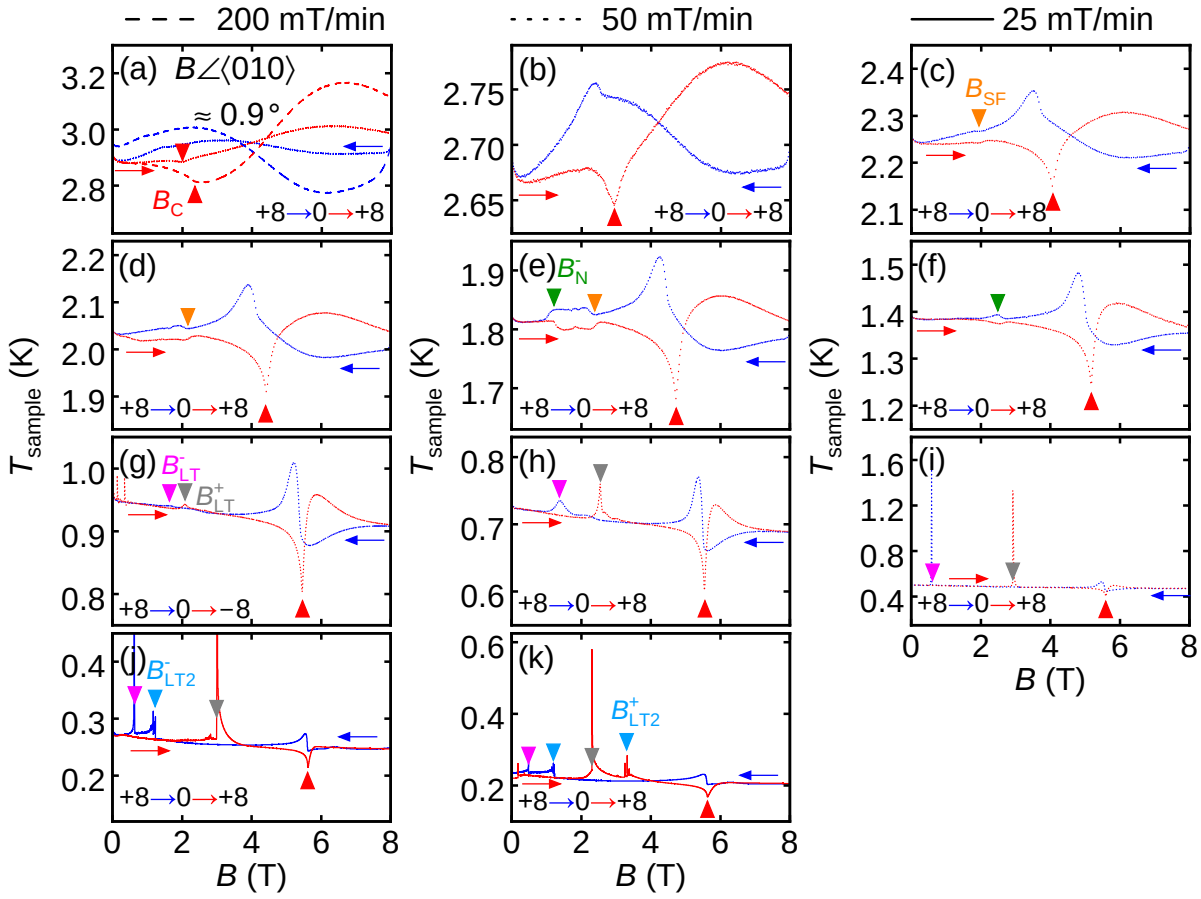

Figure 4.24: Magnetic Field dependence of the magnetocaloric temperature variations for different fairly constant bath temperatures under a slightly misaligned magnetic field with a misalignment angle of 0.9°. The magnetocaloric effect was measured for magnetic field sweep rates of 200 mT/min (dashed lines), 50 mT/min (dotted lines), and 25 mT/min (solid lines) and for increasing and decreasing magnetic fields.

shoulder has turned into a maximum at $B_N^- = 2.36$ T. However, there is no corresponding signature in Figs. 4.24 (g)-(k).

Transition field	signature	color
B_N^-	shoulder in the magnetocaloric effect with negative ramp rate	green
B_{SF}^-	dip in the magnetocaloric effect with negative ramp rate	orange
B_C	minimum in the magnetocaloric effect with positive ramp rate	red
B_{LT}^-	maximum/spike in the magnetocaloric effect with negative ramp rate	magenta
B_{LT}^+	maximum/spike in the magnetocaloric effect with positive ramp rate	gray
B_{LT2}	maximum/spike in the magnetocaloric effect	blue

Table 10: Overview of the signatures attributed to different phase transitions in the magnetocaloric measurements for a misaligned magnetic field as in Fig. 4.24

In Fig. 4.24 (g), at $B_{\mathrm{LT}}^{-} = 1.66\,\mathrm{T}$ and $B_{\mathrm{LT}}^{+} = 2.08\,\mathrm{T}$ maxima are observed under negative and positive ramp rate, respectively. As the temperature decreases, as shown in Figs. 4.24 (h)-(i), the two peaks shift away from each other and become delta-like temperature spikes, indicating a hysteretic first-order phase transition. Hysteretic phase boundaries have also been observed in the literature at temperatures below 1 K for magnetic field applied along the magnetically easy ⟨001⟩ direction [132, 143].

At the lowest temperatures measured in Fig. 4.24 (j) and (k), additional peaks in the temperature variation of the sample are marked with blue triangles. These peaks are observed at $B_{\mathrm{LT2}}^{-} = 1.2\,\mathrm{T}$ for a negative ramp rate of the magnetic field in Fig. 4.24 (j) and (k) and for a positive ramp rate at $B_{\mathrm{LT2}}^{+} = 3.2\,\mathrm{T}$ only at the lowest temperature shown in Fig. 4.24 (j). The origin of these peaks requires further investigation.

4.5.7 Anomalous Thermal Relaxation in Heat Capacity Measurements

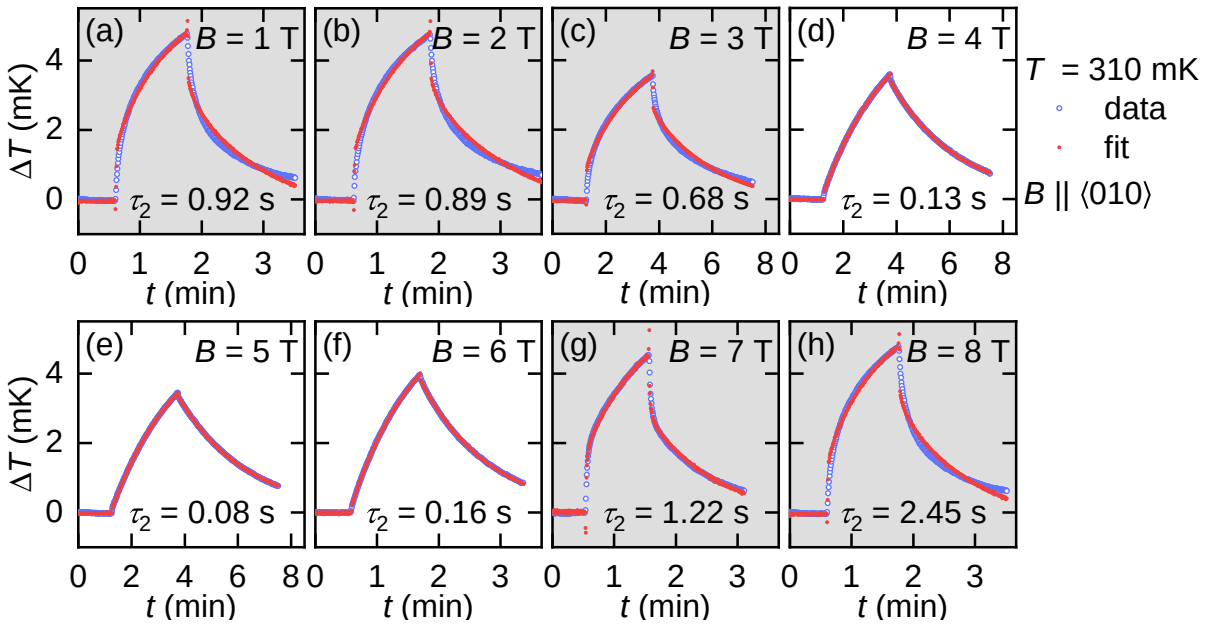

Figure 4.25: Heat pulses recorded at a temperature of 310 mK and for a selection of different magnetic fields. All heat pulses were fitted with the same algorithm. The values for τ_2 were extracted from the fit. The gray shading marks the heat pulses that can't be handled properly by the fit due to an anomalous thermal relaxation.

In certain regions of the magnetic phase diagram of $CoNb_2O_6$, it was not possible to extract the heat capacity from thermal relaxation measurements with sufficient reliability. This issue was due to the presence of a non-exponential thermal relaxation in these regions of the magnetic phase diagram, as illustrated in Fig. 4.25.

Fig. 4.25 presents a selection of heat pulses for a temperature of 310 mK and various magnetic fields. The fit to the data is inadequate for magnetic fields below 4 T, as shown in Fig. 4.25 (a)-(c). Proper fits were only possible between 4 T and 6 T, as seen in Fig. 4.25 (d)-(f). For magnetic fields exceeding 6 T, the fits exhibit a pronounced deviation, as shown in Fig. 4.25 (g) and (h).

The quality of the fit with respect to the data also correlates with the value τ_2 extracted from the fit. A proper fit results in a relatively small value of τ_2. Other groups have also observed unusual thermal relaxation in these temperature and field regions [35, 42], as well as anomalies in domain growth kinetics at milli-Kelvin temperatures [125, 126, 132, 134].

Although the fits for the extraction do not work ideally in the glassy regimes, one of the resulting parameters, namely τ_2, can be employed as an indicator of the phase boundary of this glassy regime. This approach has been adopted from other research groups [42]. It is important to note that in the glassy regime, all parameters extracted from the fit to the heat pulse are strongly dependent on the measurement parameters, such as heating time and relaxation time. Therefore, in order to focus on the anomalous thermal relaxation effects, the measurements had to be performed in a systematic manner with fixed measurement times and heating amplitudes.

In order to achieve a reliable fit, it is necessary to ensure that the value of τ_2 is as small as possible, particularly that τ_1, the time constant characteristic of the heat capacity of the sample in a given measurement setup, is significantly larger than τ_2. However, this is not the case in the regions of the phase diagram designated as glassy. The standard two-τ model is inadequate for fitting the thermal relaxation curves in these regions, as it fails to provide a satisfactory fit of the data for extracting the heat capacity and other parameters. Instead, the fit attempts to compensate the changed shape of the heat pulse by increasingly large values of τ_2.

Fig. 4.26 presents the temperature dependence of τ_2 for a selection of constant magnetic fields up to 8 T. In zero magnetic field, as shown in Fig. 4.26 (a), a comparatively small τ_2 is observed above a temperature $T_G = 0.96$ K. At this temperature T_G, τ_2 suddenly becomes much larger as the temperature continues to decrease.

When a magnetic field is applied in a direction perpendicular to the Ising axis, the sharp edge in τ_2 marking T_G shifts to lower temperatures with increasing magnetic field as is shown in Fig. 4.26 (b) and (c). For magnetic fields ranging from 4 T to 5.7 T, the value of τ_2 remains at a constant low level as illustrated in Figs. 4.26 (d)-(f).

For larger magnetic fields, the edge in τ_2 marking T_G reappears at a field of 6.5 T at a

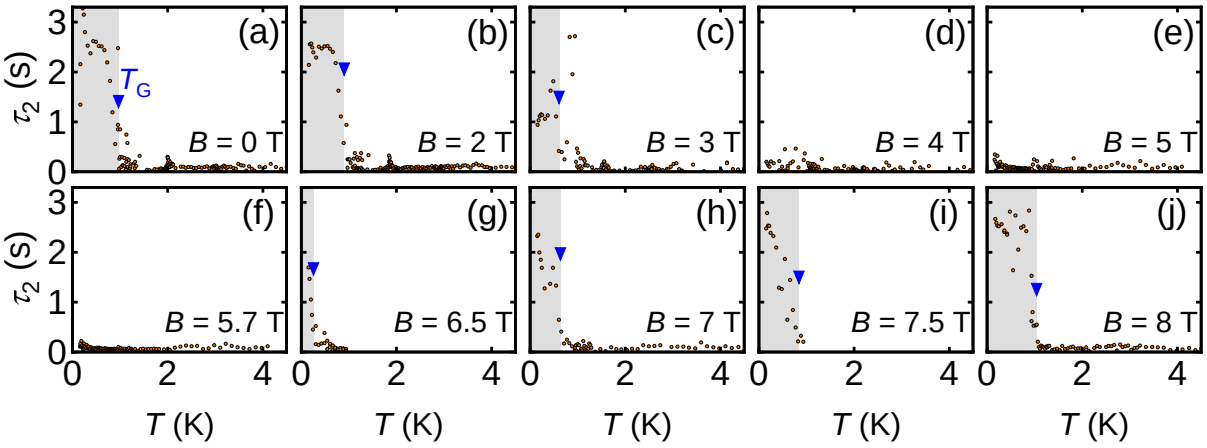

Figure 4.26: Temperature dependence of the time constant τ_2 at milli-Kelvin temperatures for a selection of constant magnetic fields between 0 T and 8 T.

temperature of $T_G = 0.24$ K in Fig. 4.26 (g). As the magnetic field is further increased, the edge marking T_G shifts to higher temperatures as shown in Figs. 4.26 (h)-(j).

Fig. 4.27 illustrates the magnetic field dependence of τ_2 for a selection of temperatures between 0.16 K and 0.61 K. Starting from a magnetic field of 8 T at a temperature of 160 mK in Fig. 4.27 (a), τ_2 decreases sharply as the magnetic field decreases until a low level is reached at $B_{G2} = 6$ T. Between $B_{G2} = 6$ T and $B_{G1} = 4$ T, the value of τ_2 stays at a constant low level. Below $B_{G1} = 4$ T, τ_2 begins to rise again as the magnetic field is decreased further.

In Fig. 4.27 (b), the magnetic field dependence at 200 mK is shown, which is essentially analogous to the magnetic-field dependence at 160 mK as depicted in Fig. 4.27 (a). In Fig. 4.27 (c)-(f) the magnetic field B_{G1} was extracted from a shoulder-like signature in Fig. 4.18 (j)-(l) and not from the magnetic field dependence of τ_2 in Fig. 4.27. As the temperature increases, B_{G1} shifts to lower magnetic fields. In Figs. 4.27 (d)-(f), B_{G2} shifts to higher magnetic fields as the temperature increases.

In conclusion, the analysis of τ_2 must be approached with caution, because in the context of the glassy regime, τ_2 only serves as empirical indicator for the deviation from the expected behavior of the thermal relaxation and does not have a physical meaning as the model for the fit is inadequate. Furthermore, the extracted values for τ_2 are highly dependent on the measurement parameters in the regimes designated as glassy. The positions of the glassy regions extracted from the temperature and magnetic field dependence of τ_2 are consistent with the observations in Ref. [35].

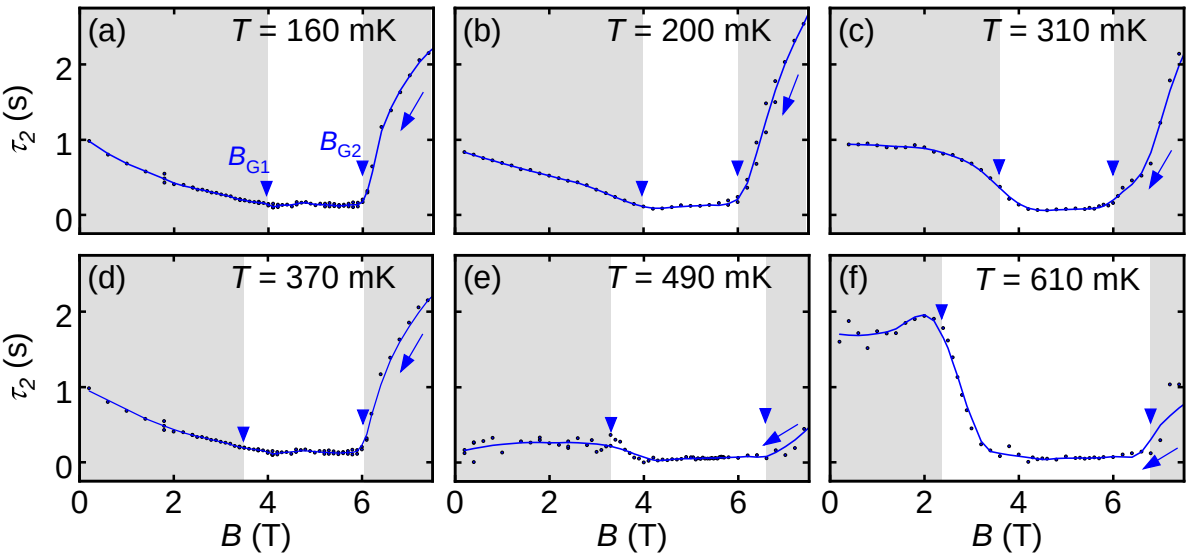

Figure 4.27: Magnetic field dependence of the time constant τ_2 at fairly constant milli-Kelvin temperatures. The gray shaded area marks regions with an anomalous thermal relaxation. The data was recorded for a decreasing magnetic field. The blue lines are smooths of the data and serve as a guide to the eye.

4.5.8 Angular dependence of τ_2

Fig. 4.28 presents the influence of the angle between the magnetic field and the $\langle 010 \rangle$ direction on the specific heat and the time constant τ_2. Fig. 4.28 (a) shows the magnetic field dependence of the specific heat for a selection of different angles between the magnetic field and the $\langle 010 \rangle$ direction. For the perfect transverse orientation (0° misalignment) the heat capacity shows two maxima at 3.5 T and 5 T. Below 4 T, the heat capacity is much larger in the perfect transverse orientation than for any misalignment angle as shown in Fig. 4.28 (a). In addition, a plateau is observed in the vicinity of 7 T.

For all non-zero misalignment angles in Fig. 4.28 the specific heat is low between 2 T and 3 T. At misalignment angles of 2° and 4°, additional contributions to the specific heat are observed below 1 T. At a misalignment of ±4°, the specific heat has a broad maximum at 5 T and a shoulder at 4 T. For larger misalignment angles, the specific heat becomes smaller.

In Fig. 4.28 (b), the magnetic field dependence of τ_2 is plotted for a selection of different angles between the magnetic field and the $\langle 010 \rangle$ direction ranging from -4° to +16°.

For the perfect orientation (0°), τ_2 shows a plateau below 2 T with a value slightly below 1 s. With increasing magnetic field, τ_2 decreases towards a broad valley with small values of τ_2 between 4 T and 6 T. Above 6 T, τ_2 increases sharply up to a value of 3 s for a

magnetic field of 8 T. For misaligned orientations, τ_2 takes larger values below 4 T and shows a broad maximum between 2 T and 3 T. The regime with small values of τ_2 in the vicinity of 5.5 T becomes narrower with increasing misalignment angle. For large misalignment angles of 12° and 16°, τ_2 takes large values $\geq$ 1.5 s for all magnetic fields between 0 T and 8 T, showing only small variations as a function of magnetic field.

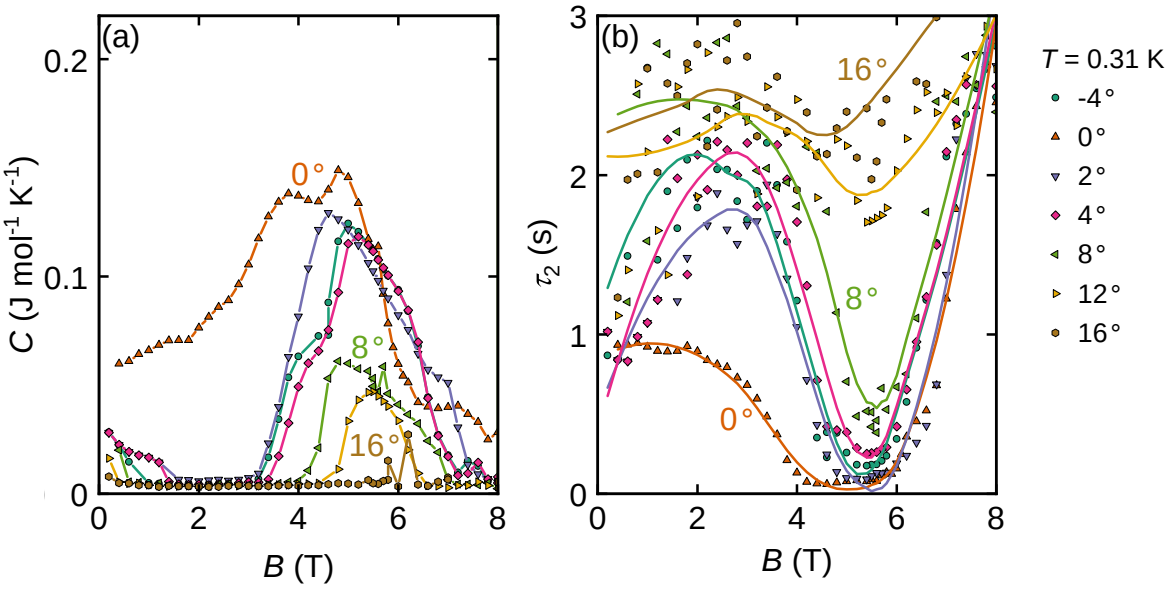

Figure 4.28: Magnetic field dependence of (a) the specific heat and (b) the time constant τ_2 at a temperature of 310 mK for a selection of different angles between the magnetic field and the ⟨010⟩ direction. In (b), smooths through each set of data serve as guides to the eyes.

The investigation of the angular dependence of τ_2 indicates that the anomalous behavior of the thermal relaxation and the extent of the associated glassy regime is strongly influenced by the presence of the quantum phase transition for the perfect transverse field orientation. The extent of regions with anomalous thermal relaxation and large values of τ_2 is minimal for the perfect transverse orientation.

4.5.9 Critical Scaling of the Phase Transitions

The investigation of critical exponents is of central interest in the research field of second-order quantum phase transitions [108]. In the vicinity of second order phase transitions, measurement quantities, for example the heat capacity, the magnetization or the susceptibility may be proportional to $|g - g_c|^{-e}$ with g being an external parameter like the magnetic field, g_c the critical value of the external parameter, and e the critical exponent. The critical exponent of different parameters may be used for a comparison

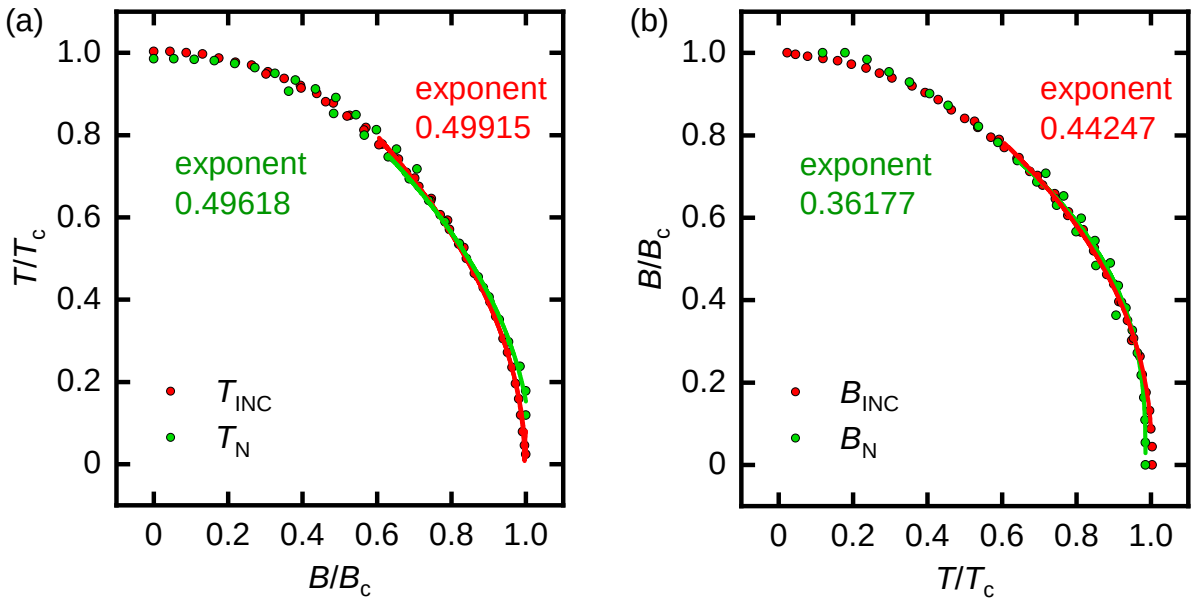

Figure 4.29: Critical scaling of the paramagnetic-to-incommensurate and of the incommensurate-to-commensurate antiferromagnetic transition for a perfect transverse orientation. (a) Magnetic field dependence of the critical temperatures T_{INC} and T_{N}. (a) Temperature dependence of the critical fields B_{INC} and B_{N}. A power-law fit was applied in the vicinity of the critical field $B/B_{\mathrm{c}} = 1$ in (a) and in the vicinity of the critical temperature $T/T_{\mathrm{c}} = 1$ in (b).

between theoretical models and experimental results [144–146]. For the critical trajectories $T_{\mathrm{C}}(B) \propto |g - g_c|^{-e}$ of the antiferromagnetic Ising-chain compounds $BaCo_2V_2O_8$ and $SrCo_2V_2O_8$, critical exponents of $e_{1\mathrm{D}} = 1$ for the 1D-quantum critical point were reported [147, 148]. For the critical trajectory $T_{\mathrm{C,3D}}(B)$ towards the 3D-quantum critical point in the case of the antiferromagnetic Ising-chain compounds $SrCo_2V_2O_8$ [148, 149] and $CaCoV_2O_7$ [150], values of $e_{3\mathrm{D}} = 0.5$ and $e_{3\mathrm{D}} = 0.164$, respectively, were reported.

We have focused on the evaluation of the critical scaling of the evolution of the phase boundaries between the paramagnetic and incommensurate phase and between the incommensurate and the antiferromagnetic phase. Fig. 4.29 shows the critical scaling of the transition temperatures $T_{\mathrm{INC}}(B)$ and $T_{\mathrm{N}}(B)$ and the transition fields $B_{\mathrm{INC}}(T)$ and $B_{\mathrm{N}}(T)$. Fig. 4.29 (a) displays the magnetic field dependence of the two transition temperatures T_{INC} and T_{N}, with both axes normalized using the critical values of the two transitions. The two curves exhibit a remarkable congruence. A power-law fit was performed using the equation $T/T_{\mathrm{c}} = A \cdot ((B/B_{\mathrm{c}}) - b)^{\mathrm{exp}}$ in the vicinity of $B/B_{\mathrm{c}} = 1$. The resulting exponent for both curves is approximately 1/2. This exponent is equivalent to the critical exponent of the critical trajectory of the 3D-quantum critical point in $SrCo_2V_2O_8$ [148, 149]. Fig. 4.29 (b) presents the two critical fields as a function of the reduced temperatures T/T_{c}.

The exponents resulting from the power law fits in the vicinity of $T/T_c = 1$ deviate in this case, with values of 0.362 for B_N and 0.442 for B_{INC}. The results of this analysis may be used for the comparison with predictions of future theoretical predictions of the magnetic phase diagram.

4.6 Summary

In this chapter, the synthesis of single crystal $CoNb_2O_6$ and the investigation of its physical properties at cryogenic temperatures were presented. Single crystal material was prepared from a mixture of Co_3O_4 and Nb_2O_5 using a combination of a solid state reaction and the optical floating zone technique. The quality of the synthesized material was assessed using X-ray Laue and powder diffraction.

Investigations of the heat capacity, the magnetic ac susceptibility, and the magnetization were in excellent agreement with the literature. In zero magnetic field, prominent signatures were observed in the heat capacity and ac susceptibility at the two magnetic phase transitions, $T_{\mathrm{INC}} = 3.04\,\mathrm{K}$ and $T_{\mathrm{N}} = 1.97\,\mathrm{K}$. The magnetic field dependence of the magnetization showed a pronounced anisotropy with a hard magnetic axis parallel to $\langle 010 \rangle$ direction.

The derivative of the magnetic field dependence of the magnetization for a magnetic field applied parallel to the hard magnetic axis deviates from the ac susceptibility in the paramagnetic regime. This deviation is typically not expected and may be explained by the presence of one-dimensional ferromagnetic fluctuations already present above the magnetic ordering temperature T_{INC}. A broad maximum at T_{x} in the longitudinal susceptibility inside the paramagnetic regime indicated the presence of a crossover and strong anisotropy effects.

Heat capacity and ac susceptibility measurements were used to study quantum phase transitions in a transverse magnetic field. Cryogenic temperatures were provided by a dilution refrigerator insert. A vector magnet was used to precisely align the magnetic field perpendicular to the Ising axes of $CoNb_2O_6$. The process of aligning the magnetic field in the perfect transverse configuration was described.

The results of heat capacity, magnetocaloric, and ac susceptibility measurements for the transverse configuration were used to extract a magnetic phase diagram. Based on prominent signatures in the measured quantities and on the comparison with existing publications on the magnetic phase diagrams, five regimes in the magnetic phase diagram for the transverse field orientation were identified: an regime dominated by the anisotropy, a paramagnetic regime, an incommensurate phase, an antiferromagnetic phase and a glassy region characterized by an anomalous thermal relaxation. Additional signatures in the imaginary part of the transverse ac susceptibility and the magnetocaloric measurements in the vicinity of the quantum phase transition at the magnetic field B_{N} at milli-Kelvin temperatures indicated the presence of an emerging phase pocket.

The extracted phase diagram provides information about the relevant energy scales of the different interactions in the system. The onset of the magnetic contribution to the heat capacity in zero magnetic field in the vicinity of 20 K is characteristic for the ferromagnetic intra-chain coupling of the cobalt moments. The anisotropy of the cobalt spins manifest in a broad maximum in the longitudinal susceptibility at a temperature T_x outside of the ordered magnetic regime.

Under intentional misalignment of the magnetic field, emerging signatures indicate the presence of an additional phase. This emergent phase may be connected to a spin-flip phase also present for a magnetic field parallel to the easy $\langle 001 \rangle$ direction. Below a temperature of 1 K, all signatures in the transverse susceptibility disappeared except for a maximum at the boundary between paramagnetic and ordered magnetic phase. Temperature spikes were observed in the measurement of the magnetocaloric effect below a temperature of 1 K for a misaligned magnetic field orientation. These spikes show a hysteretic behavior and indicate an emerging first-order phase transition. Presumably, this first-order phase transition is connected to hysteretic phase transitions observed for a magnetic field parallel to the $\langle 001 \rangle$ direction as reported in the literature [132].

Phase boundaries derived from signatures in measurements of the magnetocaloric effect are consistent with the results of heat capacity and ac susceptibility measurements. The change of entropy was inferred from the measurements of the magnetocaloric effect and the heat capacity. At a temperature of 720 mK, the magnetic field dependence of the change of entropy resembles that of the behavior of the susceptibility along the $\langle 100 \rangle$ direction as a function of temperature in zero magnetic field.

The regions of anomalous thermal relaxation are consistent with the existing literature. However the origin of this unusual thermal property remains obscure. In the vicinity of the quantum phase transitions, the thermal relaxation exhibits a standard exponential behavior.

The critical scaling of the transition temperatures and transition fields for the two quantum phase transitions exhibit a excellent congruence. For both quantum phase transitions, the scaling of $T(B)$ towards lowest temperatures result in critical exponents very close to 1/2. This is the same value as reported for the 3D-quantum critical point of the antiferromagnetic Ising-chain compound $SrCo_2V_2O_8$ [148, 149]. The interpretation of this exponent requires further investigations.

5 Conclusions

In this study we have investigated the properties of Ising systems in transverse magnetic fields. We have conducted ac susceptibility and heat capacity measurements as well as elastic neutron diffraction experiments. The central results include hard-axis magnetic phase diagrams of the two Ising compounds $TbFeO_3$ and $CoNb_2O_6$ and the effects of tilting the magnetic field away from a orientation transverse to the Ising directions of the two compounds. The first chapter of this thesis addressed the methods employed for the synthesis and investigation of quantum magnets. The second chapter presented findings of neutron scattering experiments and the study of the susceptibility of the soliton-lattice host $TbFeO_3$ in a transverse magnetic field. The third chapter presented the investigation of the magnetic and caloric properties of the Ising chain compound $CoNb_2O_6$ in a transverse magnetic field.

In a neutron diffraction experiment, we observed signatures of the soliton lattice phase in a transverse magnetic field using single-crystal $TbFeO_3$ synthesized in an earlier work [39]. In analogy to Ref. [15], we found a large number of higher harmonic reflections, which are characteristic of the presence of the soliton lattice phase. The characteristic reflections remained stable up to the maximal accessible magnetic field of 12 T. In contrast to the measurement of the longitudinal ac susceptibility, we found signatures of the low-temperature phase boundary of the soliton lattice phase in the temperature dependence of the transverse ac susceptibility. A better resolution of these signatures was achieved by means of a small easy-axis component of the magnetic field. First measurements of the heat capacity of $TbFeO_3$ yielded promising results. However, further measurements are necessary to confirm these findings, and a more rigid heat capacity setup should be employed.

We have synthesized single-crystal $CoNb_2O_6$ using a combination of a solid-state reaction technique and the optical floating-zone method. From the synthesized material, we have prepared a spherical sample for the ac susceptibility and heat capacity measurements in a transverse magnetic field. First measurements to characterize the magnetic properties demonstrated good agreement with the existing literature. We demonstrated that the exact alignment of the magnetic field transverse to the two Ising axes of the cobalt spins is essential for the measurement of the transverse susceptibility and heat capacity measurements. A procedure was presented for the precise alignment of the magnetic field in a perpendicular direction to the Ising axes of $CoNb_2O_6$.

Based on the experimental results of the magnetic and caloric properties in a transverse magnetic field, we have presented a comprehensive magnetic phase diagram for $CoNb_2O_6$.

The phase diagram illustrates the evolution of the incommensurate and the antiferromagnetic phases down to temperatures of 80 mK in a transverse magnetic field of up to 8 T. Both phases persist down to the lowest temperature. Furthermore, the imaginary part of the transverse susceptibility indicates the emergence of an additional phase pocket in the vicinity of the one-dimensional quantum critical point at approximately 4.65 T. This observation is corroborated by emerging signatures in the temperature variation due to the magnetocaloric effect. A phase pocket in the vicinity of the one-dimensional quantum critical point may be consistent with an effective model which takes into account an isosceles distortion of the interchain couplings [105]. In contrast to the findings of Liang et al., we do not observe a heat capacity peak at a quantum critical point [35]. Instead, a broad increase in the heat capacity is observed towards the lowest temperature of 160 mK for magnetic field below 6 T. The origin of this increase is currently unclear. The critical scaling of the transition temperature of the two quantum phase transitions $T_{\mathrm{N}}(B)$ and $T_{\mathrm{INC}}(B)$ resulted in exponents of 1/2. This is the same value as for the critical trajectory of the 3D quantum critical point of the antiferromagnetic Ising chain coumpound $SrCo_2V_2O_8$ [148, 149]. The interpretation of this value of these exponents requires further investigation.

The introduction of a misalignment angle of 0.9° resulted in a drastic change of the magnetic phase diagram. The emergence of a new phase boundary suggests the existence of a spin-flip phase, which was not observed in the case of a perfect transverse field orientation. The spin-flip phase may be associated with a magnetic phase observed for a magnetic field applied parallel to the ⟨001⟩ direction [115]. In contrast, at milli-Kelvin temperatures, signatures in the transverse susceptibility indicate only one quantum phase transition in a tilted magnetic field. The measurement of the magnetocaloric effect in this case of a misaligned magnetic field showed the emergence of spikes in the sample temperature. These temperature spikes may indicate first-order phase transitions involving latent heat. The magnetic fields at which the temperature spikes were observed exhibited an increasing hysteresis with decreasing temperature. A hysteretic behavior was also observed for a magnetic field parallel to the ⟨001⟩ direction [132].

At low temperatures below 1 K, an anomalous thermal relaxation was observed, in accordance with observations from other groups [35, 42]. This anomalous behavior in the thermal relaxation was not observed in the vicinity of the quantum critical point. Furthermore, an intentional misalignment of the magnetic field also results in a broadening of the region of anomalous thermal relaxation.

6 References

[1] M. Fava, R. Coldea, and S. A. Parameswaran. "Glide Symmetry Breaking and Ising Criticality in the Quasi-1D Magnet $CoNb_2O_6$". In: *Proceedings of the National Academy of Sciences* 117 (2020), p. 25219. DOI: 10.1073/pnas.2007986117.

[2] R. Okazaki et al. "Rotational Symmetry Breaking in the Hidden-Order Phase of URu2Si2". In: *Science* 331 (2011), p. 439. DOI: 10.1126/science.1197358.

[3] M. A. Wilde et al. "Symmetry-Enforced Topological Nodal Planes at the Fermi Surface of a Chiral Magnet". In: *Nature* 594 (2021), p. 374. DOI: 10.1038/s41586-021-03543-x.

[4] Y. Enomoto et al. "Evaluation of Experimental Permanent-Magnet Brushless Motor Utilizing New Magnetic Material for Stator Core Teeth". In: *IEEE Transactions on Magnetics* 41 (2005), p. 4304. DOI: 10.1109/TMAG.2005.857943.

[5] O. Gutfleisch et al. "Magnetic Materials and Devices for the 21st Century: Stronger, Lighter, and More Energy Efficient". In: *Advanced Materials* 23 (2011), p. 821. DOI: 10.1002/adma.201002180.

[6] J. M. Silveyra et al. "Soft Magnetic Materials for a Sustainable and Electrified World". In: *Science* 362 (2018), eaao0195. DOI: 10.1126/science.aao0195.

[7] A. Hirohata and K. Takanashi. "Future Perspectives for Spintronic Devices". In: *Journal of Physics D: Applied Physics* 47 (2014), p. 193001. DOI: 10.1088/0022-3727/47/19/193001.

[8] S. T. Bramwell and M. J. P. Gingras. "Spin Ice State in Frustrated Magnetic Pyrochlore Materials". In: *Science* 294 (2001), p. 1495. DOI: 10.1126/science.1064761.

[9] L. D. C. Jaubert and P. C. W. Holdsworth. "Signature of Magnetic Monopole and Dirac String Dynamics in Spin Ice". In: *Nature Physics* 5 (2009), p. 258. DOI: 10.1038/nphys1227.

[10] S. Mühlbauer et al. "Skyrmion Lattice in a Chiral Magnet". In: *Science* 323 (2009), p. 915. DOI: 10.1126/science.1166767.

[11] A. Banerjee et al. "Proximate Kitaev Quantum Spin Liquid Behaviour in a Honeycomb Magnet". In: *Nature Materials* 15 (2016), p. 733. DOI: 10.1038/nmat4604.

[12] S.-H. Do et al. "Majorana Fermions in the Kitaev Quantum Spin System α-RuCl3". In: *Nature Physics* 13 (2017), p. 1079. DOI: 10.1038/nphys4264.

[13] R. Gross and A. Marx. *Festkörperphysik*. 2., akt. Aufl. De Gruyter Oldenbourg, 2014. DOI: 10.1524/9783110358704.

[14] S. Blundell. *Magnetism in Condensed Matter*. 1. publ., repr. Oxford Univ. Press, 2011.

[15] S. Artyukhin et al. "Solitonic Lattice and Yukawa Forces in the Rare-Earth Orthoferrite $TbFeO_3$". In: *Nature Materials* 11 (2012), p. 694. DOI: 10.1038/nmat3358.

[16] R. Coldea et al. "Quantum Criticality in an Ising Chain: Experimental Evidence for Emergent E8 Symmetry". In: *Science* 327 (2010), p. 177. DOI: 10.1126/science.1180085.

[17] J. A. Ringler, A. I. Kolesnikov, and K. A. Ross. "Single-Ion Properties of the Transverse-Field Ising Model Material $CoNb_2O_6$". In: *Physical Review B* 105 (2022), p. 224421. DOI: 10.1103/PhysRevB.105.224421.

[18] C. M. Morris et al. "Duality and Domain Wall Dynamics in a Twisted Kitaev Chain". In: *Nature Physics* 17 (2021), p. 832. DOI: 10.1038/s41567-021-01208-0.

[19] L. Woodland et al. "Excitations of Quantum Ising Chain $CoNb_2O_6$ in Low Transverse Field: Quantitative Description of Bound States Stabilized by off-Diagonal Exchange and Applied Field". In: *Physical Review B* 108 (2023), p. 184417. DOI: 10.1103/PhysRevB.108.184417.

[20] L. Woodland et al. "Tuning the Confinement Potential between Spinons in the Ising Chain Compound $CoNb_2O_6$ Using Longitudinal Fields and Quantitative Determination of the Microscopic Hamiltonian". In: *Physical Review B* 108 (2023), p. 184416. DOI: 10.1103/PhysRevB.108.184416.

[21] G. Sim, J. Knolle, and F. Pollmann. *Nonlinear Spectroscopy of Bound States in Perturbed Ising Spin Chains*. 2022. arXiv: 2209.00720 [cond-mat].

[22] G. Sim, J. Knolle, and F. Pollmann. "Nonlinear Spectroscopy of Bound States in Perturbed Ising Spin Chains". In: *Physical Review B* 107 (2023), p. L100404. DOI: 10.1103/PhysRevB.107.L100404.

[23] G. Sim, F. Pollmann, and J. Knolle. "Microscopic Details of Two-Dimensional Spectroscopy of One-Dimensional Quantum Ising Magnets". In: *Physical Review B* 108 (2023), p. 134423. DOI: 10.1103/PhysRevB.108.134423.

[24] H. Xu and H.-Y. Kee. "Creating Long-Range Entangled Majorana Pairs: From Spin-1/2 Twisted Kitaev to Generalized X Y Chains". In: *Physical Review B* 107 (2023), p. 134435. DOI: 10.1103/PhysRevB.107.134435.

[25] D. Churchill and H.-Y. Kee. *Transforming from Kitaev to Disguised Ising Chain: Application to $CoNb_2O_6$*. 2024. DOI: 10.48550/arXiv.2403.14754. arXiv: 2403.14754 [cond-mat].

[26] N. Xi et al. *Emergent $D_8^{(1)}$ Spectrum and Topological Soliton Excitation in $CoNb_2O_6$*. 2024. arXiv: 2403.10785 [cond-mat, physics:math-ph].

[27] S. Suzuki, J.-ichi Inoue, and B. K. Chakrabarti. "Transverse Ising Chain (Pure System)". In: *Quantum Ising Phases and Transitions in Transverse Ising Models*. Vol. 862. Springer Berlin Heidelberg, 2013, p. 13. DOI: 10.1007/978-3-642-33039-1_2.

[28] S. Sachdev. "Quantum Phase Transitions". In: *Physics World* 12 (1999), p. 33. DOI: 10.1088/2058-7058/12/4/23.

[29] A. B. Zamolodchikov. "Integrals of Motion and S-Matrix of the (Scaled) $T = T_c$ Ising Model with Magnetic Field". In: *International Journal of Modern Physics A* 04 (1989), p. 4235. DOI: 10.1142/S0217751X8900176X.

[30] K. P. Belov, A. K. Zvezdin, and A. A. Mukhin. "Magnetic Phase Transitions in Terbium Orthoferrite". Trans. by W. F. Brown Jr. In: (1979), p. 6.

[31] A. Wendl et al. "Emergence of Mesoscale Quantum Phase Transitions in a Ferromagnet". In: *Nature* 609 (2022), p. 65. DOI: 10.1038/s41586-022-04995-5.

[32] N. Bonacic. "Measurements of Heat Capacity of Systems with Complex Magnetic Phase Diagrams for Magnetic Field along Hard Magnetisation Axes". Master's Thesis. 2016.

[33] A. Wendl. "Transverse-Field Ising Transition under Tilted Magnetic Field". PhD thesis. TU Munich, 2023.

[34] D. Prabhakaran, F.R. Wondre, and A.T. Boothroyd. "Preparation of Large Single Crystals of ANb_2O_6 (A=Ni, Co, Fe, Mn) by the Floating-Zone Method". In: *Journal of Crystal Growth* 250 (2003), p. 72. DOI: 10.1016/S0022-0248(02)02229-7.

[35] T. Liang et al. “Heat Capacity Peak at the Quantum Critical Point of the Transverse Ising Magnet $CoNb_2O_6$”. In: *Nature Communications* 6 (2015). DOI: 10.1038/ncomms8611.

[36] T. Hanawa, M. Ishikawa, and K. Miyatani. “Disappearance of Ferromagnetism at Low Temperatures in $CoNb_2O_6$”. In: *Journal of the Physical Society of Japan* 61 (1992), p. 4287. DOI: 10.1143/JPSJ.61.4287.

[37] W. Scharf et al. “Magnetic Structures of $CoNb_2O_6$”. In: *Journal of Magnetism and Magnetic Materials* 13 (1979), p. 121. DOI: 10.1016/0304-8853(79)90044-1.

[38] P. W. C. Sarvezuk et al. “New Investigation of the Magnetic Structure of $CoNb_2O_6$ Columbite”. In: *Journal of Applied Physics* 109 (2011), 07E160. DOI: 10.1063/1.3562516.

[39] A. Engelhardt. “Single-Crystal Growth and the Study of Correlation Effects in the Magnetoelectric Compound $TbFeO_3$”. MA thesis. TU Munich, 2019.

[40] Y.-J. Ke et al. “Anisotropic Magnetic Entropy Change in $RFeO_3$ Single Crystals(R = Tb, Tm, or Y)”. In: *Scientific Reports* 6 (2016). DOI: 10.1038/srep19775.

[41] Y. Cao et al. “Magnetic Phase Transition and Giant Anisotropic Magnetic Entropy Change in $TbFeO_3$ Single Crystal”. In: *Journal of Applied Physics* 119 (2016), p. 063904. DOI: 10.1063/1.4941105.

[42] C. L. Sarkis et al. “Low-Temperature Domain-Wall Freezing and Nonequilibrium Dynamics in the Transverse-Field Ising Model Material $CoNb_2O_6$”. In: *Physical Review B* 104 (2021), p. 214424. DOI: 10.1103/PhysRevB.104.214424.

[43] D. Bitko, T. F. Rosenbaum, and G. Aeppli. “Quantum Critical Behavior for a Model Magnet”. In: *Physical Review Letters* 77 (1996), p. 940. DOI: 10.1103/PhysRevLett.77.940.

[44] F. Rucker. “Transverse Susceptibility of Complex Magnetic Textures”. PhD thesis. Technische Universität München, 2018.

[45] F. Rucker and C. Pfleiderer. “Compact Susceptometer for Studies under Transverse Field Geometries at Very Low Temperatures”. In: *Review of Scientific Instruments* 90 (2019), p. 073903. DOI: 10.1063/1.5087949.

[46] C. Pfleiderer. “Miniature Ac Susceptometers for Use inside Clamp Type Pressure Cells”. In: *Review of Scientific Instruments* 68 (1997), p. 1532. DOI: 10.1063/1.1147642.

[47] J. S. Hwang, K. J. Lin, and C. Tien. “Measurement of Heat Capacity by Fitting the Whole Temperature Response of a Heat-Pulse Calorimeter”. In: *Review of Scientific Instruments* 68 (1997), p. 94. DOI: 10.1063/1.1147722.

[48] Quantum Design. *Heat Capacity Option User’s Manual*. 2017.

[49] A. W. Rost and P. A. Mackenzi. *Magnetothermal Properties near Quantum Criticality in the Itinerant Metamagnet $Sr_3Ru_2O_7$*. Springer Berlin Heidelberg, 2010. DOI: 10.1007/978-3-642-14524-7.

[50] R. Bidaux, J.E. Bouree, and J. Hammann. “Diagramme de phase de l’orthoferrite de terbium en présence d’un champ magnétique”. In: *Journal de Physique* 36 (1975), p. 803. DOI: 10.1051/jphys:01975003609080300.

[51] K. P. Belov, A. K. Zvezdin, and A. M. Kadomtseva. “Metamagnetic Phase Transitions and Instability of Magnetic Structure in Rare-Earth Orthoferrites”. In: 76 (1979), p. 6.

[52] V. N. Derkachenko. "Magnetic Field Induced Spin-Reorientational Phase Transitions in Terbium Orthoferrite". In: *Fizika Tverdogo Tela (Leningrad)* 22 (1980), p. 1753.

[53] O. Nikolov et al. "A Mossbauer Study of Temperature-Driven Spin-Reorientation Transitions in $TbFeO_3$". In: *Journal of Physics: Condensed Matter* 6 (1994), p. 3793. DOI: 10.1088/0953-8984/6/20/019.

[54] O. Nikolov et al. "Field-Induced Spin Reorientations in $TbFeO_3$ at 4.2 K". In: *Journal of Magnetism and Magnetic Materials* 152 (1996), p. 75.

[55] A. K. Zvezdin and A. A. Mukhin. "Magnetoelectric Interactions and Phase Transitions in a New Class of Multiferroics with Improper Electric Polarization". In: *JETP Letters* 88 (2008), p. 505. DOI: 10.1134/S0021364008200083.

[56] E. F. Bertaut et al. "Structures Magnetiques de TbFeO3". In: *Solid State Communications* 5 (1967), p. 293. DOI: 10.1016/0038-1098(67)90276-1.

[57] A. Gukasov et al. "Neutron Scattering Study of Spin Waves in $TbFeO_3$". In: *Physica B: Condensed Matter* 234–236 (1997), p. 760. DOI: 10.1016/S0921-4526(96)01156-8.

[58] A. K. Ovsianikov et al. "Inelastic Neutron Studies and Diffraction in Magnetic Fields of $TbFeO_3$ and $YbFeO_3$". In: *Journal of Magnetism and Magnetic Materials* 563 (2022).

[59] T. N. Stanislavchuk et al. "Far-IR Magnetospectroscopy of Magnons and Electromagnons in $TbFeO_3$ Single Crystals at Low Temperatures". In: *Physical Review B* 95 (2017), p. 054427. DOI: 10.1103/PhysRevB.95.054427.

[60] S. A. Skorobogatov et al. "Spin Dynamics and Exchange Interaction in Orthoferrite $TbFeO_3$ with Non-Kramers Rare-Earth Ion". In: *Physical Review B* 106 (2022), p. 184404. DOI: 10.1103/PhysRevB.106.184404.

[61] Y. H. Zou et al. "Spin Dependent Electrical Abnormal in $TbFeO_3$". In: *Journal of Alloys and Compounds* 519 (2012), p. 82. DOI: 10.1016/j.jallcom.2011.12.058.

[62] E. F. Bertaut. "Magnetic Structure Analysis and Group Theory". In: *Le Journal de Physique Colloques* 32 (1971), p. C1. DOI: 10.1051/jphyscol:19711156.

[63] D. Treves. "Studies on Orthoferrites at the Weizmann Institute of Science". In: *Journal of Applied Physics* 36 (1965), p. 1033. DOI: 10.1063/1.1714088.

[64] S. B. Kim et al. "Extraordinary Magnetic Behavior in $TbFeO_3$". In: *Journal of Magnetism and Magnetic Materials* 310 (2007), e592. DOI: 10.1016/j.jmmm.2006.11.193.

[65] I. M. Khalatnikov and K. P. Belov. *Soviet Scientific Reviews*. Vol. 9. CRC Press, 1987.

[66] R. Bidaux, J. E. Bouree, and J. Hammann. "Dipolar Interactions in Rare Earth Orthoferrites—II $TbFeO_3$". In: *Journal of Physics and Chemistry of Solids* 36 (1974), p. 655. DOI: 10.1016/0022-3697(75)90083-9.

[67] J. D. Gordon, G. Gorodetsky, and R. M. Hornreich. "Magnetization Studies of $TbFeO_3$". In: *Journal of Magnetism and Magnetic Materials* 3 (1976), p. 288.

[68] J.E. Bourée and J. Hammann. "Mise en évidence expérimentale des effets de forme dans l'orthoferrite de terbium". In: *Journal de Physique* 36 (1975), p. 391. DOI: 10.1051/jphys:01975003605039100.

[69] M. Belakhovsky et al. "SUCCESSIVE REORIENTATIONS OF IRON MOMENTS IN $YbFeO_3$, $TbFeO_3$ AND $ErFeO_3$". In: *Le Journal de Physique Colloques* 32 (1971), p. C1. DOI: 10.1051/jphyscol:19711162.

[70] R. Bidaux, J. E. Bouree, and J. Hammann. "Shape Effects and Magnetic Properties of $TbFeO_3$". In: 40 (1972), p. 2.

[71] A. K. Zvezdin, A. A. Mukhin, and A. I. Popov. "Magnetic-Structure Instability Resulting from Intersection of Energy Levels". In: 23 (1976), p. 267.

[72] A. De Combarieu et al. "Chaleurs Specifiques Entre 1,2 et 5 K de Quelques Perovskites de Terres Rares". In: *Solid State Communications* 6 (1968), p. 257. DOI: 10.1016/0038-1098(68)90099-9.

[73] J. Mareschal and J. Sivardière. "Structures magnétiques des orthoferrites de terres rares". In: *Journal de Physique* 30 (1969), p. 967. DOI: 10.1051/jphys:019690030011-12096700.

[74] J. Peyrard and J. Sivardiere. "Chaleurs Specifiques a Basse Temperature de Quelques Orthoferrites de Terres Rares". In: *Solid State Communications* 7 (1969), p. 605. DOI: 10.1016/0038-1098(69)90627-9.

[75] V. N. Derkachenko et al. "Effect of Magnetic Vacancies on Magnetic Properties of Terbium Orthoferrites". In: *Physica Status Solidi (a)* 84 (1984), p. 215. DOI: 10.1002/pssa.2210840127.

[76] A. Bombik, B. Leśniewska, and A. W. Pacyna. "AC Susceptibility of Powder $TbFe_{1-x}Al_xO_3$ and $TbFe_{1-x}Ga_xO_3$ Solid Solutions". In: *Journal of Magnetism and Magnetic Materials* 250 (2002), p. 325. DOI: 10.1016/S0304-8853(02)00421-3.

[77] S. A. Guretskii et al. "Low-Temperature Magnetic Properties of Terbium Orthoferrite Single Crystals". In: *Crystal Research and Technology* 31 (1996), p. 897. DOI: 10.1002/crat.2170310716.

[78] Y.-Q. Song et al. "Multiferroic Properties in Terbium Orthoferrite". In: *Chinese Physics B* 23 (2014), p. 077505. DOI: 10.1088/1674-1056/23/7/077505.

[79] O. Nikolov et al. "Field-Induced Spin Reorientations in $TbFeO_3$ at 4.2 K". In: *Journal of Magnetism and Magnetic Materials* 152 (1996), p. 75.

[80] V. Y. Ivanov et al. "Observation of Magnetic-Field-Induced Electric Polarization in Terbium Orthoferrite". In: *JETP Letters* 117 (2023), p. 38. DOI: 10.1134/S0021364022602809.

[81] V. Y. Ivanov et al. "Metamagnetic and Orientational Transitions in $TbFeO_3$ Orthoferrite: Magnetoelectric Phase Diagrams". In: *The European Physical Journal Plus* 138 (2023), p. 818. DOI: 10.1140/epjp/s13360-023-04422-2.

[82] J. Tejada et al. "Quantum Tunnelling of Antiferromagnetic Domain Walls in $TbFeO_3$ Single Crystal". In: *Europhysics Letters* 30 (1995), p. 227.

[83] E. B. Krotenko, X. X. Zhang, and J. Tejada. "Self-Heating in Magnetic Relaxation Experiments in $TbFeO_3$ Single Crystal and Fe_3Tb Metallic Alloy". In: *Journal of Magnetism and Magnetic Materials* 150 (1995), p. 119. DOI: 10.1016/0304-8853(95)00462-9.

[84] M. C. Weber et al. "Raman Spectroscopy of Rare-Earth Orthoferrites $R\mathrm{FeO}_3$ (R=La, Sm, Eu, Gd, Tb, Dy)". In: *Physical Review B* 94 (2016), p. 214103. DOI: 10.1103/PhysRevB.94.214103.

[85] H. S. Nair et al. "Magnetic Structures and Magnetic Phase Transitions in the Mn-doped Orthoferrite $TbFeO_3$ Studied by Neutron Powder Diffraction". In: *Journal of Applied Physics* 119 (2016), p. 053901. DOI: 10.1063/1.4940958.

[86] Y. Fang et al. "Application of the Spin Reorientation in $RFe_{1-x}Mn_xO_3$ (R = Tb/Ho)". In: *Solid State Communications* 261 (2017), p. 37. DOI: 10.1016/j.ssc.2017.05.025.

[87] M. Mihalik et al. "Magnetic Phase Diagram of the $TbMn_{1-x}Fe_xO_3$ Solid Solution System". In: *Physica B: Condensed Matter* 506 (2017), p. 163. DOI: 10.1016/j.physb.2016.11.015.

[88] J. P. Bolletta et al. "Spin Reorientation and Metamagnetic Transitions in $RFe_{0.5}Cr_{0.5}O_3$ Perovskites (R = Tb, Dy, Ho, Er)". In: *Physical Review B* 98 (2018), p. 134417. DOI: 10.1103/PhysRevB.98.134417.

[89] J. Xu, Y. Cui, and H. Xu. "The Effect of Fe Content on Dielectric and Relaxation Characteristics in $TbFe_xMn_{1-x}O_3$". In: *Physica B: Condensed Matter* 545 (2018), p. 402. DOI: 10.1016/j.physb.2018.07.006.

[90] B. Mali et al. "Reentrant Spin Reorientation Transition and Griffiths-like Phase in Antiferromagnetic $TbFe_{0.5}Cr_{0.5}O_3$". In: *arXiv:2001.03723 [cond-mat]* (2020). arXiv: 2001.03723 [cond-mat].

[91] Y. Nishihara. "Effect of Nearest Neighbor Ions on the Hyperfine Fields at ^{57}Fe Nuclei in $TbFe_{1-x}Cr_xO_3$". In: *Journal of the Physical Society of Japan* 38 (1975), p. 710. DOI: 10.1143/JPSJ.38.710.

[92] A. Bombik and B. Les. "Crystal Structure of Solid Solutions $REFe_{1-x}(Al \text{ or } Ga)_xO_3$ (RE=Tb, Er, Tm) and the Correlation between Superexchange Interaction $Fe^{+3}O{-}^{-2}$-Fe^{+3} Linkage Angles and Neel Temperature". In: *Journal of Magnetism and Magnetic Materials* (2003), p. 14.

[93] B. Y. Kum, S. Y. An, and C. S. Kim. "Synthesis and Mössbauer Effects of $TbFe_{1-x}Mn_xO_3$ Nanoparticles". In: *IEEE Transactions on Magnetics* 41 (2005), p. 3481. DOI: 10.1109/TMAG.2005.854916.

[94] W. Kim, B. Y. Kum, and C. S. Kim. "Spin-Reorientation and Mössbauer Study of Orthoferrite $TbFe_{0.75}Mn_{0.25}O_3$". In: *Journal of Superconductivity and Novel Magnetism* 24 (2011), p. 867. DOI: 10.1007/s10948-010-1033-0.

[95] J.-L. Jin et al. "Influence of the Jahn-Teller Distortion on Magnetic Ordering in $\backslash\backslash TbMn_{1-x}Fe_xO_3$". In: *Chinese Physics B* 21 (2012), p. 107501. DOI: 10.1088/1674-1056/21/10/107501.

[96] H. Nhalil et al. "Spin-Reorientation and Weak Ferromagnetism in Antiferromagnetic $TbMn_{0.5}Fe_{0.5}O_3$". In: *Journal of Applied Physics* 117 (2015), p. 173904. DOI: 10.1063/1.4919660.

[97] Y. Fang et al. "Observation of Re-Entrant Spin Reorientation in $TbFe_{1-x}Mn_xO_3$". In: *Scientific Reports* 6 (2016). DOI: 10.1038/srep33448.

[98] A. Schneidewind and P. Čermák. "PANDA: Cold Three Axes Spectrometer". In: *Journal of large-scale research facilities JLSRF* 1 (2015), A12. DOI: 10.17815/jlsrf-1-35.

[99] A. Scheie. "LongHCPulse: Long-Pulse Heat Capacity on a Quantum Design PPMS". In: *Journal of Low Temperature Physics* 193 (2018), p. 60. DOI: 10.1007/s10909-018-2042-9.

[100] I.A. Tanaeva et al. "Heat Capacities and Magnetic Moments of Potential Regenerator Materials at Low Temperatures". In: *Cryogenics* 43 (2003), p. 441. DOI: 10.1016/S0011-2275(03)00099-7.

[101] K. Amelin et al. "Experimental Observation of Quantum Many-Body Excitations of E_8 Symmetry in the Ising Chain Ferromagnet $CoNb_2O_6$". In: *Physical Review B* 102 (2020), p. 104431. DOI: 10.1103/PhysRevB.102.104431. arXiv: 2006.12956.

[102] J. A. Kjäll, F. Pollmann, and J. E. Moore. "Bound States and E 8 Symmetry Effects in Perturbed Quantum Ising Chains". In: *Physical Review B* 83 (2011). DOI: 10.1103/PhysRevB.83.020407.

[103] J. Wu, M. Kormos, and Q. Si. "Finite-Temperature Spin Dynamics in a Perturbed Quantum Critical Ising Chain with an E 8 Symmetry". In: *Physical Review Letters* 113 (2014), p. 247201. DOI: 10.1103/PhysRevLett.113.247201.

[104] H. Zou et al. "E_8 Spectra of Quasi-one-dimensional Antiferromagnet $BaCo_2V_2O_8$ under Transverse Field". In: *Physical Review Letters* 127 (2021), p. 077201. DOI: 10.1103/PhysRevLett.127.077201. arXiv: 2005.13302.

[105] S. Lee, R. K. Kaul, and L. Balents. "Interplay of Quantum Criticality and Geometric Frustration in Columbite". In: *Nature Physics* 6 (2010), p. 702. DOI: 10.1038/nphys1696.

[106] S. Kobayashi et al. "Uniaxial-Pressure Control of Geometrical Spin Frustration in an Ising Antiferromagnet $CoNb_2O_6$ via Anisotropic Deformation of the Isosceles Lattice". In: *Physical Review B* 90 (2014). DOI: 10.1103/PhysRevB.90.060412.

[107] I. Cabrera et al. "Excitations in the Quantum Paramagnetic Phase of the Quasi-One-Dimensional Ising Magnet $CoNb_2O_6$ in a Transverse Field: Geometric Frustration and Quantum Renormalization Effects". In: *Physical Review B* 90 (2014). DOI: 10.1103/PhysRevB.90.014418.

[108] M. Vojta. "Quantum Phase Transitions". In: *Reports on Progress in Physics* 66 (2003), p. 2069. DOI: 10.1088/0034-4885/66/12/R01.

[109] S. Sachdev and B. Keimer. "Quantum Criticality". In: *Physics Today* 64 (2011), p. 29. DOI: 10.1063/1.3554314. arXiv: 1102.4628.

[110] P. Gegenwart, Q. Si, and F. Steglich. "Quantum Criticality in Heavy-Fermion Metals". In: *Nature Physics* 4 (2008), p. 186. DOI: 10.1038/nphys892.

[111] H. Nishimori and G. Ortiz. *Elements of Phase Transitions and Critical Phenomena*. Oxford University Press, 2011.

[112] N. D. Mermin and H. Wagner. "Absence of Ferromagnetism or Antiferromagnetism in One- or Two-Dimensional Isotropic Heisenberg Models". In: *Physical Review Letters* 17 (1966), p. 1133. DOI: 10.1103/PhysRevLett.17.1133.

[113] J. Custers et al. "The Break-up of Heavy Electrons at a Quantum Critical Point". In: *Nature* 424 (2003), p. 524. DOI: 10.1038/nature01774.

[114] N. D. Mathur et al. "Magnetically Mediated Superconductivity in Heavy Fermion Compounds". In: *Nature* 394 (1998), p. 39. DOI: 10.1038/27838.

[115] C. Heid et al. "Magnetic Phase Diagram of $CoNb_2O_6$: A Neutron Diffraction Study". In: *Journal of magnetism and magnetic materials* 151 (1995), p. 123.

[116] H. Weitzel et al. "Lifshitz Point in the Three-Dimensional Magnetic Phase Diagram of $CoNb_2O_6$". In: *Physical Review B* 62 (2000), p. 12146. DOI: 10.1103/PhysRevB.62.12146.

[117] C. Heid et al. "Magnetic Phase Diagrams of $CoNb_2O_6$". In: *Physica B: Condensed Matter* 234 (1997), p. 574.

[118] S. Kobayashi et al. "Three-Dimensional Magnetic Ordering in the Quasi-One-Dimensional Ising Magnet $CoNb_2O_6$ with Partially Released Geometrical Frustration". In: *Physical Review B* 60 (1999), p. 3331. DOI: 10.1103/PhysRevB.60.3331.

[119] S. B. Rutkevich. "On the Weak Confinement of Kinks in the One-Dimensional Quantum Ferromagnet $CoNb_2O_6$". In: *Journal of Statistical Mechanics: Theory and Experiment* 2010 (2010), P07015. DOI: 10.1088/1742-5468/2010/07/P07015.

[120] A. W. Kinross et al. "Evolution of Quantum Fluctuations Near the Quantum Critical Point of the Transverse Field Ising Chain System $CoNb_2O_6$". In: *Physical Review X* 4 (2014). DOI: 10.1103/PhysRevX.4.031008. arXiv: 1401.6917.

[121] C. M. Morris et al. "Hierarchy of Bound States in the One-Dimensional Ferromagnetic Ising Chain $CoNb_2O_6$ Investigated by High-Resolution Time-Domain Terahertz Spectroscopy". In: *Physical Review Letters* 112 (2014). DOI: 10.1103/PhysRevLett.112.137403.

[122] Y. F. Dai et al. *Unveiling the Quantum Critical Point of an Ising Chain*. 2011. DOI: 10.48550/arXiv.1103.0095. arXiv: 1103.0095 [cond-mat].

[123] H. Weitzel and S. Klein. "Magnetische struktur von columbiten $MnNb_2O_6$ und $CoNb_2O_6$". In: *Solid State Communications* 12 (1973), p. 113. DOI: 10.1016/0038-1098(73)90517-6.

[124] I. Maartense, I. Yaeger, and B. M. Wanklyn. "Field-Induced Magnetic Transitions of $CoNb_2O_6$ in the Ordered State". In: *Solid State Communications* 21 (1977), p. 93.

[125] T. Hanawa et al. "Anisotropic Specific Heat of $CoNb_2O_6$ in Magnetic Fields". In: *Journal of the Physical Society of Japan* 63 (1994), p. 2706. DOI: 10.1143/jpsj.63.2706.

[126] S. Kobayashi et al. "Domain Growth Kinetics in the Isosceles Triangular Ising Antiferromagnet $CoNb_2O_6$". In: *Physical Review B* 69 (2004), p. 144430. DOI: 10.1103/PhysRevB.69.144430.

[127] S. Thota et al. "Magnetic Ground State and Exchange Interactions in the Ising Chain Ferromagnet $CoNb_2O_6$". In: *Physical Review B* 103 (2021), p. 064415. DOI: 10.1103/PhysRevB.103.064415.

[128] S. Mitsuda et al. "Magnetic Ordering in One-Dimensional System $CoNb_2O_6$ with Competing Interchain Interactions". In: *Journal of the Physical Society of Japan* 63 (1994), p. 3568. DOI: 10.1143/JPSJ.63.3568.

[129] S. Mitsuda et al. "Disappearance of 2D Magnetic Character in Quasi-1D System $CoNb_2O_6$ under Magnetic Field". In: *Journal of the Physical Society of Japan* 64 (1995), p. 2325. DOI: 10.1143/jpsj.64.2325.

[130] E. M. D. Wheeler. "Neutron Scattering from Low-Dimensional Quantum Magnets". PhD thesis. University of Oxford, 2007.

[131] M. Nandi, D. Prabhakaran, and P. Mandal. "Spin-Charge-Lattice Coupling in Quasi-One-Dimensional Ising Spin Chain $CoNb_2O_6$". In: *Journal of Physics: Condensed Matter* 31 (2019), p. 195802. DOI: 10.1088/1361-648X/ab0539.

[132] S. Kobayashi, S. Mitsuda, and K. Prokes. "Low-Temperature Magnetic Phase Transitions of the Geometrically Frustrated Isosceles Triangular Ising Antiferromagnet $CoNb_2O_6$". In: *Physical Review B* 63 (2000), p. 024415. DOI: 10.1103/PhysRevB.63.024415.

[133] K. Matsuura et al. "Anomalous Lattice Softening Near a Quantum Critical Point in a Transverse Ising Magnet". In: *Physical Review Letters* 124 (2020), p. 127205. DOI: 10.1103/PhysRevLett.124.127205.

[134] S. Kobayashi et al. "Anisotropic Growth Kinetics in the Geometrically Frustrated Isosceles Triangular Ising Antiferromagnet $CoNb_2O_6$". In: *Physical Review B* 60 (1999), R9908. DOI: 10.1103/PhysRevB.60.R9908.

[135] N. J. Robinson et al. "Quasiparticle Breakdown in the Quasi-One-Dimensional Ising Ferromagnet $CoNb_2O_6$". In: *Physical Review B* 90 (2014). DOI: 10.1103/PhysRevB.90.174406.

[136] P. Laurell, G. Alvarez, and E. Dagotto. "Spin Dynamics of the Generalized Quantum Spin Compass Chain". In: *Physical Review B* 107 (2023), p. 104414. DOI: 10.1103/PhysRevB.107.104414.

[137] Y. Xu et al. "Quantum Critical Magnetic Excitations in Spin-1/2 and Spin-1 Chain Systems". In: *Physical Review X* 12 (2022), p. 021020. DOI: 10.1103/PhysRevX.12.021020.

[138] D. Churchill and H.-Y. Kee. *Transforming from Kitaev to Disguised Ising Chain: Application to $CoNb_2O_6$*. 2024. DOI: 10.48550/arXiv.2403.14754. arXiv: 2403.14754 [cond-mat].

[139] C. A. Gallegos and A. L. Chernyshev. "Magnon Interactions in the Quantum Paramagnetic Phase of $CoNb_2O_6$". In: *Physical Review B* 109 (2024), p. 014424. DOI: 10.1103/PhysRevB.109.014424.

[140] N. Xi et al. *Emergent $D_8^{(1)}$ Spectrum and Topological Soliton Excitation in $CoNb_2O_6$*. 2024. arXiv: 2403.10785 [cond-mat, physics:math-ph].

[141] P. Pfeuty. "The One-Dimensional Ising Model with a Transverse Field". In: *Annals of Physics* 57 (1970), p. 79. DOI: 10.1016/0003-4916(70)90270-8.

[142] R. Jullien et al. "Zero-Temperature Renormalization Method for Quantum Systems. I. Ising Model in a Transverse Field in One Dimension". In: *Physical Review B* 18 (1978), p. 3568. DOI: 10.1103/PhysRevB.18.3568.

[143] T. Nakajima et al. "Nonmagnetic Impurity Effect on Magnetic Phase Transitions in an Isosceles Triangular Lattice Ising Chain Antiferromagnet $CoNb_2O_6$". In: *Journal of the Physical Society of Japan* 83 (2014), p. 094723. DOI: 10.7566/JPSJ.83.094723.

[144] D. Bitko, T. F. Rosenbaum, and G. Aeppli. "Quantum Critical Behavior for a Model Magnet". In: *Physical Review Letters* 77 (1996), p. 940. DOI: 10.1103/PhysRevLett.77.940.

[145] Y. Liu and C. Petrovic. "Critical Behavior of Quasi-Two-Dimensional Semiconducting Ferromagnet $Cr_2Ge_2Te_6$". In: *Physical Review B* 96 (2017), p. 054406. DOI: 10.1103/PhysRevB.96.054406.

[146] W. Liu et al. "Critical Behavior of the Single-Crystalline van Der Waals Bonded Ferromagnet $Cr_2Ge_2Te_6$". In: *Physical Review B* 98 (2018), p. 214420. DOI: 10.1103/PhysRevB.98.214420.

[147] Z. Wang et al. "Quantum Criticality of an Ising-like Spin-1/2 Antiferromagnetic Chain in a Transverse Magnetic Field". In: *Physical Review Letters* 120 (2018), p. 207205. DOI: 10.1103/PhysRevLett.120.207205.

[148] Y. Cui et al. "Quantum Criticality of the Ising-like Screw Chain Antiferromagnet $SrCo_2V_2O_8$ in a Transverse Magnetic Field". In: *Physical Review Letters* 123 (2019), p. 067203. DOI: 10.1103/PhysRevLett.123.067203.

[149] X. Zhang et al. “Quantum Phase Transitions in a Quasi-One-Dimensional Ising Quantum Magnet in Transverse Fields”. In: *Physical Review B* 103 (2021), p. 144405. DOI: 10.1103/PhysRevB.103.144405.

[150] Isha et al. “Sharp Quantum Phase Transition in the Frustrated Spin-1/2 Ising Chain Antiferromagnet $CaCoV_2O_7$”. In: *Physical Review Research* 6 (2024), p. L032010. DOI: 10.1103/PhysRevResearch.6.L032010.

Acknowledgements

Während meiner Zeit am Lehrstuhl habe ich durch viele Leute tatkräftige Unterstützung erfahren, wofür ich mich explizit bedanken will.

- **Christian Pfleiderer** Vielen Dank, dass ich im Rahmen der Masterarbeit und der Promotion ein Teil deiner Gruppe werden durfte und du mir während dieser Zeit immer mit Rat und Tat zur Seite standest.
- **Andreas Bauer und Gorg Benka** für die Einführung in den Lehrstuhl. Ihr wart ein zentraler Bestandteil der tollen Atmosphäre in der Arbeitsgruppe und habt mich dadurch zur Promotion motiviert.
- **Meinen aktuellen und ehemaligen Bürokollegen Nico, Oleu, Anh, Caro, Andi Wendl und Grace** Es war eine wirklich schön und lustig mit euch das Büro zu teilen und sich über alle möglichen Dinge auszutauschen.
- **Cresch, Wukas, Andre, Leo, Flo, Michelle, Markus, Michi, Stefan, Marc, Fabian, Johanna** Vielen Dank für die gute Gesellschaft bei Diskussionen in der Kaffeerunde, auf Konferenzen und auch nach der Arbeit.
- **Das Kristalllabor, insbesondere Andreas, Susi, Astrid und Sandra** Vielen Dank für die präzise Präparation der Proben und die Unterstützung bei der Probensynthese und beim Ausrichten der Kugelproben am Lauediffraktometer.
- **Meine Vorgänger am Lehrstuhl Steffen, Felix, Marco, Wolle, Fonsi, Jan, Aggl, Christopher, Marc, Schorsch** für den Transfer ihres Wissens und sonstiger Lebensweisheiten.
- **Meine Eltern** Vielen Dank für die bedingungslose Unterstützung während meiner gesamten akademischen Laufbahn.
- **Meine Freunde in Rosenheim** Es ist immer wieder eine schöne Abwechslung, euch bei meinen Heimatbesuchen zu sehen und die alten Zeiten wieder aufleben zu lassen.
- **Melanie** Danke, dass du Teil meines Lebens geworden bist und du vor allem in schwierigen Zeiten immer für mich da warst.